SANDIA REPORT

SAND2012-1354
Unlimited Release
February, 2012

Photoelectronic Characterization of Heterointerfaces

Michael T. Brumbach

Prepared by
Sandia National Laboratories
Albuquerque, New Mexico 87185 and Livermore, California 94550

Sandia National Laboratories is a multi-program laboratory managed and operated by Sandia Corporation, a wholly owned subsidiary of Lockheed Martin Corporation, for the U.S. Department of Energy's National Nuclear Security Administration under contract DE-AC04-94AL85000.

Approved for public release; further dissemination unlimited.

Sandia National Laboratories

Issued by Sandia National Laboratories, operated for the United States Department of Energy by Sandia Corporation.

NOTICE: This report was prepared as an account of work sponsored by an agency of the United States Government. Neither the United States Government, nor any agency thereof, nor any of their employees, nor any of their contractors, subcontractors, or their employees, make any warranty, express or implied, or assume any legal liability or responsibility for the accuracy, completeness, or usefulness of any information, apparatus, product, or process disclosed, or represent that its use would not infringe privately owned rights. Reference herein to any specific commercial product, process, or service by trade name, trademark, manufacturer, or otherwise, does not necessarily constitute or imply its endorsement, recommendation, or favoring by the United States Government, any agency thereof, or any of their contractors or subcontractors. The views and opinions expressed herein do not necessarily state or reflect those of the United States Government, any agency thereof, or any of their contractors.

Printed in the United States of America. This report has been reproduced directly from the best available copy.

Available to DOE and DOE contractors from
U.S. Department of Energy
Office of Scientific and Technical Information
P.O. Box 62
Oak Ridge, TN 37831

Telephone: (865) 576-8401
Facsimile: (865) 576-5728
E-Mail: reports@adonis.osti.gov
Online ordering: http://www.osti.gov/bridge

Available to the public from
U.S. Department of Commerce
National Technical Information Service
5285 Port Royal Rd.
Springfield, VA 22161

Telephone: (800) 553-6847
Facsimile: (703) 605-6900
E-Mail: orders@ntis.fedworld.gov
Online order: http://www.ntis.gov/help/ordermethods.asp?loc=7-4-0#online

SAND2012-1354
Unlimited Release
February, 2012

Photoelectronic Characterization of Heterointerfaces

Michael Todd Brumbach
Materials Characterization
Sandia National Laboratories
P.O. Box 5800
Albuquerque, New Mexico 87185-MS0886

Abstract

In many devices such as solar cells, light emitting diodes, transistors, etc., the performance relies on the electronic structure at interfaces between materials within the device. The objective of this work was to perform robust characterization of hybrid (organic/inorganic) interfaces by tailoring the interfacial region for photoelectron spectroscopy. Self-assembled monolayers (SAM) were utilized to induce dipoles of various magnitudes at the interface. Additionally, SAMs of molecules with varying dipolar characteristics were mixed into spatially organized structures to systematically vary the apparent work function. Polymer thin films were characterized by depositing films of varying thicknesses on numerous substrates with and without interfacial modifications. Hard X-ray photoelectron spectroscopy (HAXPES) was performed to evaluate a buried interface between indium tin oxide (ITO), treated under various conditions, and poly(3-hexylthiophene) (P3HT). Conducting polymer films were found to be sufficiently conducting such that no significant charge redistribution in the polymer films was observed. Consequently, a further departure from uniform substrates was taken whereby electrically disconnected regions of the substrate presented ideally insulating interfacial contacts. In order to accomplish this novel strategy, interdigitated electrodes were used as the substrate. Conducting fingers of one half of the electrodes were electrically grounded while the other set of electrodes were electronically floating. This allowed for the evaluation of substrate charging on photoelectron spectra (SCOPES) in the presence of overlying semiconducting thin films. Such an experiment has never before been reported. This concept was developed out of the previous experiments on interfacial modification and thin film depositions and presents new opportunities for understanding chemical and electronic changes in a multitude of materials and interfaces.

ACKNOWLEDGMENTS

Many people helped with various aspects of this project. I would like to thank Jim Aubert, William Wallace, Joe Michael, Bruce Bunker, Jim Voigt, Kevin Zavadil, Ana Trujillo, Tony Ohlhausen, and Michael Kalan for general support. Dave Wheeler, Mark Roberts, Ronen Polsky, and Xiaoyin Xiao assisted with various aspects of polymer depositions and diazonium modifications. I would like to thank Cody Washburn for providing interdigitated electrodes and a photoresist master for patterning. I would also like to thank Seong Kim and Brandon Veres for their assistance with patterned P3HT films. I would also like to thank Cherno Jaye, and Daniel Fischer for assistance with NEXAFS and NEXAFS imaging as well as Joe Woicik, Barry Karlin, and Conan Weiland for help with HAXPES measurements.

CONTENTS

Nomenclature 13

1. INTRODUCTION 15

2. METHODS 17
   2.1. Sample Preparation 17
   2.2. Analysis Methods 20

3. SURFACE MODIFICATIONS 21
   3.1. Uniform Surface Treatments 21
   3.2. Patterned Surface Modifications 23
      3.2.1. Shadow Mask Patterned Thiols on Gold 24
      3.2.2. Silhouette Patterning Using Nylon Shadow Masks 36
      3.2.3. Other Patterning Strategies 40

4. CONDUCTING POLYMER INTERFACES 43
   4.1. Varying Thickness Conducting Polymer Films 43
   4.2. PEDOT on COOH-Modified ITO and Unmodified-ITO 47
   4.3. HAXPES of Protected ITO Interfaces with P3HT 49
   4.3. Photoelectronic Characterization of Discontinuous P3HT Films on ITO 57

5. INTERDIGITATED ELECTRODES 65
   5.1. PEDOT on Gold IDE 65
   5.2. TiOPc and C_{60} on Gold IDEs 68
   5.3. Pentacene Conversion on IDE 70

6. CONCLUSIONS 75

7. REFERENCES 77

Distribution 81

FIGURES

Figure 1. Modification of ITO was performed with 16-phosphonohexadecanoic acid (COOH) to functionalize the surface with terminal carboxylic acid groups. ITO was also modified with 4-nitrobenzenediazonium, loosely termed “diazonium”, by electrochemical grafting. The nitro group was used for subsequent conversion to the NH_2 amine and could also be protonated to NH_3^+. Perfluorodecanethiol (C10F8) and decanethiol (C10) were used for SAM modification of gold and ZnO. 18

Figure 2. Polymers used in this study were PEDOT, PANI, poly(thiophene), P3HT, and N3. PEDOT:PSS, when deposited via spin coating, most commonly contains the poly(styrene sulfonate) counterion. In this study, PANI, poly(thiophene), and N3 were deposited electrochemically, while P3HT and PEDOT were deposited via spin coating. 19

Figure 3. Modification of ITO was performed with 16-phosphonohexadecanoic acid (COOH) to functionalize the surface with carboxylic acid terminal groups. The XPS spectra (left) show an increase in carbon associated with the presence of the SAM on the ITO surface. The UPS spectra (right), show little change in the low kinetic energy edge although there is an increase in

emission for the COOH-modified electrode. The lack of a shift in work function suggests heterogeneous orientation of the COOH terminal group in the modifying SAM layer..... 21
Figure 4. XPS spectra are shown for diazonium modified ITO substrates in (A) survey spectra, (B) O 1s spectra, and (C) C 1s spectra. NO_2 refers to the as deposited nitrobenzene diazonium SAM. NH_2 is the converted amine, while NH_3^+ is the protonated amine. The nitro-diazonium shows an O 1s shoulder form the NO_2 group, which is removed after conversion to the amine. 22
Figure 5. UPS spectra for the diazonium modified ITO show that the work function varies according to the expected dipole for the surface modifying SAM. NO_2 refers to the as deposited nitrobenzene diazonium SAM. NH_2 is the converted amine while, NH_3^+ is the protonated amine terminal functional group. The work function increases according to the shift in the low KE edge of the spectra, $NH_3^+ < NH_2 < NO_2$. 23
Figure 6. Thiol modification of gold was accomplished by first treating the sample with decanethiol (C10). The sample was then subjected to UV/ozone cleaning with and without shadow masks to remove all thiol from unmasked regions. The patterned C10 was then placed in perfluorodecanethiol (C10F8) to backfill the unmodified regions. This strategy gave patterned C10 SAM layers of varying surface area percentages, as well as patterned C10/C10F8 patterned films with varying surface coverages. 24
Figure 7. Thiol modification of gold was accomplished by first treating the sample with perfluorodecanethiol (C10F8). The sample was then subjected to UV/ozone cleaning with and without shadow masks to remove all thiol from unmasked regions. The patterned C10F8 was then placed in decanethiol (C10) to backfill the unmodified regions. This strategy gave patterned C10F8 SAM layers of varying surface area percentages, as well as patterned C10F8/C10 patterned films with varying surface coverages..... 25
Figure 8. UPS spectra are shown for cleaned and modified gold control samples. (A) Spectra are shown for two gold samples which have been UV/ozone cleaned and one sample which was sputtered. Spectra are also shown for samples modified with either C10 of C10F8 SAM with subsequent UV/ozone cleaning to remove the SAM. (B) Spectra are shown for a C10 modified gold surface as well as three spectra for C10 modification after a C10F8 SAM was removed via UV/ozone cleaning. (C) A UPS spectrum is shown for a C10F8 modified gold surface as well as two spectra for C10F8 SAMs deposited after a C10 SAM was removed. 26
Figure 9. C 1s spectra are shown for control samples where C10 was deposited initially (C10), and where C10 was deposited after a C10F8 SAM was removed (C10(post-C10F8)). C10F8 was also deposited initially (C10F8), as well as deposited after a C10 SAM was removed (C10F8(post-C10)). The C 1s is more intense and narrower for C10 films modified after C10F8 relative to the as-deposited C10 film. The components at high BE, corresponding to C-F, are more pronounced for the C10F8 deposited after the C10 SAM was removed. These results show that a more compact SAM was obtained after an initial SAM was deposited and removed. 27
Figure 10. UPS spectra from (A) decanethiol (C10) and (B) perfluorodecanethiol (C10F8) modified gold. The percentages show the area of surface modification by the respective SAM. The remaining area was UV/ozone cleaned in the etching process. 28
Figure 11. (Upper left) Work function is shown for the C10 and C10F8 SAM films as a function of the area of surface modification. (Upper right) The percent composition of fluorine is shown for the C10F8 sample as a function of the modified surface area. C10 did not show any evidence of fluorine. (Lower left) The percent composition of gold is shown versus the area of modification for the two SAM films. A linear relationship would be expected. (Lower right) The percent composition of carbon is shown versus the area of modification. 29

Figure 12. (A) The C 1s spectra for C10 modified gold are shown for the various areas of modification as indicated. (B) The C 1s spectra for C10F8 modified gold are shown for the various areas of modification. The C-F component at high binding energy is only observed for the 100% modified sample..... 30
Figure 13. UPS spectra are shown for patterned bimolecular SAMs. The percentages show the expected area of C10 modification where the remaining area was modified by C10F8. Cases where C10 was patterned in the lines of the mask pattern are from initial C10 deposition followed by UV/ozone cleaning through the mask and C10F8 deposition. C10F8 in the lines was performed first followed by C10 backfilling. 30
Figure 14. Patterned bimolecular SAMs (PB_SAMs) show distinct differences in work function and percent composition. Values are shown for C10 coverage either in the holes or lines of the mask pattern, with C10F8 filling the remainder of the surface area. (Upper left) The work function is shown as a function of the area of surface modification expected from the geometry of the shadow mask. (Upper right) The percent composition of fluorine is shown for the case where C10F8 was backfilled into the holes of the C10 line pattern. When C10 was backfilled into the C10F8 line pattern, there was no evidence of fluorine. (Lower left) The percent composition of gold is shown versus the area of C10 modification. Since the full surface of the gold substrate should be coated with a SAM, the concentration of gold should not change significantly. (Lower right) The percent composition of carbon is shown versus the area of C10 modification. 31
Figure 15. (A) The C 1s spectra are shown for the various areas of C10 modification where C10 was patterned first and backfilled by C10F8. The C-F components at high BE are clearly observable when C10F8 was deposited into the holes of the C10 pattern. (B) The C 1s spectra are shown for the various areas of C10 modification where C10F8 was patterned first followed by backfilling with C10. No indication of C-F bonds from C10F8 are observed. 32
Figure 16. A NEXAFS image is shown for a sample where C10 was initially patterned in the lines of the grid shadow mask and C10F8 was backfilled into the open areas. Black areas are from gold delamination from the quartz substrate. A -100V bias was applied to the grid at the entrance to the partial electron yield detector. 33
Figure 17. A NEXAFS image is shown for a sample where C10 was initially patterned in the lines of the grid shadow mask and C10F8 was backfilled into the open areas. Black areas are from gold delamination from the quartz substrate. A -150V bias was applied to the grid at the entrance to the partial electron yield detector, making the measurement slightly more surface sensitive than the previous Figure..... 34
Figure 18. A NEXAFS image is shown for a sample where C10F8 was initially patterned in the lines of the grid shadow mask and the open areas were left unmodified. A -150V bias was applied to the grid at the entrance to the partial electron yield detector. The lower right figure is a blow up of the upper right figure. 35
Figure 19. A NEXAFS spectrum is shown for a sample where C10F8 was initially patterned by UV/ozone followed by backfilling with C10. A -150V bias was applied to the grid at the entrance to the partial electron yield detector. No contrast was observed in the corresponding NEXAFS image to indicate a patterned SAM. 36
Figure 20. XPS spectra are shown for silhouette patterned ZnO samples. A,B, and C show the C 1s spectra for the indicated specimens. E, F, and G show the O 1s spectra. The (*) indicates carbon environments such as C-S, C-N, or C-O. The (**) is a C-F component. For O 1s, the

primary component at lower BE is the oxide component, while the peak at higher BE (†) is from additionally oxidized species. 38
Figure 21. XPS spectra are shown for silhouette patterned ZnO samples. A,B, and C show the S 2p spectra for the indicated specimens. E, F, and G show the N 1s spectra. 39
Figure 22. F 1s spectra are shown for C10F8 silhouette patterned ZnO samples..... 39
Figure 23. UPS spectra for the various silhouette patterned ZnO samples. (A) ZnO samples where no thiol modification was performed, but the three different sized nylon patterns were used during UV/ozone cleaning. (B) C10-modified ZnO. (C) C10F8-modified ZnO. 40
Figure 24. An optical image of the photoresist master with an array of 16 patterns is shown along with the description of each domain. PDMS can be used to form a reverse replica of the master for microcontact printing. 41
Figure 25. An interdigitated electrode (IDE) is shown as a substrate for use in photoemission analyses. The region under analysis is large enough to cover electrodes from both pairs of electrodes as well as the interdigit spacing. The interdigit spacing is equal to the width of the electrodes. Gold is deposited as the electrode fingers on a quartz substrate. The voltage on the electrodes can be controlled. In the simplest case, one set of electrodes is grounded to the spectrometer while the other set of electrodes is left electrically floating. As shown on the right, Au 4f emission at ~84 eV (BE) is due to emission from the grounded gold electrodes, while the highly shifted Au 4f emission is due to charging of the electrically floating gold electrodes. The shift of the floating electrodes gives an indication of the nature of the surface and/or the electronic communication with the grounded electrodes. 42
Figure 26. The most common method for analyses of the energy level alignment at an interface is through sequential deposition of the topmost material with corresponding photoemission characterization at each stage. This gives characterization to various depths across the interface. For evaluation of polymer films on an inorganic substrate, the polymers must be deposited *ex situ* on multiple samples to give a range of thicknesses. 43
Figure 27. XPS spectra are shown for electrochemically deposited (A) poly(thiophene) and (B) poly(aniline) on gold at three different thicknesses from (1) thinnest to (3) thickest..... 43
Figure 28. N3 polymer was electrochemically deposited on ITO. The increase in thickness is observed from sample 1-7 as the In and Sn signals become attenuated due to the overlying polymer. The components of the N3 polymer, namely C, N and S grow in intensity as the N3 polymer thickness increases. Impurities were observed in the N3 polymer. 45
Figure 29. N3 polymer was electrochemically deposited on ITO. The increase in thickness is observed from sample 1-7 as the In and Sn signal became attenuated due to the overlying polymer. The O 1s from ITO is attenuated until a thick film of N3 was deposited and a broad O 1s peak was observed due to entrained contaminants and charging. 45
Figure 30. N3 polymer was electrochemically deposited on ITO. The increase in thickness is observed from sample 1-7 as the C, N, and S peaks grow in intensity. The thickest film shows a broadening of the C, N, and S peaks due to some differential charging of the polymer. 46
Figure 31. UPS spectra are shown for the N3 polymer electrochemically deposited on ITO at three thicknesses. Sample (7) corresponds to the thickest N3 film. 46
Figure 32. Survey XPS spectra are shown for PEDOT layers of varying thicknesses spin coated on (A) unmodified ITO and (B) 16-phosphonohexadecanoic (COOH) modified ITO. No PEDOT was present on (1) and thicknesses of PEDOT were increased from 2-5. 47

Figure 33. XPS spectra of C 1s are shown for PEDOT layers of varying thicknesses spin coated on (A) unmodified ITO and (B) 16-phosphonohexadecanoic (COOH) modified ITO. No PEDOT was present on (1) and thicknesses of PEDOT were increased from 2-5. 48
Figure 34. UPS spectra for PEDOT layers of varying thicknesses spin coated on (A) unmodified ITO and (B) 16-phosphonohexadecanoic (COOH) modified ITO. No PEDOT was present on (1) and thicknesses of PEDOT were increased from 2-5. 48
Figure 35. Work function does not change significantly for the various thicknesses of PEDOT on the two ITO substrates. Work function is shown as a function of indium concentration, where decreasing In concentration related to increasing PEDOT thickness. Work function is also shown relative to sulfur concentration, where increasing sulfur relates to increasing PEDOT thickness..... 49
Figure 36. Survey spectra are shown for P3HT films on ITO surfaces using three different X-ray energies as indicated. Prior to P3HT deposition, ITO surfaces were treated with (A) solvent cleaning only, (B) solvent cleaning followed by UV/ozone treatment, and (C) H_2SO_4 etching. . 51
Figure 37. O 1s spectra are shown for ITO buried under P3HT films using three different X-ray energies. Prior to P3HT deposition, ITO surfaces were treated with (A) solvent cleaning only, (B) solvent cleaning followed by UV/ozone treatment, and (C) H_2SO_4 etching. Peak A and B were fixed at identical binding energy separations, FWHM, and area ratios across all spectra. This allowed for the clear identification of an asymmetric component, peak C, associated with the conducting ITO substrate in the deeper HAXPES analyses. Peak C was also observed in the 2.2 keV analysis of the H_2SO_4 treated ITO/P3HT sample..... 53
Figure 38. In $3d^5/_2$ spectra are shown for ITO buried under P3HT films using three different X-ray energies. Prior to P3HT deposition, ITO surfaces were treated with (A) solvent cleaning only, (B) solvent cleaning followed by UV/ozone treatment, and (C) H_2SO_4 etching. Peak A and B were fixed at identical binding energy separations, FWHM, and area ratios across all spectra. An asymmetric component, peak C, associated with the conducting ITO substrate, was observed in all spectra but increased in intensity as the depth of analysis increased..... 54
Figure 39. (A) The analysis depth, based upon 3x(IMFP) values for the respective X-ray energies, is plotted versus the atomic concentration of indium observed in survey spectra. A linear relationship was observed extrapolating to a y-intercept of zero indium content, i.e. the thickness of the P3HT film. (B) The analysis depth is plotted versus the relative content of the bulk oxide constituent from the O 1s peak fits. A bulk oxide constituent of zero shows that the only contribution to the O 1s spectra is from the oxidized surface layer. Consequently, the y-intercept relates to the depth of the interface between the bulk oxide and the surface oxidized layer, plus the thickness of the P3HT film..... 56
Figure 40. The analysis depth of XPS can be tuned in HAXPES by changing the energy of the illuminating X-ray. For the P3HT films investigated in this work, the films were sufficiently thin to allow for examination of the P3HT/ITO interface using three different X-ray energies. HAXPES revealed a thicker surface oxidized layer in the ITO films cleaned solvent and UV/ozone treatments. 56
Figure 41. HAXPES allows for the use of different X-ray energies to probe various depths of the near surface region. Higher photon energy probes deeper into the sample. Consequently, an interface can be evaluated by simply changing the excitation energy to probe above, at, or below the interfacial region. 57
Figure 43. Optical images of cross-hatch patterns on P3HT films on ITO. Images are 480microns by 580microns. Samples II and VI were 20nm thick P3HT films, and samples IV

and VIII were 10nm films. Samples II and IV were spin coated under under dry N_2. Samples VI and VIII were spin coated under ambient atmospheric conditions. 58
Figure 44. (Top) XPS spectra are shown for the P3HT films in (left) unpatterned regions and (right) patterned regions. The In and Sn from the substrate are observed through the patterned scratches in the XPS of the patterned P3HT films. (Bottom) UPS spectra are shown for the (left) unpatterned and (right) patterned P3HT films. Samples II and VI were 20nm thick P3HT films, and samples IV and VIII were 10nm films. Samples II and IV were spin coated under under dry N_2. Samples VI and VIII were spin coated under ambient atmospheric conditions. The "_x" nomenclature indicates the region on the film where lines were cross-hatched into the P3HT film exposing ITO. 59
Figure 45. XPS images are shown for the two components showing the greatest contrast for the P3HT patterned film II (20nm thick P3HT spin coat under dry N_2). The P3HT layer, composed of C and S, is observed in between the lines where the ITO constituents are observed. The images are 400microns by 400 microns. Images correspond to the intensity of the spectra shown to the left of the image. 61
Figure 46. XPS images are shown for the two components showing the greatest contrast for the P3HT patterned film IV (10nm thick P3HT spin coat under dry N_2). The P3HT layer, composed of C and S, is observed in between the lines where the ITO constituents are observed. The images are 400microns by 400 microns. Images correspond to the intensity of the spectra shown to the left of the image. 61
Figure 47. XPS images are shown for the two components showing the greatest contrast for the P3HT patterned film VI (20nm thick P3HT spin coat under ambient conditions). The P3HT layer, composed of C and S, is observed in between the lines where the ITO constituents are observed. The images are 400microns by 400 microns. Images correspond to the intensity of the spectra shown to the left of the image. 62
Figure 48. XPS images are shown for the two components showing the greatest contrast for the P3HT patterned film VIII (10nm thick P3HT spin coat under ambient conditions). The P3HT layer, composed of C and S, is observed in between the lines where the ITO constituents are observed. The images are 400microns by 400 microns. Images correspond to the intensity of the spectra shown to the left of the image. 62
Figure 49. A NEXAFS image, and the corresponding spectrum, is shown for the P3HT patterned film II. Red coloration relates to the intensity of the given spectrum. The black lines indicate no data collected in those regions. A -100V bias was applied to the grid at the entrance to the partial electron yield detector..... 63
Figure 50. A NEXAFS image, and the corresponding spectra, is shown for the P3HT patterned film IV. White and blue coloration relates to the intensity of the indicated spectra. A -100V bias was applied to the grid at the entrance to the partial electron yield detector. 63
Figure 51. XPS spectra for unmodified gold IDEs with and without PEDOT overlayer using two different dimensions of interdigitated electrodes..... 66
Figure 52. XPS spectra for C10-modified gold IDEs with and without PEDOT overlayer using two different dimensions of interdigitated electrodes..... 66
Figure 53. XPS spectra for C10F8-modified gold IDEs with and without PEDOT overlayer using two different dimensions of interdigitated electrodes. 67
Figure 54. The schematic for the change in BE position of the Au 4f peaks is shown for the case of an IDE substrate used in XPS. In the case where there is no electronic communication between the grounded and floating pairs of IDE electrodes, there is a large shift in the BE of the

emission from the floating gold due to static charging. When PEDOT is cast over the interdigit spacing, the ungrounded IDE electrodes are effectively wired through the PEDOT to the grounded electrodes. Consequently, the charging effect is removed and only one set of Au 4f peaks is observed. 68
Figure 55. XPS spectra are shown for (left) sputter cleaned gold IDE, (middle) C_{60} on sputter cleaned gold IDE, and (right) TiOPc on sputter cleaned gold IDE. (*) indicate emission from the grounded gold IDE. (**) indicate emission from carbon in electrically grounded environments. (***) indicate N 1s emission from electrically grounded environments. (†) indicate emission from electrically charged gold IDEs. (‡) indicate emission from charged carbon environments. Significant charging of the floating electrodes is observed for the sputter cleaned gold, where there is no conductive pathway from the grounded electrodes to the floating electrodes. There is only a slight shift in the charged components corresponding to the difference in interdigit spacing. For C_{60}, in which electron mobility is significantly greater than hole mobility, the charged gold components are shifted much closer to the grounded Au 4f emission. Alternatively, for TiOPc, where hole mobility is highest, the shift of the charged Au 4f emission is less than was observed for C_{60}. 69
Figure 56. The shift of the charged gold and charged carbon components are not equivalent. The shift of the charged gold components relative to the grounded components, are shown as a function of interdigit spacing. The shift is much greater for the TiOPc films than for the C60 films. (The value at 50microns probably has additional charging due to an inadequate contact.) The difference between the shift of the charged gold components and the charged carbon components are shown on the right-hand y-axis. Gold components shift to a greater extent that the carbon components. 69
Figure 57. A cartoon of electron flow is shown for a simplified IDE electrode. Arrows relate to electron flow. Electrons are emitted from all illuminated areas of the sample leaving core holes which must be refilled. The only path for electrons back into the system is through the grounding of the sample to the electron spectrometer. Electrons must then inject into the organic film and then transport across the interdigit gap through the organic, and reinjected into the electrically disconnected gold IDE. Since there is an additional charge injection step to neutralize the floating gold IDEs, the charged gold components are always shifted more than the charged carbon components. Background emission form the quartz substrates is either not observed, due to an insufficient escape depth through the overlying organic film, or are so charged as to be broadened and shifted out of the spectrum. 70
Figure 58. The pentacene precursor was deposited via spin coating from solution. The sample was then placed under vacuum where it was analyzed via XPS. Conversion to the pentacene molecule was performed by heating the sample *in situ*. Analyses of the resulting films were then performed without breaking vacuum. The film of the pentacene precursor should not have any appreciable conductivity, while the pentacene film would be expected to be conducting. 71
Figure 59. XPS spectra of the pentacene precursor on cleaned gold interdigitated electrodes are shown for (red) a uniform film on gold, (green) 15µm IDE, (pink) 20 µm IDE, and (blue) 25 µm IDE. Spectra shown are (left) survey spectra, (middle) Au 4f and charged Au 4f components, (right) C 1s and charged C 1s components. 72
Figure 60. XPS spectra of the converted pentacene on cleaned gold interdigitated electrodes are shown for (red) a uniform film on gold, (green) 15µm IDE, (pink) 20 µm IDE, and (blue) 25 µm IDE. Spectra shown are (left) survey spectra, (middle) Au 4f and charged Au 4f components, (right) C 1s and charged C 1s components. 73

Figure 61. The shift in the charged gold and charged carbon components are shown relative to their respective grounded components, as a function of interdigitated electrode spacing. The shift in the charged gold components is greater than that of the charged carbon components, and the difference is shown on the right-hand y-axis. 73

TABLES

Table 1. Work function values for gold surfaces with and without SAM modifications. C10 and C10F8 were both deposited on initially clean surface as well as on surface which had been previously modified with the alternate thiol. 27
Table 2. Work function values for thiol modified ZnO films via silhouette patterning. The openings of the nylon square mesh are indicated, where UV/ozone treatment was performed to pattern through the silhouette mask. Solvent cleaned, C10, and C10F8 were not UV/ozone treated. 37
Table 3. Work function values and atomic concentrations for seven thicknesses of N3 polymer on ITO. Thicknesses of the polymer increase from 1-7 corresponding to the increase in C concentration. 47
Table 5. Fitting parameters for the In 3d 5/2 and O 1s components. In 3d 5/2 peak B was fixed at FWHM=1.3, BE position A+1.375, and area=A*1.95. O 1s peak B was fixed at FWHM=2.5, BE position A+1.945, and area=A*1.95. 55
Table 6. Work function values and atomic concentrations for the various P3HT films on ITO. 60

NOMENCLATURE

IPA	isopropanol
XPS	X-ray photoelectron spectroscopy
UPS	UV photoelectron spectroscopy
SNL	Sandia National Laboratories
RMS	root mean squared
MSDS	material safety data sheet
ITO	indium tin oxide
NSLS	National Synchrotron Light Source
BNL	Brookhaven National Laboratories
COOH	16- phosphonohexadecanoic acid
Diazonium	4-nitrobenzenediazonium tetrafluoroborate
C10	hexadecanethiol
C10F8	perfluorodecanethiol
HAXPES	hard energy X-ray photoelectron spectroscopy
NEXAFS	near edge X-ray absorption fine structure
IDE	interdigitated electrode
BE	binding energy
KE	kinetic energy
PDMS	poly(dimethyl siloxane)
SAM	self-assembled monolayer
QCM	quartz crystal microbalance
WF	work function
OPV	organic photovoltaic
OLED	organic light emitting diode
OFET	organic field effect transistor
P3HT	poly(3-hexyl thiophene)
PEDOT	poly(3,4-ethylenedioxythiophene)-poly(styrenesulfonate)
TiOPc	titanyl phthalocyanine

1. INTRODUCTION

The study of semiconducting organic materials has been progressing towards use of these materials as alternatives to traditional inorganic semiconductors in electronics. The anticipated benefits of organic electronics are based largely upon cost and processing advantages. Despite the implication of electronics based entirely on organic materials, the numerous examples of organic electronic devices, such as organic photovoltaics (OPV), organic light emitting diodes (OLED), and organic field effect transistors (OFET), the organic materials ultimately interface with inorganic materials at electrical contacts in most cases. Additionally, many organic devices actually contain inorganic materials as active components.[1-5] The interfaces between organic/organic materials have been increasingly examined yielding important mechanistic insights. For example, the output voltage has been shown to be determined by the offset potential at the organic/organic heterojunction in small molecule OPV devices.[6-9] Photoelectron spectroscopy can be used to map the band structure through careful analyses of layer-by-layer formation of an interface where ionization potential, core level positions, and work function are monitored.[6-11] However, characterization of interfaces between inorganic materials and active organic layers has been lagging. Many assumptions are prevalent including the fact that properties are often assumed from bulk measurements and the effects of ubiquitous contamination at surfaces and interfaces have been neglected.[12, 13] As organic devices have increased in efficiency, through new materials and innovative designs, it has become more relevant to examine the inorganic/organic interfaces to further push the technology and seek breakthroughs for increasing performance.

This study has characterized uniform and patterned surface treatments of inorganic substrates along with interfaces of modified and unmodified inorganic substrates with overlying organic thin films. Thin film deposition capabilities and materials analysis techniques have been developed. Additionally, the discovery of a new technique for materials characterization was explored.

2. METHODS

This study relied heavily on photoemission characterization using XPS and UPS. Samples were prepared to compliment the analysis depth of XPS/UPS where films were typically deposited at sub-micron thicknesses. In general the exact thicknesses of the deposited films were not of interest, because the attenuation of the substrate intensity, as observed via XPS, gave an accurate indication of film thickness and could be used for relative comparisons among a sequence of films. This section describes the general methods for sample preparation and analytical characterization. More detailed descriptions are given in the respective sections.

2.1. Sample Preparation

Electrode materials evaluated included gold, ZnO, and indium-tin-oxide (ITO). Sputter deposited gold on quartz was used as gold substrates. Indium tin oxide (ITO) was purchased from Colorado Concept Coatings LLC. ITO was cleaved into 1cm^2 coupons for subsequent cleaning. Cleaning was accomplished by first washing in soapy water, followed by rinsing and sonication in water. Samples were then sonicated in ethanol. The final treatment of the ITO surface has been shown to be the most important step and various procedures were used following Brumbach *et al*.[14]

ZnO was deposited on ITO from 35mM zinc acetate dihydrate in ethanol at 70°C. The ITO surface was flooded with solution and was then spun at a rate of 2000rpm. The zinc acetate film on ITO was heated at 150°C for 10minutes for conversion to ZnO.

UV/ozone treatment was performed in a Jelight Model 42A UV/ozone chamber (Jelight Co. Inc., Irvine, CA). Spin coating was performed using a Laurell Technologies spin coater Model WS-400BZ-6NPP/LITE. Electrochemistry was performed using a Gamry Reference 3000 potentiostat. UV/Vis spectroscopy was performed using an Ocean Optics DH-2000-BAL light source with a HR4000CG-UV-NIR monochromator.

Molecules used for surface modification are shown in Figure 1. Thiol modification was performed by placing the substrate in 1mM thiol solution in ethanol for 24 hours. 16-phosphonohexadecanoic acid (COOH) modification of ITO was performed with 1mM COOH in $CHCl_3$:C_2H_5OH (2:1) for 2 hours. 4-Nitrobenzenediazonium tetrafluoroborate was electrochemically deposited on ITO by cyclic voltammetry following previous reports.[15-18]

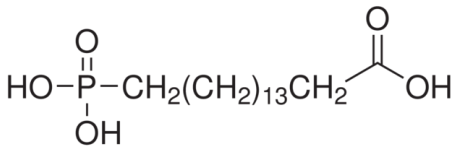

16-phosphonohexadecanoic acid (COOH)

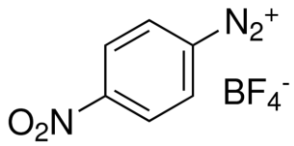

4-Nitrobenzenediazonium tetrafluoroborate (diazonium)

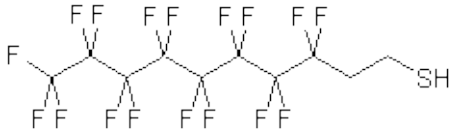

perfluorodecanethiol (C10F8)

hexadecanethiol (C10)

Figure 1. Modification of ITO was performed with 16-phosphonohexadecanoic acid (COOH) to functionalize the surface with terminal carboxylic acid groups. ITO was also modified with 4-nitrobenzenediazonium, loosely termed "diazonium", by electrochemical grafting. The nitro group was used for subsequent conversion to the NH_2 amine and could also be protonated to NH_3^+. Perfluorodecanethiol (C10F8) and decanethiol (C10) were used for SAM modification of gold and ZnO.

Polymers used in this study are shown in Figure 2. Poly(3,4-ethylenedioxythiophene)-poly(styrenesulfonate) (PEDOT) was obtained from Aldrich in high conductivity grade (2.2-2.6% in H_2O). The stock solution was diluted to ¼ volume fraction using distilled water. PEDOT films were deposited via spin coating at various spin rates from 500-8000rpm to obtain desired thicknesses. Annealing was not performed. Poly(3-hexylthiophene) (P3HT) was obtained from Rieke Metals. P3HT films were spun coat from chlorobenzene on ITO. For patterned films of P3HT, films were deposited at either 1000rpm or 2000rpm yielding films of 20nm and 10nm, respectively. The atmosphere during spin coating was either air (40-50% relative humidity) or dry nitrogen (free of oxygen and water). Lines were scribed into the P3HT using a ball-on-disc tribometer to strictly control the line widths. The span between lines could not be easily controlled. The polymer, poly(tris(4-(thiophen-2-yl)phenyl)amine) (N3), is a potential photovoltaic absorber and was described previously.[19] The novel polymer was electrodeposited to give varying thicknesses on ITO.

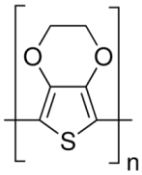

poly(ethylene dioxythiophene) (PEDOT)

poly(aniline) (PANI)

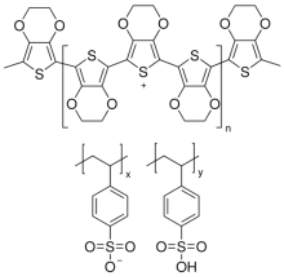

poly(ethylene dioxythiophene)
poly(styrene sulfonate) (PEDOT)

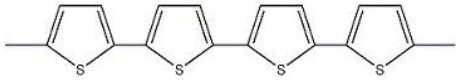

poly(thiophene)

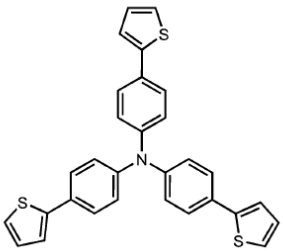

poly(tris(4-(thiophen-2-yl)phenyl)amine) (N3)

poly(3-hexylthiophene) (P3HT)

Figure 2. Polymers used in this study were PEDOT, PANI, poly(thiophene), P3HT, and N3. PEDOT:PSS, when deposited via spin coating, most commonly contains the poly(styrene sulfonate) counterion. In this study, PANI, poly(thiophene), and N3 were deposited electrochemically, while P3HT and PEDOT were deposited via spin coating.

Grids used for shadow mask patterning were copper Veco TEM square mesh grids obtained from Ted Pella, Inc. Outer diameters of grid masks were 3.05mm. Quartz slides were used to hold the grids in place during UV/ozone treatment as described in a later section. For silhouette patterning with nylon, Sefar NITEX woven mesh fabrics were used with square mesh openings of 25µm, 37µm, and 100µm corresponding to open areas of 14-19%, 24%, and 32-44%, respectively.

Titanyl phthalocyanine (TiOPc) and C_{60} were obtained from Aldrich. Films were deposited from vacuum deposition using Knudsen-type cells at a base pressure less than 9 x 10^{-7} torr. A 10 MHz quartz crystal microbalance (QCM) with a frequency counter (Agilent 53181A) and a timing circuit (International Crystal Manufacturing 35360) was used to monitor the rate of deposition. Deposition rates were approximately 3 Hz/s corresponding to temperatures of approximately 450°C and 370°C, for C_{60} and TiOPc, respectively.

13,6-N-sulfinylacetamidopentacene (precursor), obtained from Aldrich, was dissolved in chloroform. The concentrations of solutions were varied and several spin coating rates were attempted to achieve a coating of the film where gold photoemission could still be observed. Samples were placed in vacuum and analyzed for suitability for the experiment. Heating was performed in the Kratos system.

2.2. Analysis Methods

XPS was performed using a Kratos Axis Ultra DLD instrument with a monochromatic Al Kα (1486.6 eV) source. Full survey spectra were collected with an analyzer pass energy of 160 and a step size of 1 eV. High resolution spectra were collected with an analyzer pass energy of 20 and step sizes of 0.1 eV. The analyzer was used in Hybrid mode with a large spot size of 300microns by 700microns elliptically. Imaging XPS was performed with smaller spot sizes. UPS was obtained using an Omicron VUV source HIS13 lamp producing He I (21.2 eV) illumination. The analyzer was operated in UPS mode with a pass energy of 5. A -7V bias was applied to samples for UPS measurements. HAXPES was performed on beamline X24A at the National Synchrotron Light Source (NSLS) at Brookhaven National Labs (BNL). The beamline and end station are discussed extensively in other works.[20-23] Incident energies were selected from 2.2 keV to 4.0 keV as indicated in the respective figures. XPS data were analyzed using CasaXPS. E_F was determined by applying a Heaviside step function to the edge of emission of metallic standards.[24-26] E_F was taken as the kinetic energy of the center of the Gaussian step function and was set to 0 eV (BE) for the corresponding XPS spectra. Imaging NEXAFS was performed on beamline U7A at the National Synchrotron Light Source (NSLS) at Brookhaven National Labs (BNL) and is discussed extensively in other works.[27, 28] Scanning electron microscopy work was completed on a Zeiss Supra 55VP Field Emitter Gun (FEG) SEM. Images were collected using Zeiss SmartSEM software interface. Spectral images from XPS and NEXAFS were analyzed with Sandia's Automated eXpert Spectral Image Analysis (AXSIA) multivariate statistical analysis software.[29-31]

3. SURFACE MODIFICATIONS

3.1. Uniform Surface Treatments

Standard surface modifications were performed with thiols on gold and ZnO, and phosphonic acids on ITO, to establish baseline conditions. Thiol modifications will be discussed in a later section. Figure 3 shows the modification of ITO with 16-phosphonohexadecanoic acid (COOH). This molecule was intended to adsorb with the phosphonic head group anchored to the oxide surface leaving the carboxylic group as the dangling terminal group. This conformation produces a negative dipole at the surface and leads to an apparent increase in work function.[32-34]

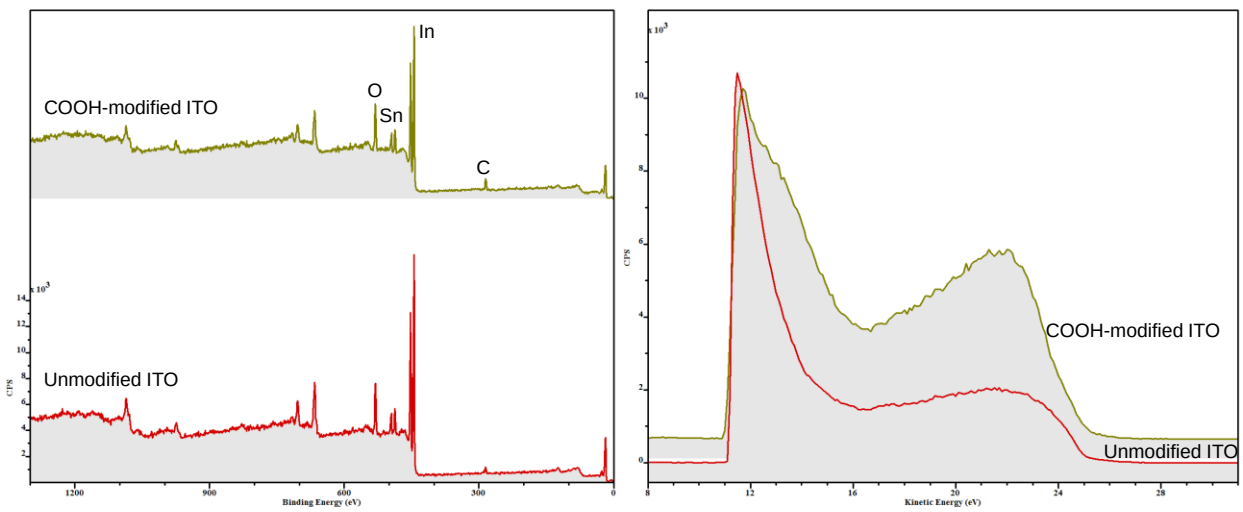

Figure 3. Modification of ITO was performed with 16-phosphonohexadecanoic acid (COOH) to functionalize the surface with carboxylic acid terminal groups. The XPS spectra (left) show an increase in carbon associated with the presence of the SAM on the ITO surface. The UPS spectra (right), show little change in the low kinetic energy edge although there is an increase in emission for the COOH-modified electrode. The lack of a shift in work function suggests heterogeneous orientation of the COOH terminal group in the modifying SAM layer.

XPS results show an increase in total carbon for the COOH-modified ITO surface. There was a shift in the low kinetic energy edge of the UPS spectrum, indicating a small change in apparent work function. However, it could be surmised that the long alkyl chain does not support the alignment of the COOH terminal group outwardly from the surface over large domains. There are likely to be a mixture of orientations of the COOH tail group leading to a lessening of the net dipole at the surface.

Diazonium modification can occur spontaneously for silicon and carbon surfaces, however, the modification can also be controlled by electrochemical deposition for oxides such as ITO.[35] 4-nitrobenzenediazonium is a relatively short, rigid molecule where the ITO surface can directly bond with the benzene ring through either a Sn-C or In-C bond. The nature of the exact bonding between diazonium and ITO is not known. The rigidity of the molecule allows for the organization of the NO_2 groups oriented away from the surface giving an apparent negative dipole at the surface. Additionally, the NO_2 was electrochemically converted to the amine, to

reduce the apparent work function of the surface. By a brief exposure of the amine to acid, the amine could be protonated, yielding an apparent positive dipole at the surface, and a further decrease in apparent work function. The XPS and UPS spectra for diazonium modified ITO surfaces are shown in Figure 4 and 5.

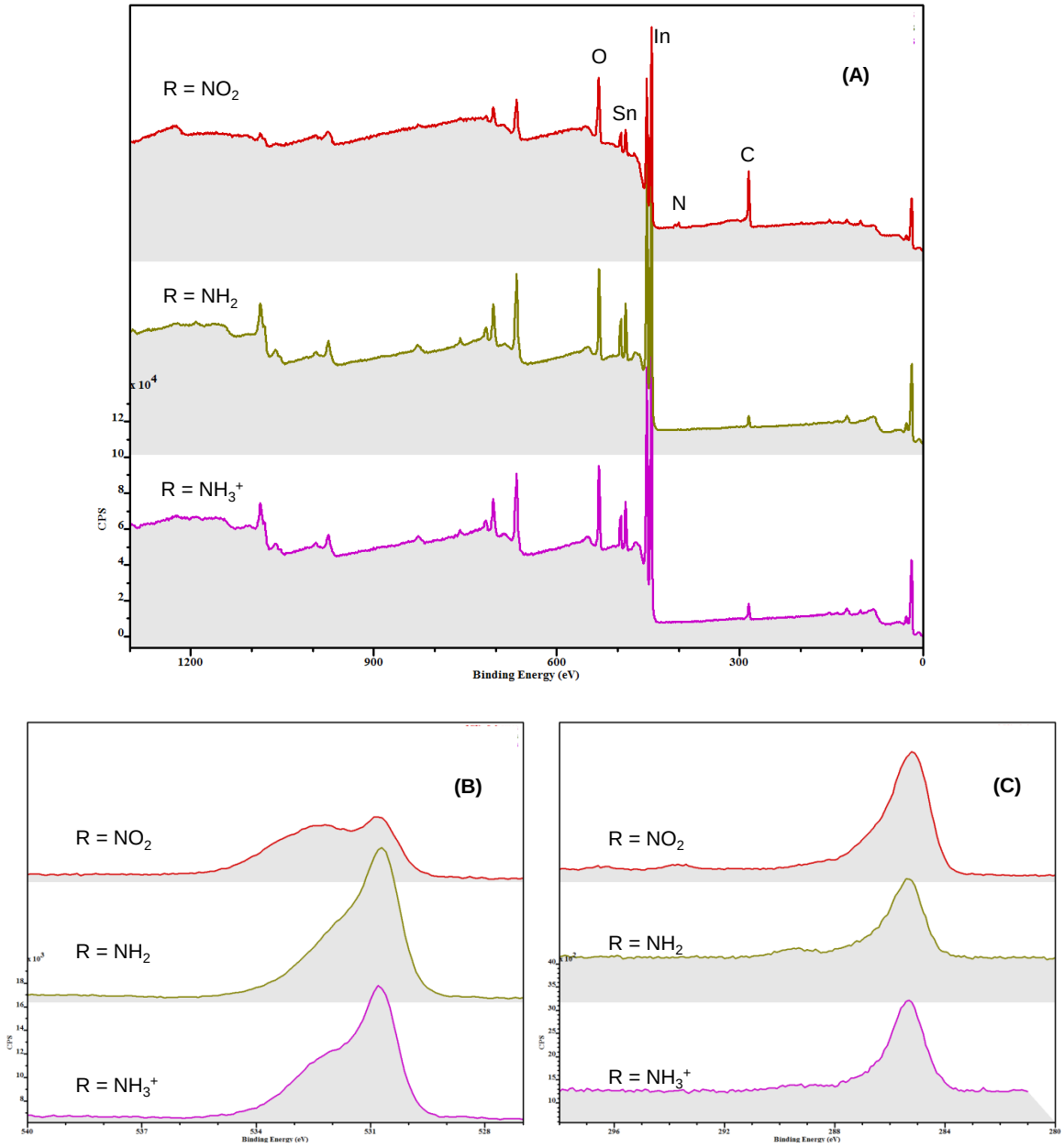

Figure 4. XPS spectra are shown for diazonium modified ITO substrates in (A) survey spectra, (B) O 1s spectra, and (C) C 1s spectra. NO_2 refers to the as deposited nitrobenzene diazonium SAM. NH_2 is the converted amine, while NH_3^+ is the protonated amine. The nitro-diazonium shows an O 1s shoulder form the NO_2 group, which is removed after conversion to the amine.

The nitrogen signal is very weak, due to the low concentration of nitrogen at the surface (one N per anchored diazonium molecule) and the low ionization cross section for N 1s. Consequently,

the changes in the C and O spectra are more revealing showing the change in surface chemistry associated with the respective SAM layers. There is a broad shoulder on the high BE side of the O 1s peak for the NO_2-diazonium modified ITO due to the presence of the NO_2 functionality. The shoulder is absent for the NH_2 and NH_3^+ modifications. The UPS spectra also show distinct shifts in the low KE edge correlating with the surface dipole formation from the terminal functional groups, Figure 5. The work function is lowest for the NH_3^+, followed by NH_2, and highest for NO_2, consistent with the dipoles expected for the respective molecules.

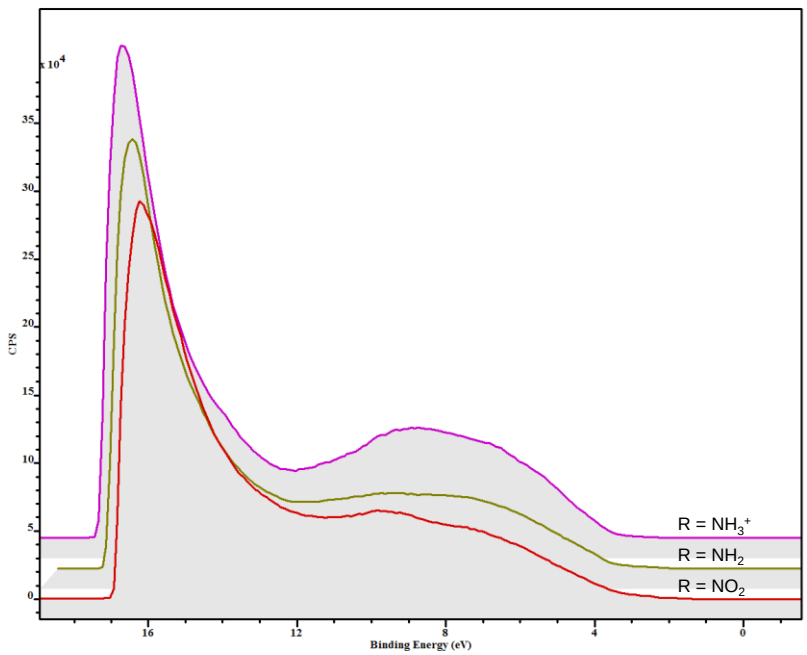

Figure 5. UPS spectra for the diazonium modified ITO show that the work function varies according to the expected dipole for the surface modifying SAM. NO_2 refers to the as deposited nitrobenzene diazonium SAM. NH_2 is the converted amine while, NH_3^+ is the protonated amine terminal functional group. The work function increases according to the shift in the low KE edge of the spectra, $NH_3^+ < NH_2 < NO_2$.

3.2. Patterned Surface Modifications

Given that a cleaned inorganic substrate is usually exposed to ambient lab atmosphere before fabrication of a device, it is reasonable to assume that the surface is in fact heterogeneous, either from heterogeneities of the substrate itself, or through inconsistent manipulation of the substrate prior to deposition of the active layers. The problem of heterogeneous surfaces is becoming increasingly more apparent, particularly for the substrate ITO, were the substrate itself appears to present electronically insulated regions when interfaced with organic layers such as in OPVs and OLEDs.[3, 5] Substrate effects and interfacial contaminants have also been shown to affect the morphology of small molecule and polymer photoactive layers, in devices with ITO or ZnO substrates.[1, 36-38] Consequently, there is practical relevance for studying surface heterogeneity relatable to substrates used in devices.

The use of unimolecular SAMs to tailor the work function and/or chemistry of a surface has been well established. However, the use of mixtures of SAMs has been less routinely performed; and there are even fewer examples of patterned SAMs with full photoemission characterization. From a basic science investigation, it is worthy to evaluate the surface chemistry and work function of pattern geometries and relative areas of coverage of SAMs and mixed SAMs.

The following sections describe several strategies for patterning C10 and C10F8, which have distinctly different molecular dipoles, on gold and ZnO. Shadow mask patterning was used as the basis for most patterning experiments, following the example of Herzer *et al*.[39]

3.2.1. Shadow Mask Patterned Thiols on Gold

Thiols with different dipoles were used to form arrays of patterned SAMs on gold. Thiol modification of gold can be accomplished by soaking the clean surface in a millimolar solution of the respective thiol. Under most circumstances, a close packed monolayer will form within 24 hours. To achieve a pattern of the initial SAM, a shadow mask was used followed by treatment of the surface under UV/ozone to remove all thiol exposed through the open areas of the mask. The resulting patterned thiol could either be retained for analysis or soaked in a second thiol solution to backfill the open areas with a second molecular SAM, as shown in Figures 6 and 7. In addition to varying the sequence of thiol deposition, the size of the patterns and relative areas of coverage were varied using shadow mask grids of various sizes.

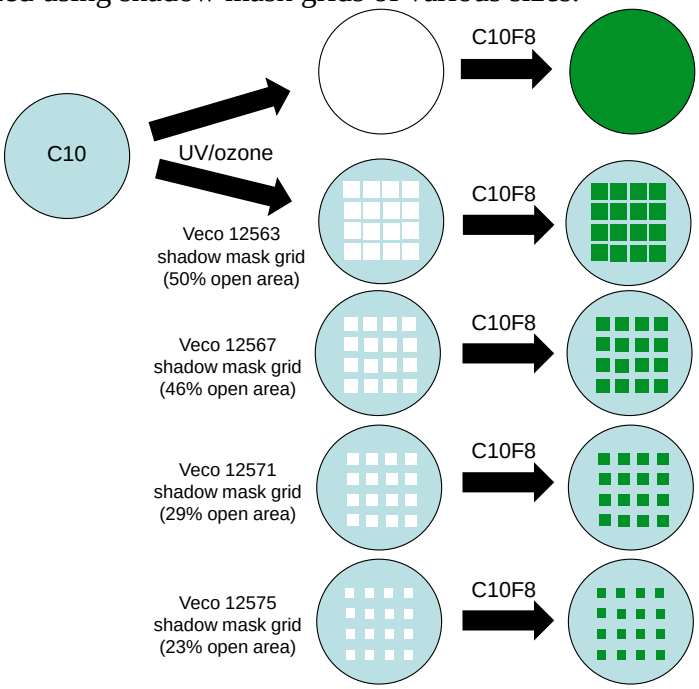

Figure 6. Thiol modification of gold was accomplished by first treating the sample with decanethiol (C10). The sample was then subjected to UV/ozone cleaning with and without shadow masks to remove all thiol from unmasked regions. The patterned C10 was then placed in perfluorodecanethiol (C10F8) to backfill the unmodified regions. This strategy gave patterned C10 SAM layers of varying surface area percentages, as well as patterned C10/C10F8 patterned films with varying surface coverages.

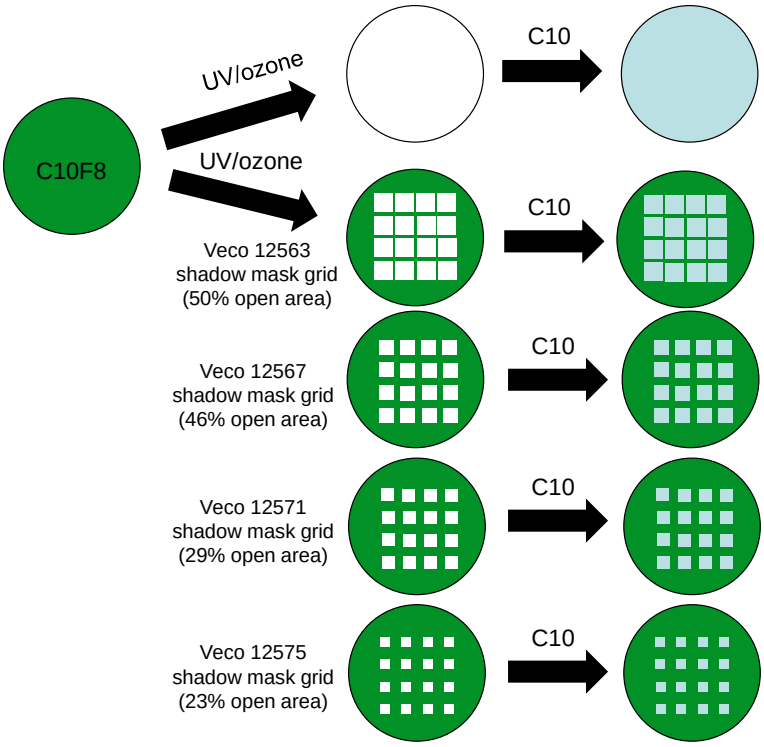

Figure 7. Thiol modification of gold was accomplished by first treating the sample with perfluorodecanethiol (C10F8). The sample was then subjected to UV/ozone cleaning with and without shadow masks to remove all thiol from unmasked regions. The patterned C10F8 was then placed in decanethiol (C10) to backfill the unmodified regions. This strategy gave patterned C10F8 SAM layers of varying surface area percentages, as well as patterned C10F8/C10 patterned films with varying surface coverages.

From Figures 6 and 7 it is indicated that there are multiple samples which can be evaluated as controls. Two samples should have uniform C10 coverage, one sample which was initially modified by C10 and retained for analysis and a second sample which was initially modified by C10F8, but was then treated by UV/ozone, followed by immersion in C10. Ideally, these two samples should show identical XPS and UPS spectra. There was also a complementary set of C10F8 samples following the reverse deposition steps of that of the C10 samples. The UPS spectra for these control samples are shown in Figure 8. The UPS data for control samples, with several repeat analyses, are summarized in Table 1.

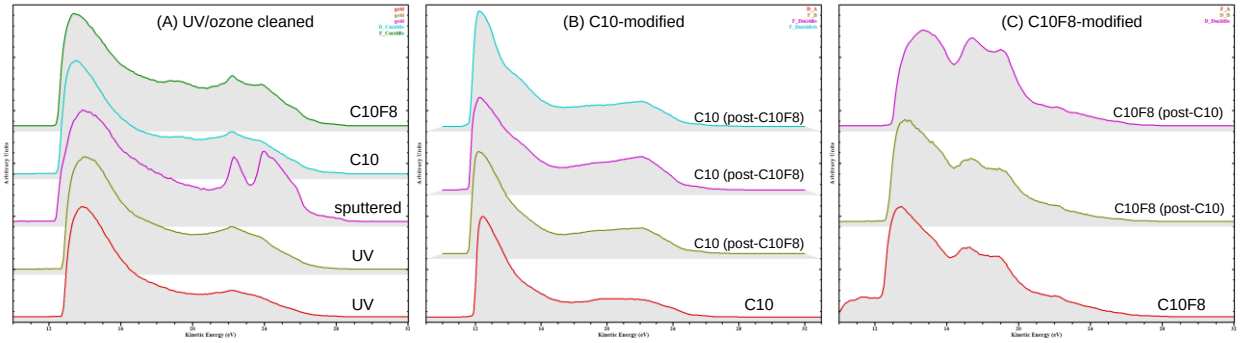

Figure 8. UPS spectra are shown for cleaned and modified gold control samples. (A) Spectra are shown for two gold samples which have been UV/ozone cleaned and one sample which was sputtered. Spectra are also shown for samples modified with either C10 of C10F8 SAM with subsequent UV/ozone cleaning to remove the SAM. (B) Spectra are shown for a C10 modified gold surface as well as three spectra for C10 modification after a C10F8 SAM was removed via UV/ozone cleaning. (C) A UPS spectrum is shown for a C10F8 modified gold surface as well as two spectra for C10F8 SAMs deposited after a C10 SAM was removed.

Figure 8A shows the UPS for gold which has been sputtered cleaned and two samples which have been UV/ozone cleaned. Also shown are the spectra for samples which were treated with either C10 or C10F8 followed by UV/ozone cleaning of the SAM-modified surface. Ideally, the spectra from these two samples should resemble that of the UV/ozone cleaned gold. Both the C10-UV treated and C10F8-UV treated samples show several distinct features disparately from the UV-treated bare gold. This is a good indication that the UV/ozone treatment of the SAM modified surfaces does not completely remove the SAM layers. The UPS spectra for C10 modified gold samples are similar despite the sequence of deposition steps, Figure 8B. Similarly, the C10F8 modified gold samples show similar spectra to one another, although there appears to be more variation in peak intensities due to the overall greater absolute values of intensity, Figure 8C.

Work function values, summarized in Table 1, show the same trends as discussed above. The work functions of all UV/ozone cleaned samples are similar, regardless of any previous SAM modification. Work function values of C10 samples were slightly lower for the post-C10F8 samples. Alternatively, the C10F8 samples, that were post-C10, generally showed a higher work function than for the initial C10F8 modified sample. These work function values are all much higher than would normally be expected for pure gold, however, the gold work function (0% modified area) was also quite high, around 5.7eV. Since the substrates were thin films of gold on quartz, there may be some difference in the conductivity of the substrate which is giving erroneous WF values relative to the literature value for pure gold, 5.1eV. For this study the values are self-consistent and can be evaluated on a relative basis.

Figures 9 shows the XPS spectra for the C 1s from the various SAM modified gold samples. When C10 was deposited after removing a C10F8 SAM, a narrower and more intense C 1s peak was observed indicating a more compact C10 film. No indication of a C-F bond was observed. When the C10F8 was deposited after the C10 layer was removed, a greater C-F contribution was observed in the total C 1s spectrum. This suggests that better coverage of the respective SAMs is obtained when an initial SAM is removed.

Table 1. Work function values for gold surfaces with and without SAM modifications. C10 and C10F8 were both deposited on initially clean surface as well as on surface which had been previously modified with the alternate thiol.

	WF (eV)
sputtered	5.2
plasma cleaned	5.6
plasma cleaned	5.6
plasma cleaned (post-C10)	5.7
plasma cleaned (post-C10F8)	5.7
C10	5.0
C10 (post-C10F8)	4.8
C10 (post-C10F8)	4.7
C10 (post-C10F8)	4.8
C10F8	5.8
C10F8 (post-C10)	6.0
C10F8 (post-C10)	6.3

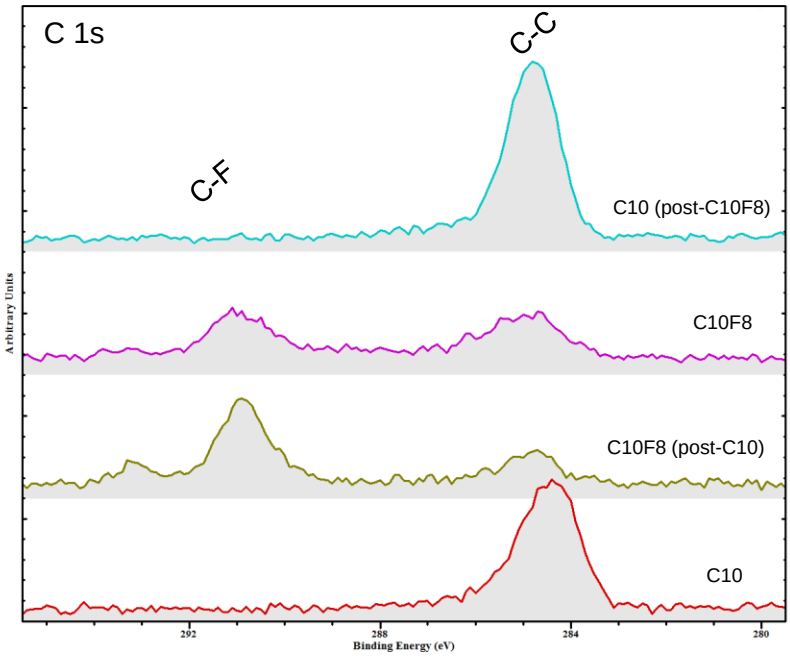

Figure 9. C 1s spectra are shown for control samples where C10 was deposited initially (C10), and where C10 was deposited after a C10F8 SAM was removed (C10(post-C10F8)). C10F8 was also deposited initially (C10F8), as well as deposited after a C10 SAM was removed (C10F8(post-C10)). The C 1s is more intense and narrower for C10 films modified after C10F8 relative to the as-deposited C10 film. The components at high BE, corresponding to C-F, are more pronounced for the C10F8 deposited after the C10 SAM was removed. These results show that a more compact SAM was obtained after an initial SAM was deposited and removed.

The work function values also support this trend, since a lower work function was observed for C10 deposited post-C10F8, indicating a better oriented C10 film. Similarly, a higher work function was observed for the C10F8 SAM deposited post-C10.

Figure 10 shows the UPS spectra for patterned thiol SAMs. The percentages relate to the percent of SAM modified area. The remaining area was UV/ozone treated by exposure through the shadow mask. In general the lineshape of the UPS spectra did not change as a function of the area of SAM coverage.

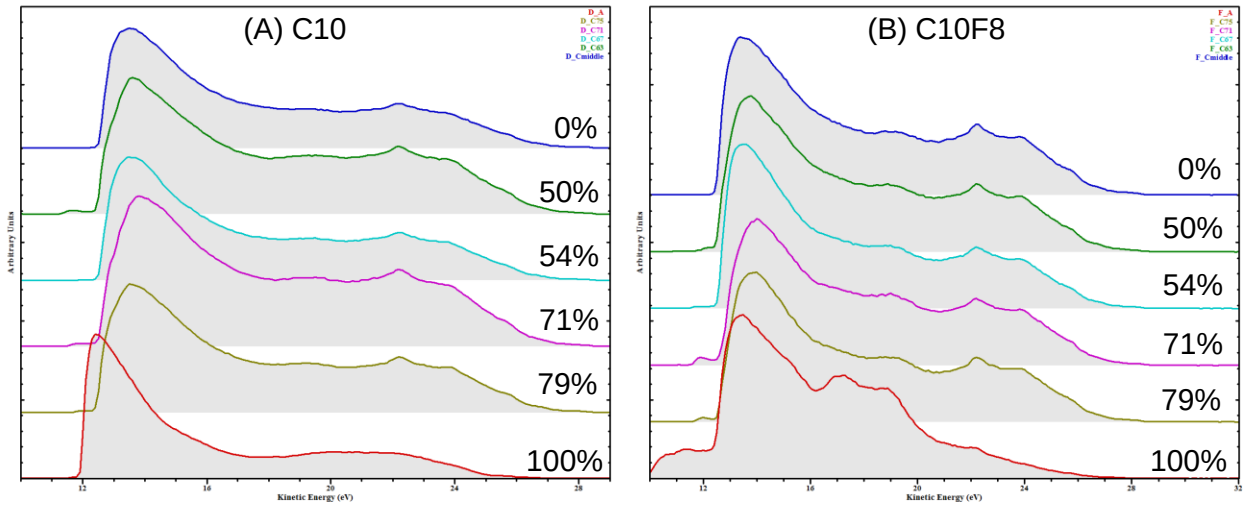

Figure 10. UPS spectra from (A) decanethiol (C10) and (B) perfluorodecanethiol (C10F8) modified gold. The percentages show the area of surface modification by the respective SAM. The remaining area was UV/ozone cleaned in the etching process.

The dipole for the C10F8 molecule is significantly greater than that of C10 and should modify the surface of gold with a much higher apparent work function. Figure 11 shows that the work functions for C10F8 modified gold are nearly 1eV greater than that of the C10 modified surface. Interestingly, however, as the area of surface modification decreases the work function values converge to more similar values between 5.5eV and 6.0eV.

Figure 11 also shows the change in percent composition of fluorine for the C10F8 modified surface. The C10 samples did not show any evidence of fluorine. The 100% C10F8 SAM shows a high F content, as expected. As the area of modification was decreased, the concentration of fluorine reached a nearly identical value across all patterned samples.

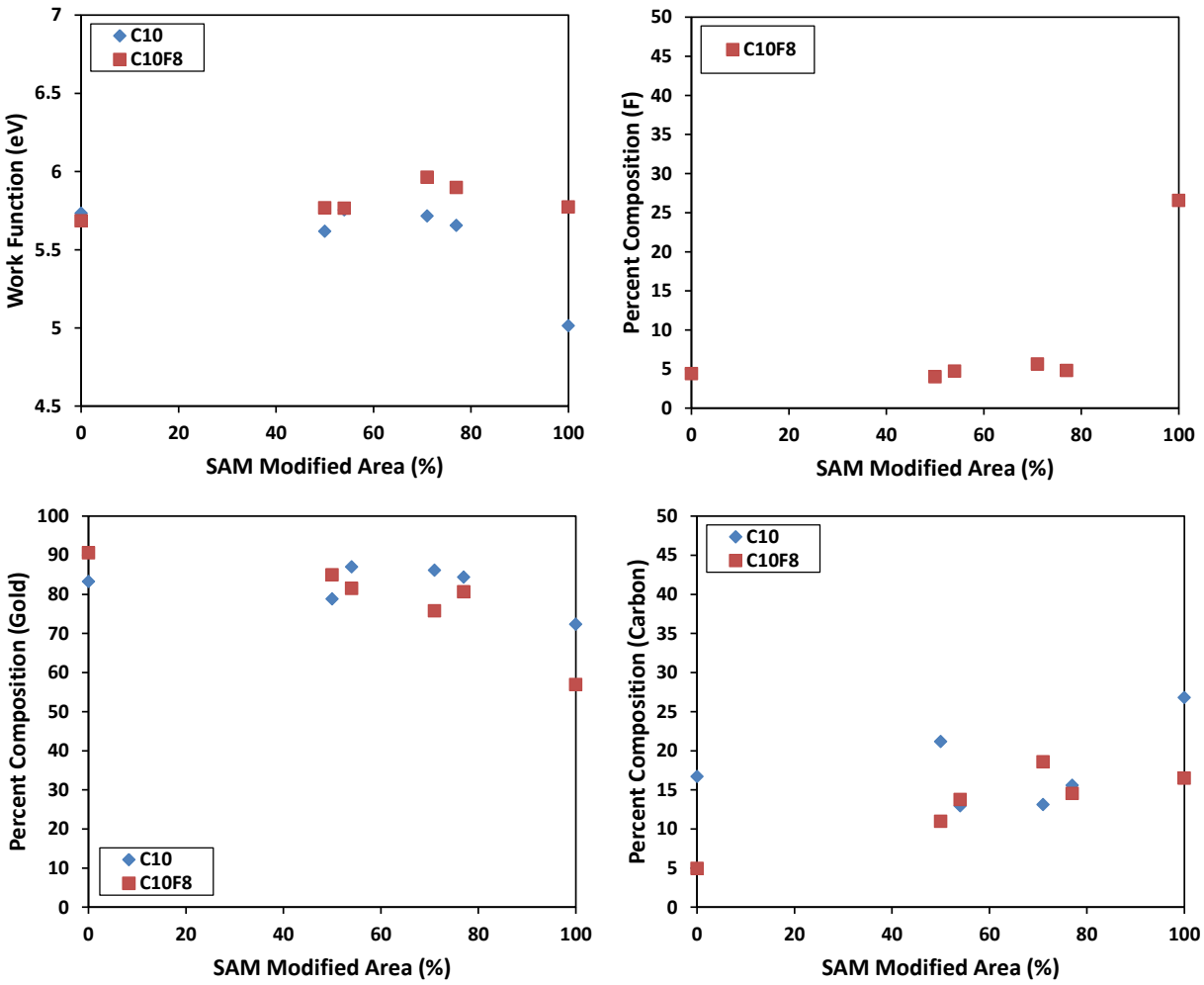

Figure 11. (Upper left) Work function is shown for the C10 and C10F8 SAM films as a function of the area of surface modification. (Upper right) The percent composition of fluorine is shown for the C10F8 sample as a function of the modified surface area. C10 did not show any evidence of fluorine. (Lower left) The percent composition of gold is shown versus the area of modification for the two SAM films. A linear relationship would be expected. (Lower right) The percent composition of carbon is shown versus the area of modification.

Gold and carbon concentration show some linearity across the modified areas as would be expected, Figure 11. The gold concentration drops off more sharply for the C10F8 sample, relative to the C10 sample, as more of the area is modified with the SAM since the C10F8 also introduces F which is accounted for in the percent compositional analysis.

C 1s spectra from XPS for the variously modified gold samples, Figure 12, show that the decanethiol SAM is preserved across the variously patterned C10 samples. The C 1s from C10F8 modified samples show that the C-F component is removed after UV/ozone treatment indicating that, although fluorine is still present (Figure 11), the nature of the perfluorodecanethiol molecule may have been altered even in the masked regions.

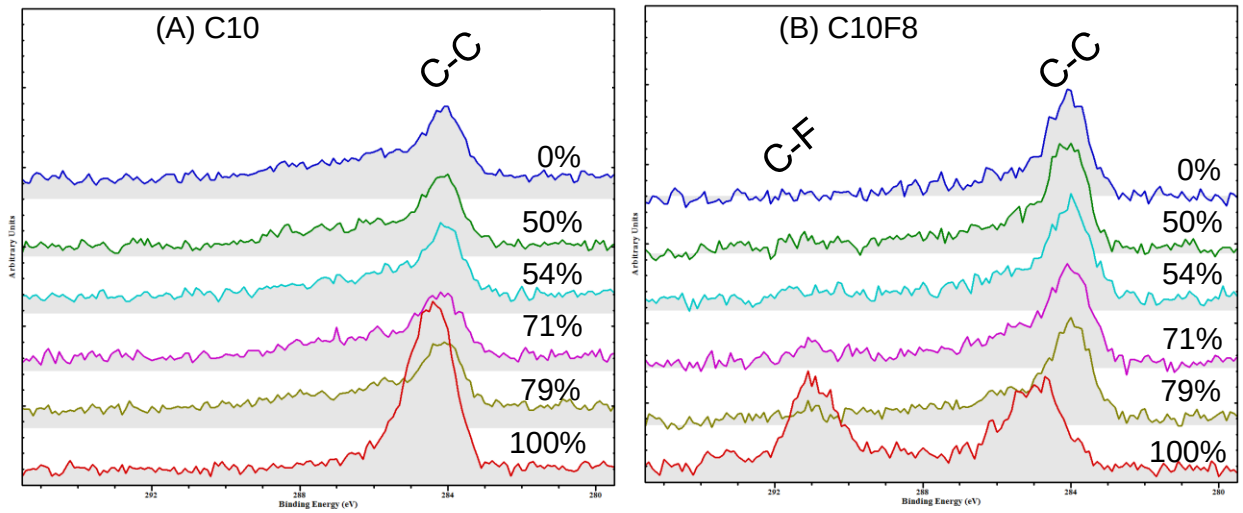

Figure 12. (A) The C 1s spectra for C10 modified gold are shown for the various areas of modification as indicated. (B) The C 1s spectra for C10F8 modified gold are shown for the various areas of modification. The C-F component at high binding energy is only observed for the 100% modified sample.

Figure 13 shows the UPS spectra for the patterned bimolecular SAMs (PB_SAMs) where the percentages relate to the expected areas of C10 coverage and the remaining area is the C10F8 coverage. C10 in the lines indicate that C10 was the first SAM deposited and was masked by the various grids prior to UV/ozone treatment. C10F8 was then backfilled into the open areas of the pattern, i.e. the holes in the mask. Alternatively, the spectra in Figure 13B are from samples were C10 was deposited after UV/ozone removal of C10F8 giving C10 in the holes and C10F8 along the lines of the grid mask pattern.

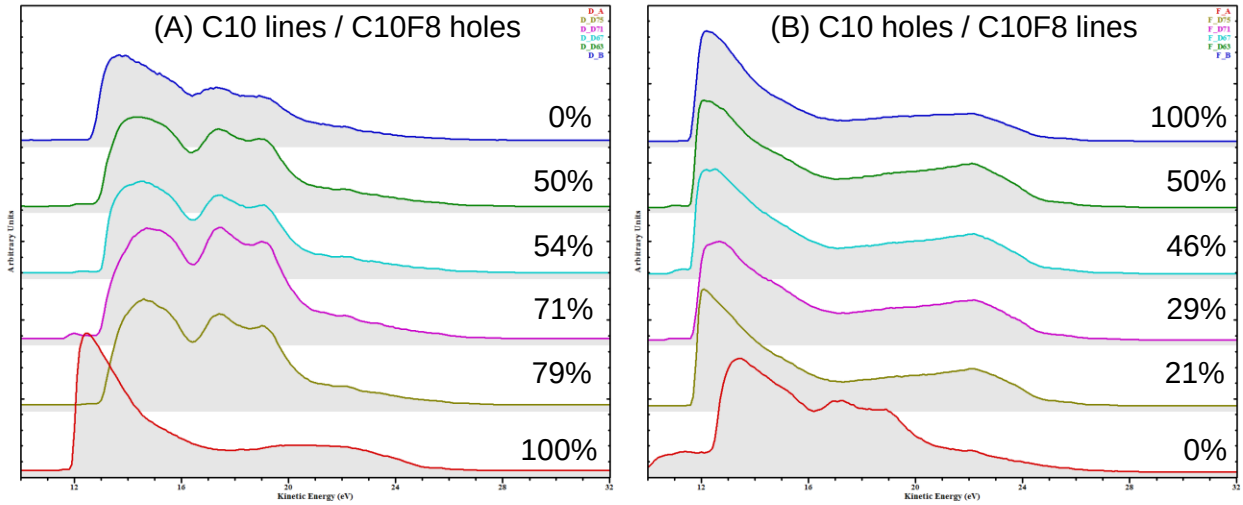

Figure 13. UPS spectra are shown for patterned bimolecular SAMs. The percentages show the expected area of C10 modification where the remaining area was modified by C10F8. Cases where C10 was patterned in the lines of the mask pattern are from initial C10 deposition followed by UV/ozone cleaning through the mask and C10F8 deposition. C10F8 in the lines was performed first followed by C10 backfilling.

The work function and changes in composition are shown for the PB_SAMs in Figure 14. The regions where C10 was backfilled into the patterned C10F8 show the lowest work function of all of the samples in this study.

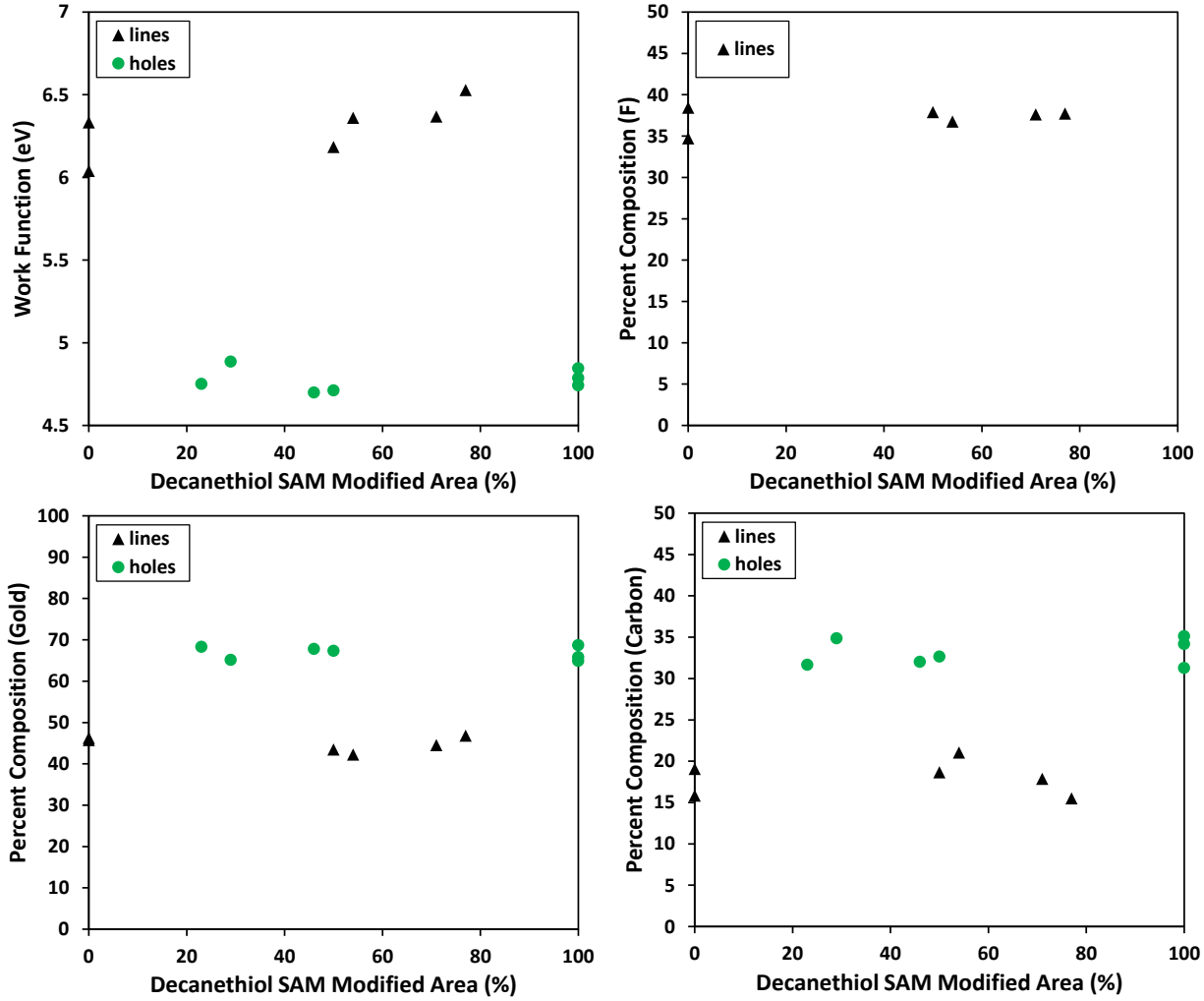

Figure 14. Patterned bimolecular SAMs (PB_SAMs) show distinct differences in work function and percent composition. Values are shown for C10 coverage either in the holes or lines of the mask pattern, with C10F8 filling the remainder of the surface area. (Upper left) The work function is shown as a function of the area of surface modification expected from the geometry of the shadow mask. (Upper right) The percent composition of fluorine is shown for the case where C10F8 was backfilled into the holes of the C10 line pattern. When C10 was backfilled into the C10F8 line pattern, there was no evidence of fluorine. (Lower left) The percent composition of gold is shown versus the area of C10 modification. Since the full surface of the gold substrate should be coated with a SAM, the concentration of gold should not change significantly. (Lower right) The percent composition of carbon is shown versus the area of C10 modification.

As with the samples where only a single molecular species was expected on the patterned samples, the PB_SAMs seem to indicate that UV/ozone treatment has induced an altercation of the SAM layers. C 1s spectra were again used as to evaluate changes in the SAM layers. Figure

15A shows the presence of C-F constituents indicating that C10F8 successfully backfilled the open areas of the patterned C10 SAM. No C-F components were observed where C10 was used to backfill patterned C10F8, Figure 15B. C10 appears to have completely displaced the C10F8 SAM in the case where C10F8 was UV/ozone patterned.

It is worth noting that sulfur was observed for all samples. However, there was only one sulfur atom per molecule and the intensity of the sulfur peak was extremely low.

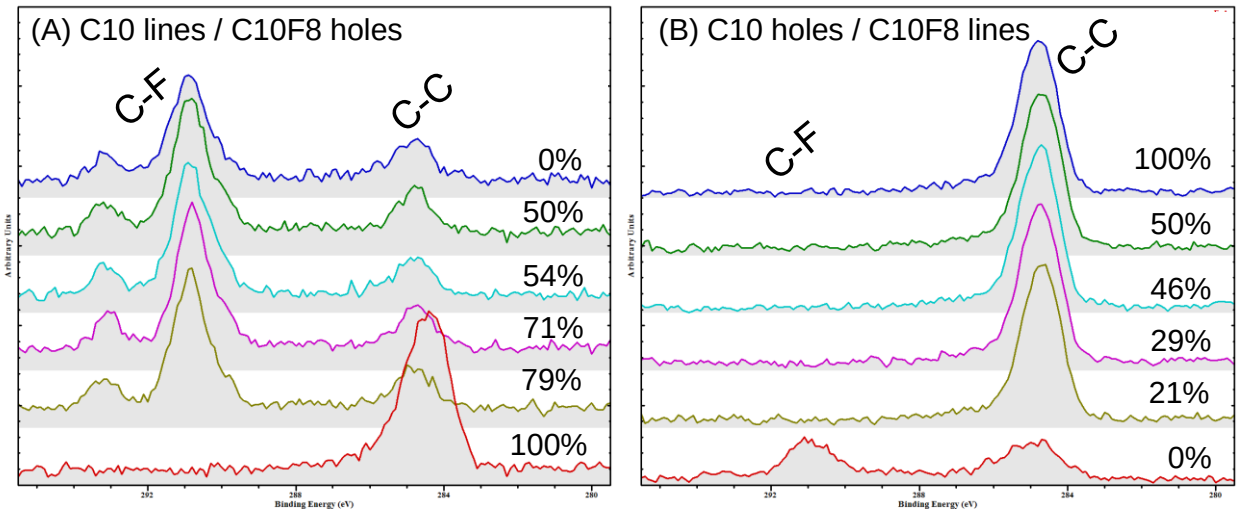

Figure 15. (A) The C 1s spectra are shown for the various areas of C10 modification where C10 was patterned first and backfilled by C10F8. The C-F components at high BE are clearly observable when C10F8 was deposited into the holes of the C10 pattern. (B) The C 1s spectra are shown for the various areas of C10 modification where C10F8 was patterned first followed by backfilling with C10. No indication of C-F bonds from C10F8 are observed.

Attempts at XPS imaging did not reveal any pattern on the respective surfaces. However, given the dimensions of the pattern and the unavoidable presence of contaminants, it is not surprising that the imaging capability of XPS could not resolve a pattern. Imaging of a monolayer molecular film is not trivial, and the *ex situ* preparation and scale of patterning make the analyses even more difficult. To confirm the existence of a pattern, NEXAFS imaging was used. NEXAFS images were obtained for C10-line patterns with C10F8 backfilling the open regions, Figure 16. The presence of a grid pattern was observed in the NEXAFS image. A chemical contrast between the lines of the shadow mask, where C10 should have been retained, and the open areas, which should have been modified by C10F8, could be observed. These samples were exposed to air for several days prior to analysis and were unavoidably exposed to ambient conditions. Consequently, the pattern was not observed across the full width of the shadow mask patterned region, but this may be due to the presence of adventitious contaminants obscuring the contrast of the underlying SAM layers. The NEXAFS imaging spectrometer also produces inconsistent illumination across the large area of analysis giving a saturation of intensity towards the middle of the field of view. A more surface sensitive image was obtained, Figure 17, by applying a higher bias to the grid at the entrance to the partial electron yield detector.[40] The contrast of the image lessens the grid biases were increased to obtain more surface sensitive NEXAFS images. A NEXAFS image was also obtained for a specimen where C10F8 was

shadow mask patterned and the open areas were left unmodified, Figure 18. A high contrast image was observed showing the retention of C10F8 along the lines of the shadow mask pattern.

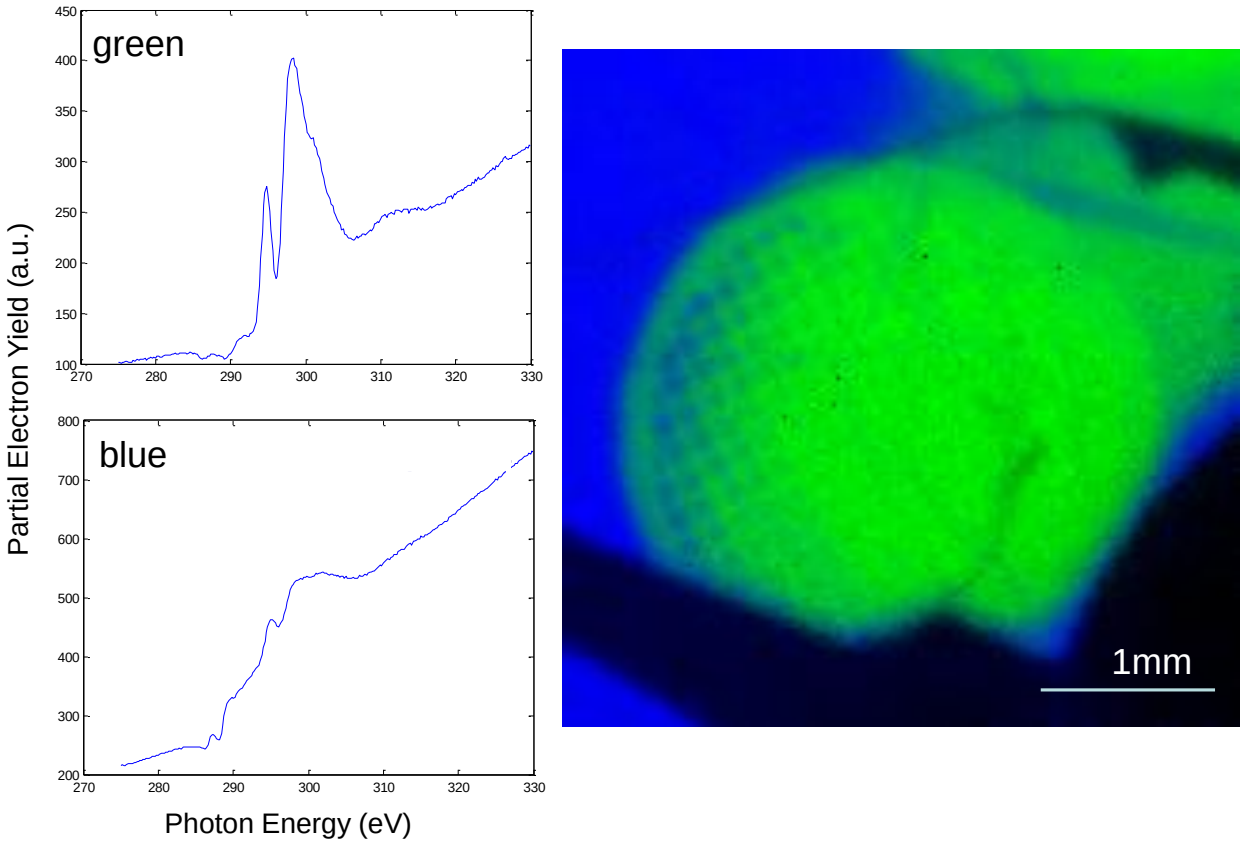

Figure 16. A NEXAFS image is shown for a sample where C10 was initially patterned in the lines of the grid shadow mask and C10F8 was backfilled into the open areas. Black areas are from gold delamination from the quartz substrate. A -100V bias was applied to the grid at the entrance to the partial electron yield detector.

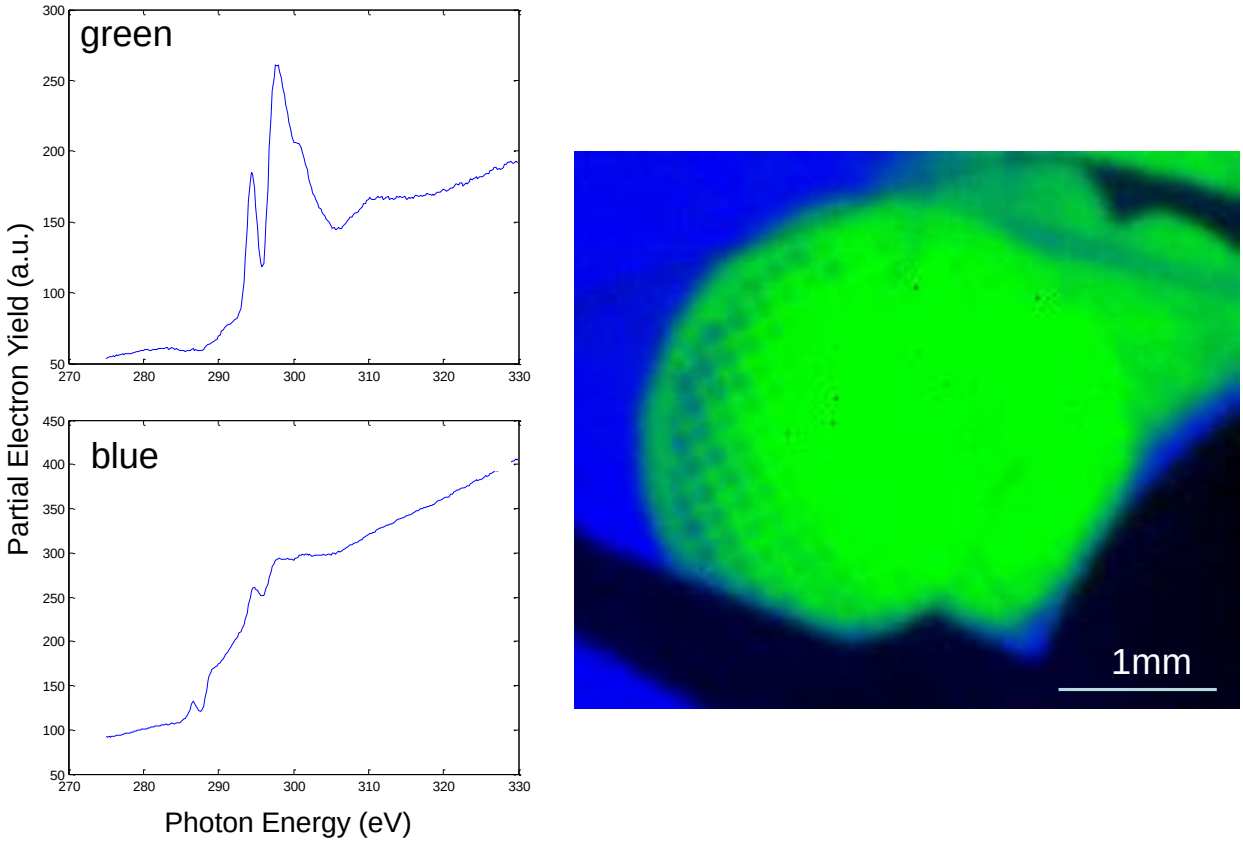

Figure 17. A NEXAFS image is shown for a sample where C10 was initially patterned in the lines of the grid shadow mask and C10F8 was backfilled into the open areas. Black areas are from gold delamination from the quartz substrate. A -150V bias was applied to the grid at the entrance to the partial electron yield detector, making the measurement slightly more surface sensitive than the previous Figure.

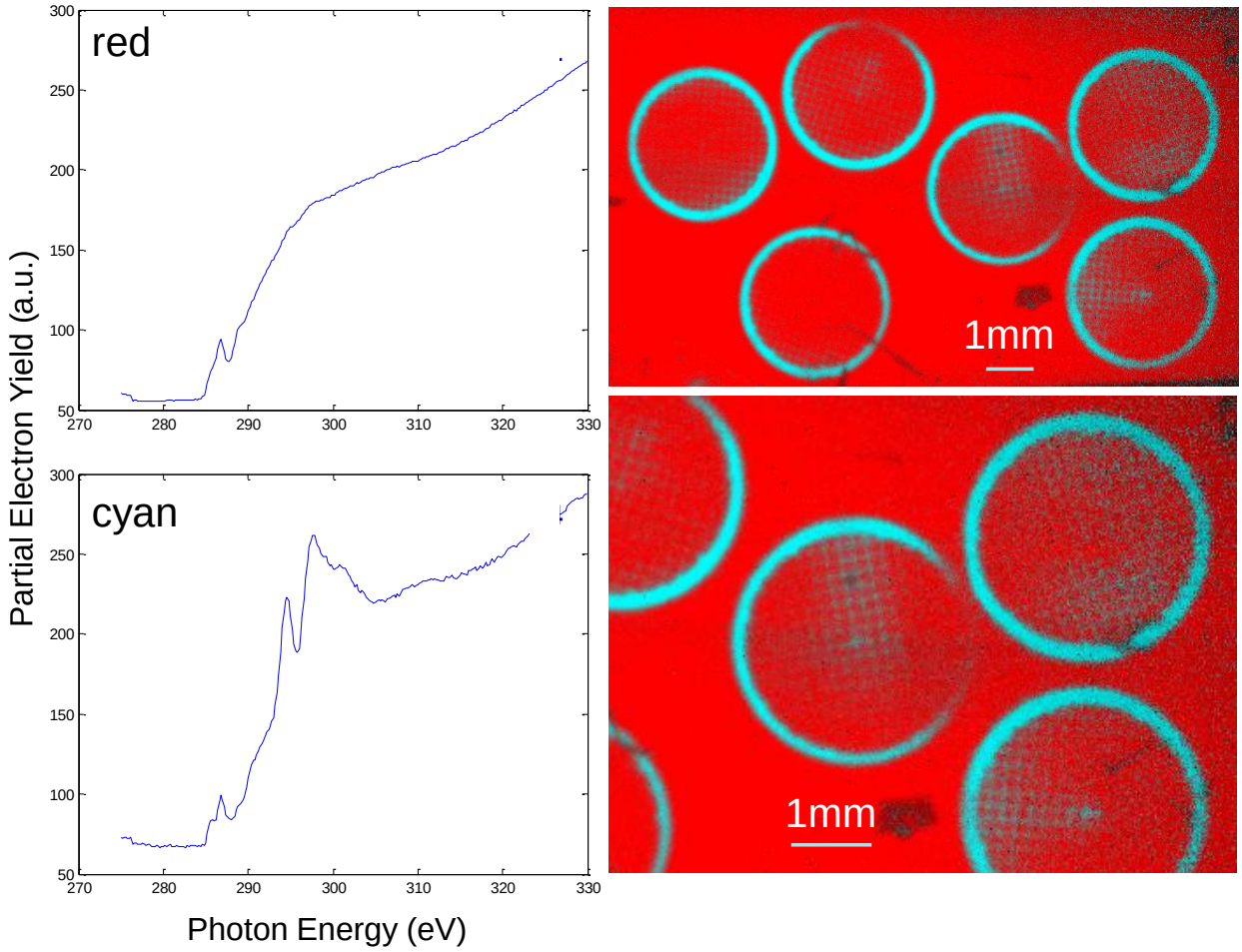

Figure 18. A NEXAFS image is shown for a sample where C10F8 was initially patterned in the lines of the grid shadow mask and the open areas were left unmodified. A -150V bias was applied to the grid at the entrance to the partial electron yield detector. The lower right figure is a blow up of the upper right figure.

A sample was evaluated using NEXAFS imaging where C10F8 was initially shadow mask patterned and was then backfilled by C10, Figure 19. This gave no contrast in NEXAFS imaging indicating that there was probably no pattern retained. As was alluded to previously by XPS, the shadow mask patterning of C10F8 and subsequent backfilling with C10, appears to displace any C10F8 with C10. The fact that C10F8 can be observed in a patterned NEXAFS image, Figure 18, indicates that the C10F8 is present prior to C10 backfilling.

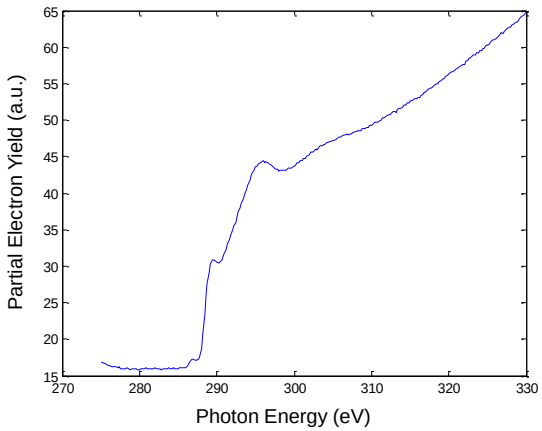

Figure 19. A NEXAFS spectrum is shown for a sample where C10F8 was initially patterned by UV/ozone followed by backfilling with C10. A -150V bias was applied to the grid at the entrance to the partial electron yield detector. No contrast was observed in the corresponding NEXAFS image to indicate a patterned SAM.

3.2.2. Silhouette Patterning Using Nylon Shadow Masks

The procedure for the grid shadow masks discussed above yielded small domains of patterned thiols on gold. These domains could be targeted for analysis in XPS and NEXAFS, but it would be preferable to mask large areas of the sample such that the substrate is uniformly modified and the patterned region does not have to be strictly located for analysis. Large area mask patterns with micron scale features as a readily available, cheap, high volume material would be ideal. Additionally, a material that could act as the mask, while also adding functionality, would offer an advantage over a static masking component. Nylon is known to react under UV exposure[41, 42] and nylon can be cheaply manufactured in large quantities in micron sized woven mesh fabrics. It was attempted to use nylon mesh screens with various sized openings as the reactive shadow mask. C10 and C10F8 thiols were deposited on ZnO and were subsequently patterned using nylon mesh screens. Since the screen is not fully opaque to the UV illumination and is expected to play a reactive role in the patterning process, the following method will be described as silhouette mask patterning to differentiate it from the shadow mask patterning discussed above.

Work function values for ZnO cleaned via ethanol, modified by C10, and modified by C10F8 are shown in Table 2. UV/ozone cleaning of bare ZnO led to a small increase in WF relative to the solvent cleaned sample. This is consistent with other reports of ozone cleaning on oxide surfaces, likely due to oxidation of the surface and contaminant species.[14, 43-45] C10F8 modification led to a large increase in WF, as expected, while C10 decreased the WF. All ozone cleaned samples, without nylon present, showed the same WF value. Silhouette patterning was performed on the three variously treated surfaces using three different mesh sizes. For the ethanol cleaned and C10-modified samples, the presence of the nylon mask had no effect on apparent WF of the ZnO. The WF values were, however, still lower than for the case where no nylon mask was present. For the C10F8 samples, the presence of the silhouette mask led a decrease in WF, but the WF was still higher than for C10-modified and unmodified ZnO.

Table 2. Work function values for thiol modified ZnO films via silhouette patterning. The openings of the nylon square mesh are indicated, where UV/ozone treatment was performed to pattern through the silhouette mask. Solvent cleaned, C10, and C10F8 were not UV/ozone treated.

	naming abbreviations	**WF (eV)**
Ethanol cleaned		
UV/ozone cleaned	Ethanol_ozone cleaned	**4.3**
25 micron	Ethanol_25	**4.0**
37 micron	Ethanol_37	**4.1**
100 micron	Ethanol_100	**4.0**
Solvent cleaned	Ethanol cleaned	**4.1**
C10 modified		
UV/ozone cleaned	Decane_ozone	**4.3**
25 micron	Decane_25	**4.0**
37 micron	Decane_37	**3.9**
100 micron	Decane_100	**4.0**
C10	Decanethiol	**4.0**
C10F8 modified		
UV/ozone cleaned	Fluoro_ozone	**4.3**
25 micron	Fluoro_25	**4.3**
37 micron	Fluoro_37	**4.3**
100 micron	Fluoro_100	**4.3**
C10F8	Perfluorodecanethiol	**4.9**

During the silhouette masking process, the UV/ozone treatment alters the exposed SAM while the nylon undergoes some degradation and can thereby alter the SAM beneath the mask. To evaluate the surface chemistry of residual species altered and/or deposited by the silhouette masking process, XPS analyses were performed. Figure 20 shows the C 1s and O 1s spectra for all samples. The presence of the C10 SAM is clearly evident by the C 1s spectrum shown in Figure 20B with a sharp and intense peak. C10F8 is also clearly evident on the C10F8 sample, Figure 20C, with a distinct component at high BE indicative of the C-F bonds. After UV/ozone treatment in the presence of the nylon silhouette masks, the C 1s spectra for cleaned ZnO and C10-modified ZnO become very similar. A peak is observed at approximately 286eV for C-C components, but an additional peak is observed at high BE, around 290eV, possibly due to C-N, C-O, and/or C-S species. (Peaks are shifted approximately 2eV to higher BE in these spectra due to some charging.) The similarity between C 1s for silhouette patterned cleaned-ZnO and C10-modified ZnO suggest deposition of material from the nylon onto these samples. For the C10F8-modified ZnO, the silhouette patterning does not completely remove C-F components. The O 1s spectra give a similar trend as observed via C 1s spectra, where the patterning process gives nearly similar spectra regardless of the mesh size. A component at higher BE to that of the Zn-O component, grows in intensity with UV/ozone treatment, due to additional oxidized species.

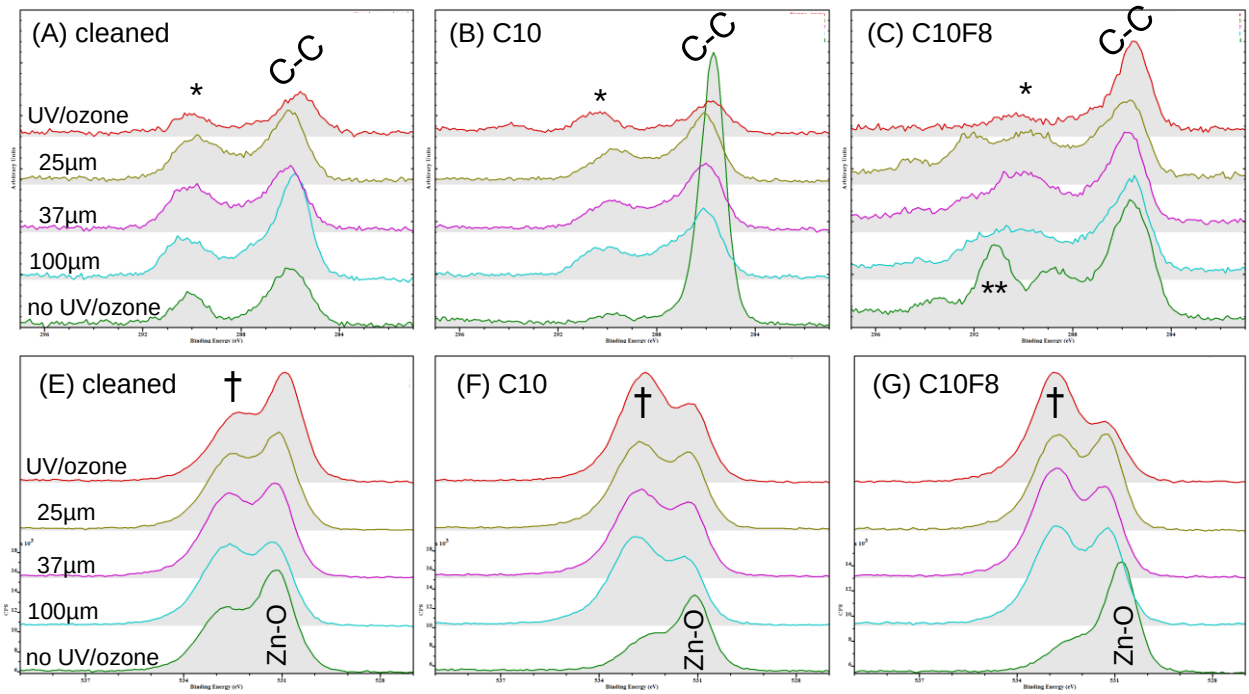

Figure 20. XPS spectra are shown for silhouette patterned ZnO samples. A,B, and C show the C 1s spectra for the indicated specimens. E, F, and G show the O 1s spectra. The (*) indicates carbon environments such as C-S, C-N, or C-O. The (**) is a C-F component. For O 1s, the primary component at lower BE is the oxide component, while the peak at higher BE (†) is from additionally oxidized species.

The S 2p and N 1s spectra are shown for all samples in Figure 21. Sulfur was present on all ethanol cleaned ZnO samples. This correlates with the C 1s peak observed at high BE in Figure 20A. Sulfur was observed at low BE for the thiol modified ZnO samples, indicating the presence of the thiol. After UV/ozone treatment, with or without the presence of the nylon mask, the S 2p peak shifted to higher BE and was nearly the same intensity regardless of the mesh size. Sulfur appears to be present in the deposited ZnO film, likely as a ZnS impurity. Nitrogen was not observed on any of the substrates until after UV/ozone treatment in the presence of the nylon mask. This is a clear indication that the nylon degradation under UV exposure deposits byproducts on the ZnO surface. Evidence of these byproducts are additionally observed in the C 1s and O 1s spectra, Figure 20.

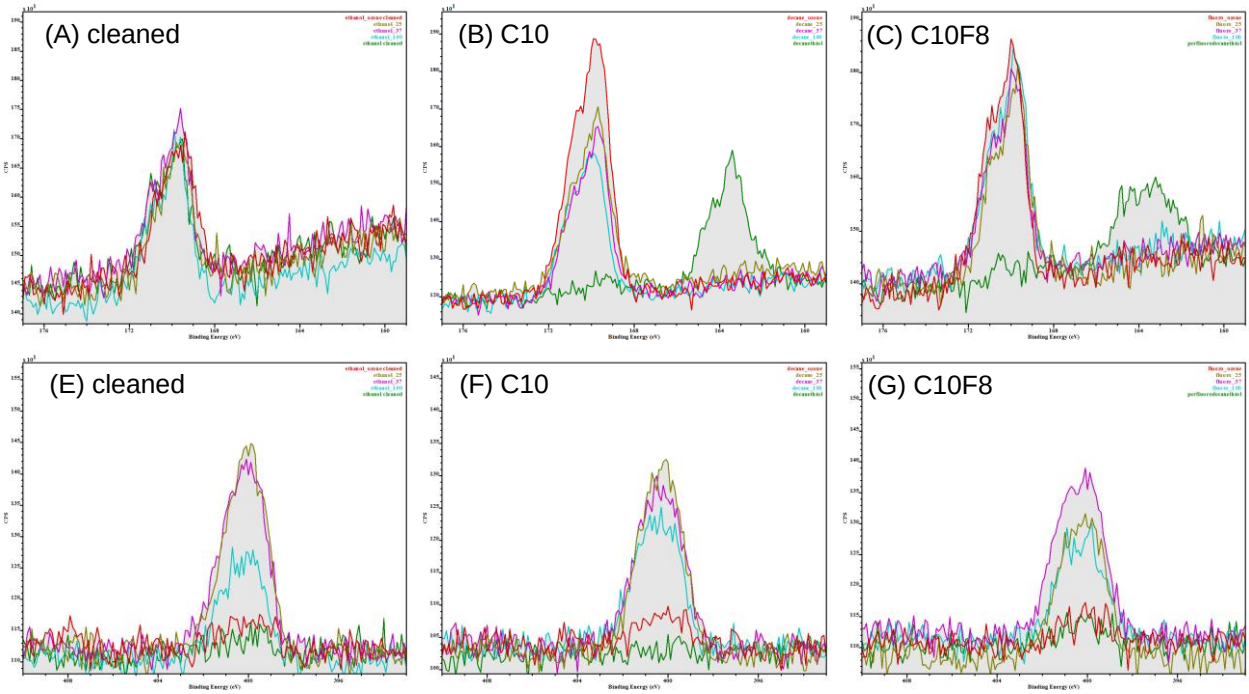

Figure 21. XPS spectra are shown for silhouette patterned ZnO samples. A,B, and C show the S 2p spectra for the indicated specimens. E, F, and G show the N 1s spectra.

Fluorine was only observed on the samples modified by C10F8, Figure 22. Fluorine was retained on the C10F8-modified sample which was completely exposed to UV/ozone treatment. This is contrary to what was observed for the C10F8-modified gold samples discussed above where UV/ozone removed the C10F8 signature from the gold surface. Two F 1s peaks are observed in the F 1s spectra from the ZnO surfaces. This may be due to some inconsistency in the underlying ZnO substrate. The F 1s spectra are consistent with the changes in the C-F component observed in the C 1s spectra, Figure 20C.

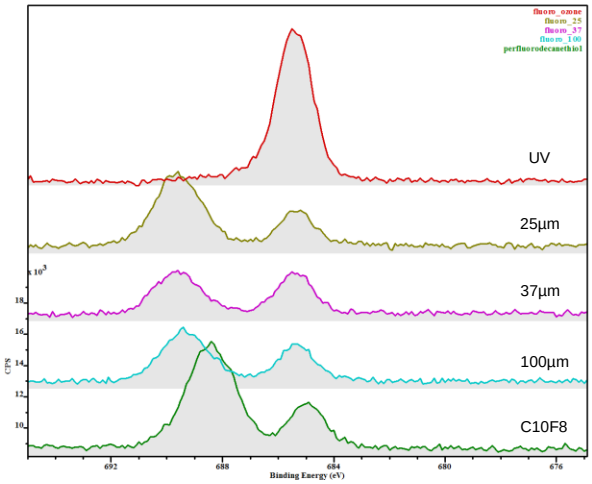

Figure 22. F 1s spectra are shown for C10F8 silhouette patterned ZnO samples.

UPS spectra for the silhouette patterned ZnO samples are shown in Figure 23. The spectra are nearly identical for all ethanol cleaned ZnO samples. C10-modified samples show such a low work function that the low KE edge appears to be cut off, giving nearly the same WF for all silhouette patterned C10-modified samples.

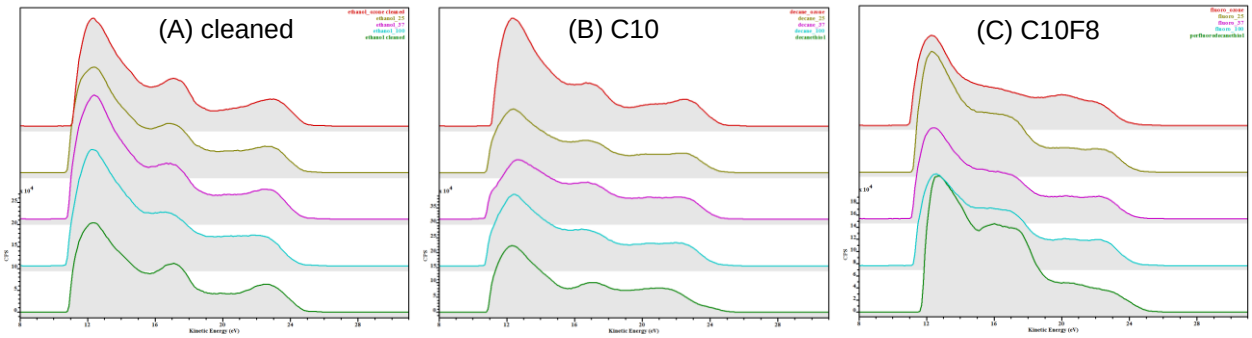

Figure 23. UPS spectra for the various silhouette patterned ZnO samples. (A) ZnO samples where no thiol modification was performed, but the three different sized nylon patterns were used during UV/ozone cleaning. (B) C10-modified ZnO. (C) C10F8-modified ZnO.

The presence of a pattern was not confirmed for these samples. XPS imaging only has a lateral resolution of 15microns, at best, but it takes a significant chemical difference between patterned and unpatterned regions to identify a chemical contrast. Since it is clear that the nylon deposits a material on the surface, it is likely that any possible chemical contrast would be diminished. NEXAFS imaging was not attempted. Based upon the UPS spectra, which is very surface sensitive, where little variation observed between 25, 37, and 100 micron mesh screens, it is speculated that there was no pattern retained by the masking process.

3.2.3. Other Patterning Strategies

Microcontact printing was attempted as another feasible strategy for patterning thiols on gold and ZnO.[46-55] This technique has been extensively explored in the literature, although backfilling with secondary thiols has not been as thoroughly examined. Microcontact printing does have the distinct advantage of deposting SAMs directly and does not require any destructive treatments. Unfortunately, the consistency of results obtained from microcontact printing often relies on the experimenter. Additionally, microcontact printing often only forms uniform patterns over very limited domains which could be difficult to unambiguously pinpoint in photoemission analyses. Microcontact printing was attempted using a poly(dimethyl siloxane) (PDMS) stamp from a photoresist master, shown in Figure 24, where multiple features were present. These domains could not be reliably evaluated in XPS, since the domains were not visible to the eye and could not be clearly isolated for analysis. Large area stamps with a consistent pattern would be desirable. This strategy was therefore only of secondary importance to the above mentioned patterning methods.

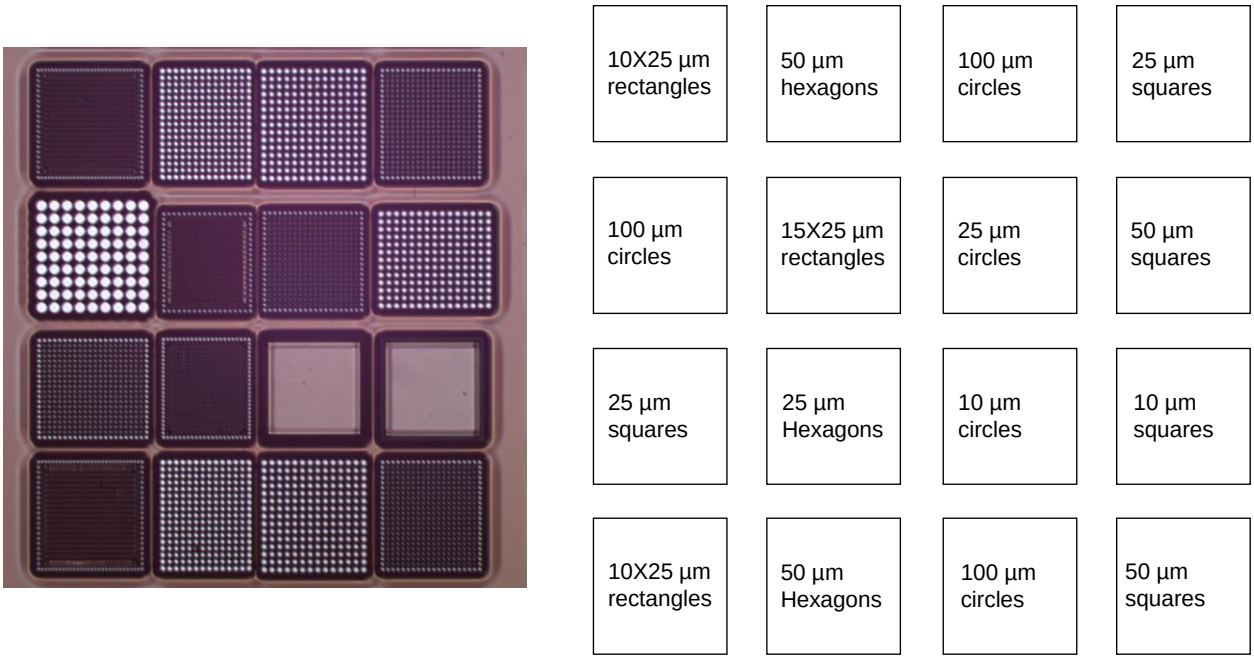

Figure 24. An optical image of the photoresist master with an array of 16 patterns is shown along with the description of each domain. PDMS can be used to form a reverse replica of the master for microcontact printing.

The ultimate goal of the patterning investigation was to explore the role of a heterogeneous substrate in a systematic manner. Consequently, an alternative strategy is to use a substrate, which is itself heterogeneous and modify all features of the substrate uniformly. An interdigitated electrode (IDE) is a substrate where independently addressable regions of the substrate are interdigitated giving an area for photoemission analysis where each region can be evaluated in a spatially averaged spectrum.

The use of an IDE array is a unique platform for photoemission investigations. No examples of the use of IDEs as a substrate for XPS analyses are known to the author. There are a limited number of circumstances where substrates, with characteristics similar to that of an IDE, have been used for XPS.[56-58] XPS studies on fuel cell materials have taken advantage of the ability to control the voltage on independent electrodes.[59, 60] Suzer and coworkers have made significant contributions on the use of applied biases in XPS and have termed "dynamic XPS" for the ability to apply an alternating bias to the sample in time with analytical characterization.[61-66] Differential charging of SAM layers has received some attention in the literature.[67-70]

The advantages of using an IDE as a substrate are numerous. The width and length of the electrodes can be controlled. The spacing between electrodes can also be controlled. Electrodes can be modified uniformly, or one set of electrodes could be modified independently from the other. In the absence of an overlying film, the voltage can be controlled on each pair of electrodes independently. An overlying film can be deposited to allow for some electrochemical communication between the IDE electrodes, thus allowing for some evaluation of charge transport and charge injection of the overlying film. This strategy allows for the control of

differentially charged regions of the substrate in known geometries, whereas the previous attempts at patterning only allowed for characterization of *ex situ* prepared samples. Figure 25 shows the general schematic of an interdigitated electrode where the analysis area covers multiple "fingers" from each of the electrodes. In XPS, the resulting spectrum gives a set of peaks corresponding to the electrodes which are electrically grounded. The electrically isolated electrodes give a set of peaks at a higher binding energy corresponding to the field produced between the electrodes by the photoemission process.

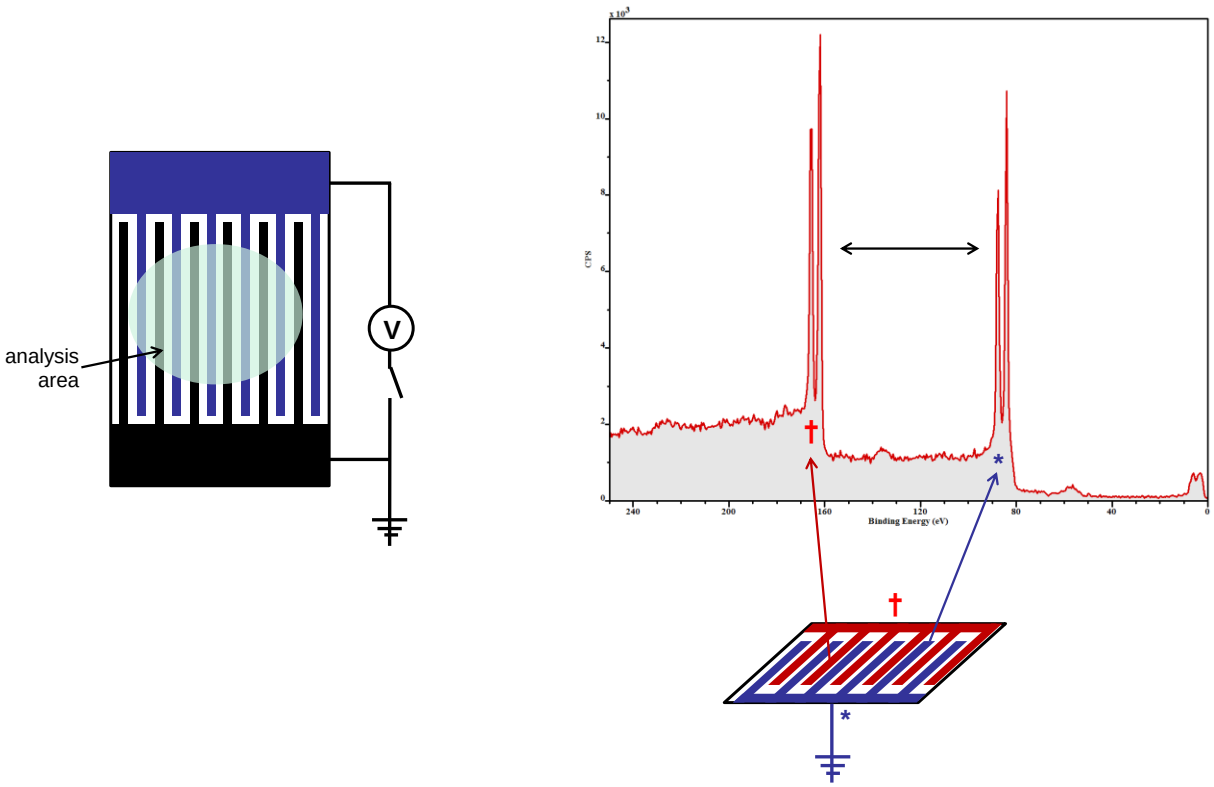

Figure 25. An interdigitated electrode (IDE) is shown as a substrate for use in photoemission analyses. The region under analysis is large enough to cover electrodes from both pairs of electrodes as well as the interdigit spacing. The interdigit spacing is equal to the width of the electrodes. Gold is deposited as the electrode fingers on a quartz substrate. The voltage on the electrodes can be controlled. In the simplest case, one set of electrodes is grounded to the spectrometer while the other set of electrodes is left electrically floating. As shown on the right, Au 4f emission at ~84 eV (BE) is due to emission from the grounded gold electrodes, while the highly shifted Au 4f emission is due to charging of the electrically floating gold electrodes. The shift of the floating electrodes gives an indication of the nature of the surface and/or the electronic communication with the grounded electrodes.

4. CONDUCTING POLYMER INTERFACES

4.1. Varying Thickness Conducting Polymer Films

A number of polymers and substrates were investigated to evaluate the role of the conducting polymer on the electronic band structure at the polymer/inorganic interface. Polymers analyzed included poly(3-hexylthiophene) (P3HT), poly(ethylene dioxythiophene) (PEDOT), poly(aniline) (PANI), and poly(thiophene). Electrode materials evaluated included gold, ZnO, and indium-tin-oxide (ITO). The typical strategy for investigating the electronic band structure is to increase the organic layer thickness as shown in Figure 26, while performing photoemission characterization with its narrow depth of analysis.[7, 8, 71] This allows for evaluation of spectral energy shifts versus distance from the interface. XPS results for electrochemically deposited poly(thiophene) and poly(aniline) are shown in Figure 27 for three different thicknesses of the respective polymers.

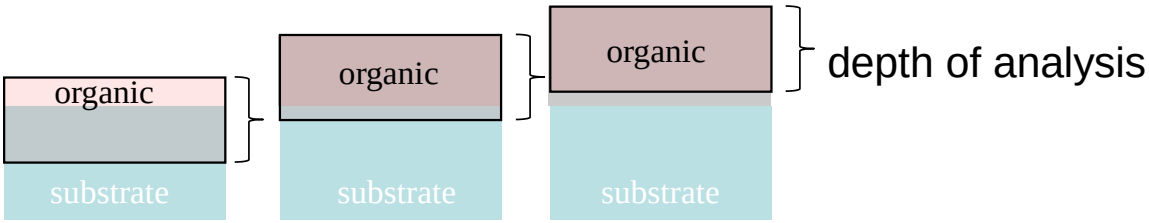

Figure 26. The most common method for analyses of the energy level alignment at an interface is through sequential deposition of the topmost material with corresponding photoemission characterization at each stage. This gives characterization to various depths across the interface. For evaluation of polymer films on an inorganic substrate, the polymers must be deposited *ex situ* on multiple samples to give a range of thicknesses.

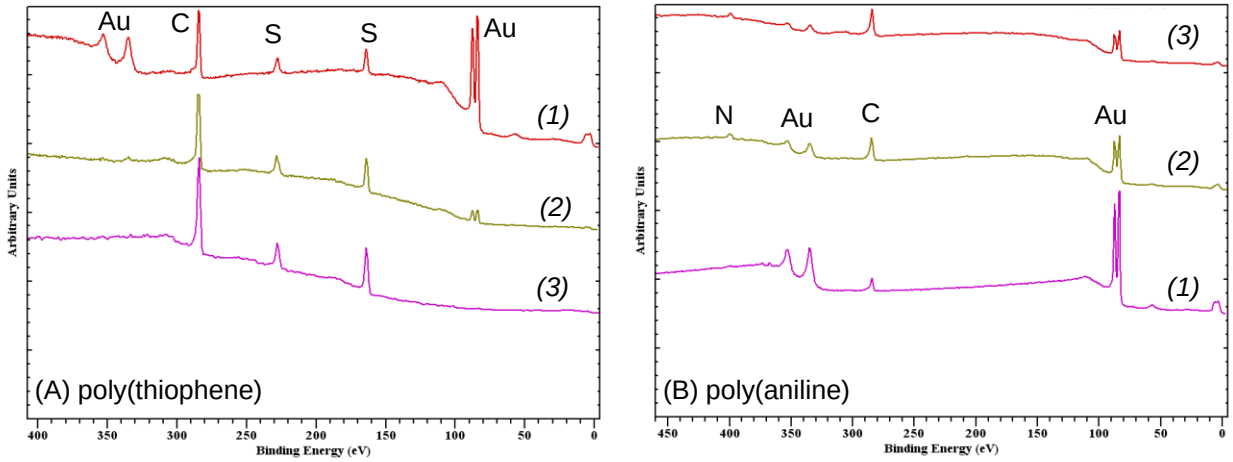

Figure 27. XPS spectra are shown for electrochemically deposited (A) poly(thiophene) and (B) poly(aniline) on gold at three different thicknesses from (1) thinnest to (3) thickest.

Survey spectra show the attenuation of the gold signal with growing polymer thickness, as well as the increase in intensity for the polymer constituents, C and S for poly(thiophene) and C and N for poly(aniline). High resolution spectra revealed little shifting of spectral components with polymer thickness indicating no significant charge redistribution in the polymer.

A novel conducting polymer with photoabsorbing properties, poly(tris(4-(thiophen-2-yl)phenyl)amine) (N3), was similarly electrodeposited on ITO at varying thicknesses.[19] Survey spectra for the deposited N3 films are shown in Figure 28. The In and Sn signals from the ITO substrate are attenuated as the N3 polymer thickness increases. N, C, and S grow in intensity with thicker N3 films until the substrate signal is completely attenuated. Pd and Br were observed in the N3 polymer as residual contaminants from the synthesis of the monomer. Unfortunately, the presence of Pd in the polymer films may significantly affect the energy shifts of the polymer constituents; however, since N3 is a novel polymer and has not been previously studied, the analyses had to be performed with the contaminants present.

Figures 29 shows the high resolution spectra for the individual energy regions associated with the ITO substrate. No significant energy shifts were observed for In or Sn as the N3 polymer film was increased. The O 1s showed a change in overall peak shape as the polymer thickness grew probably from entrained impurities or electrolyte in the polymer film.

The species corresponding to the N3 polymer (C, N, and S) increase in intensity as the polymer is grown on the ITO substrate. The signals remain relatively sharp until a thick polymer film was deposited and broadening of the peak shapes was observed due to charging. Almost no shift in the C 1s, N 1s, or S 2p peaks were observed as the polymer thickness was increased. Some variation in peak shape appeared at stage #4, but, due to the broadening of the spectra, it was likely do to charging for that specimen. As was observed for the poly(thiophene) and poly(aniline) samples, little can be discerned about the charge redistribution at the N3/ITO interface. The band alignment is dictated by the difference in work function between the substrate and polymer as investigated by UPS, Figure 31. The work function and percent compositions are summarized in Table 3.

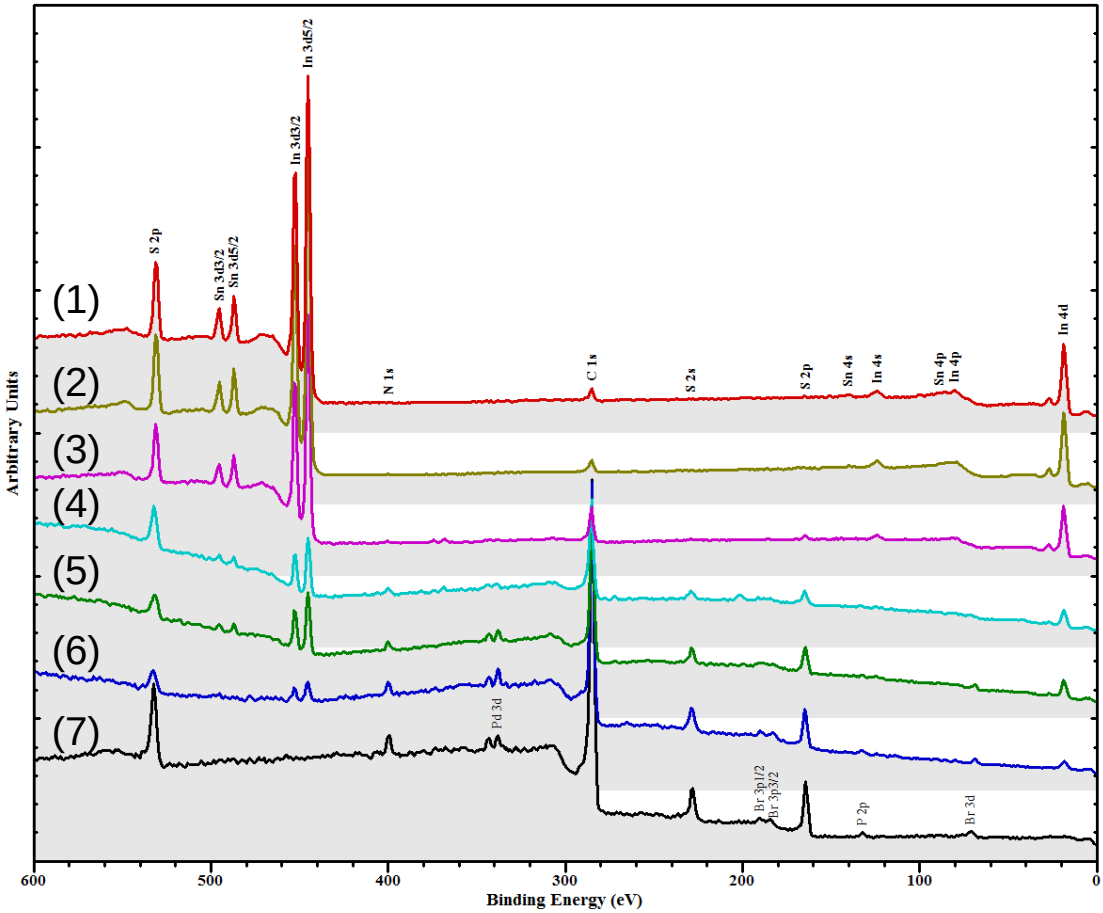

Figure 28. N3 polymer was electrochemically deposited on ITO. The increase in thickness is observed from sample 1-7 as the In and Sn signals become attenuated due to the overlying polymer. The components of the N3 polymer, namely C, N and S grow in intensity as the N3 polymer thickness increases. Impurities were observed in the N3 polymer.

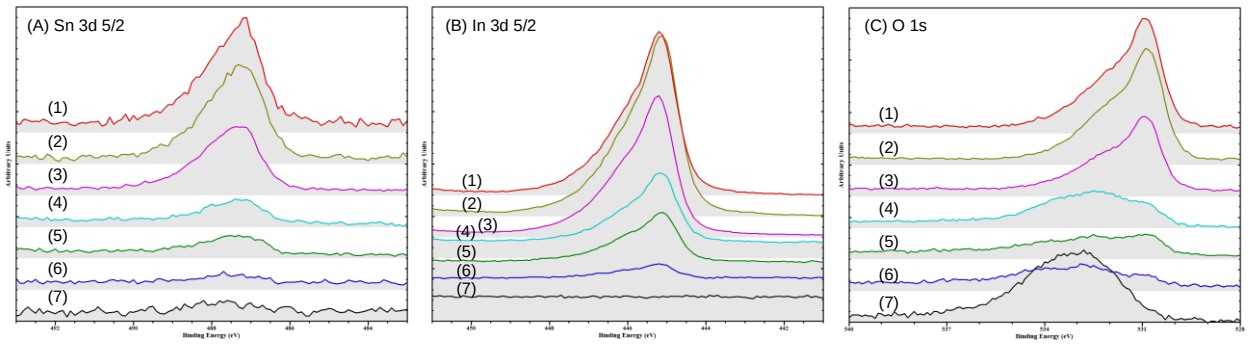

Figure 29. N3 polymer was electrochemically deposited on ITO. The increase in thickness is observed from sample 1-7 as the In and Sn signal became attenuated due to the overlying polymer. The O 1s from ITO is attenuated until a thick film of N3 was deposited and a broad O 1s peak was observed due to entrained contaminants and charging.

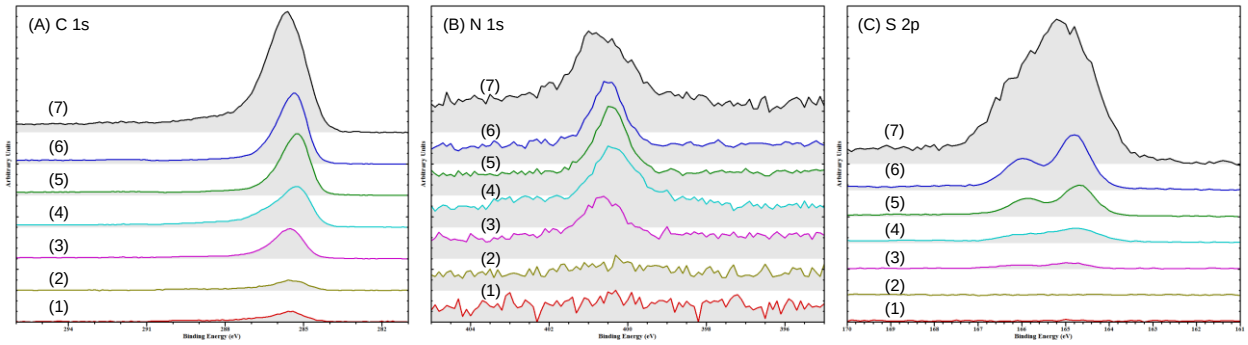

Figure 30. N3 polymer was electrochemically deposited on ITO. The increase in thickness is observed from sample 1-7 as the C, N, and S peaks grow in intensity. The thickest film shows a broadening of the C, N, and S peaks due to some differential charging of the polymer.

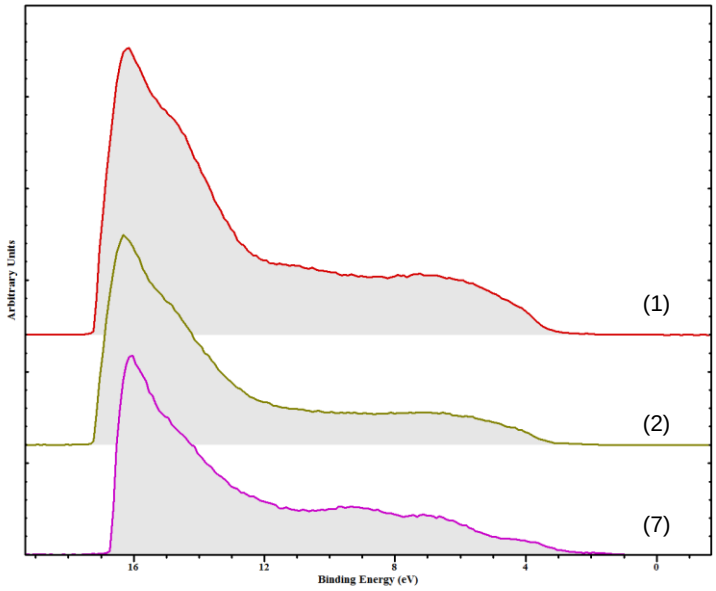

Figure 31. UPS spectra are shown for the N3 polymer electrochemically deposited on ITO at three thicknesses. Sample (7) corresponds to the thickest N3 film.

Table 3. Work function values and atomic concentrations for seven thicknesses of N3 polymer on ITO. Thicknesses of the polymer increase from 1-7 corresponding to the increase in C concentration.

	Atomic Concentration [%]				
	Carbon	Indium	Nitrogen	Sulfur	WF (eV)
1	36	64	0	0	3.7
2	38	62	0	0	3.7
3	64	32	1	3	
4	85	3	4	7	
5	86	2	3	9	
6	88	0	2	9	
7	90	0	2	9	4.3
gold					4.5

4.2. PEDOT on COOH-Modified ITO and Unmodified-ITO

The role of an interfacial layer on the charge redistribution of PEDOT at ITO surfaces was evaluated. COOH-modification of ITO was performed as discussed above. XPS spectra, Figure 32, show the increase in carbon for the COOH-modified ITO surface, relative to the unmodified sample, corresponding to the presence of the modifying SAM. PEDOT films were cast on modified and unmodified ITO samples with varying thicknesses increasing from sample 2-5. Figure 33 shows the high resolution spectra for carbon from the various thicknesses of PEDOT.

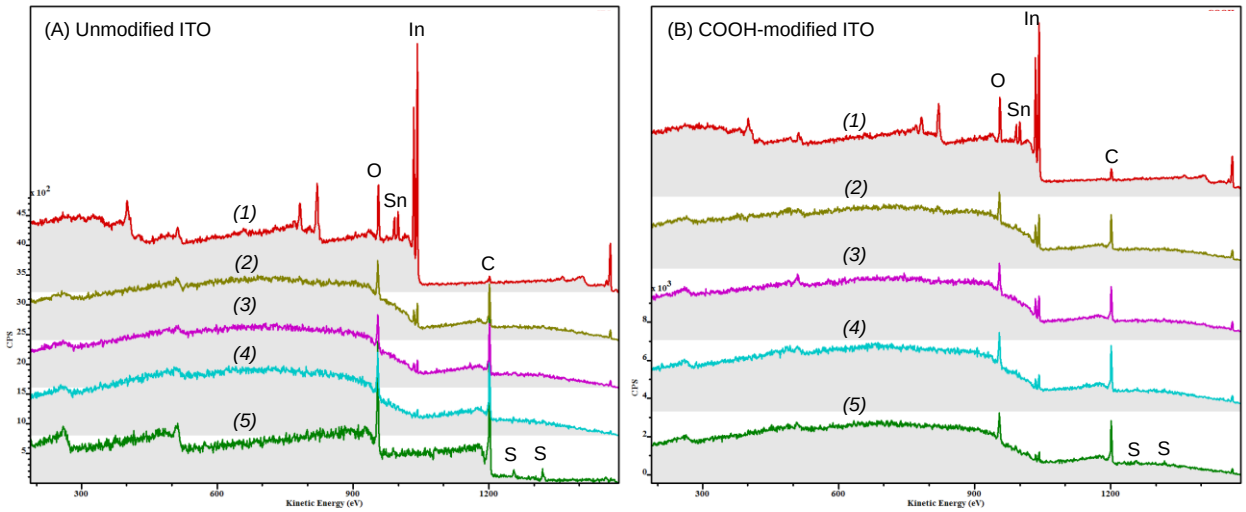

Figure 32. Survey XPS spectra are shown for PEDOT layers of varying thicknesses spin coated on (A) unmodified ITO and (B) 16-phosphonohexadecanoic (COOH) modified ITO. No PEDOT was present on (1) and thicknesses of PEDOT were increased from 2-5.

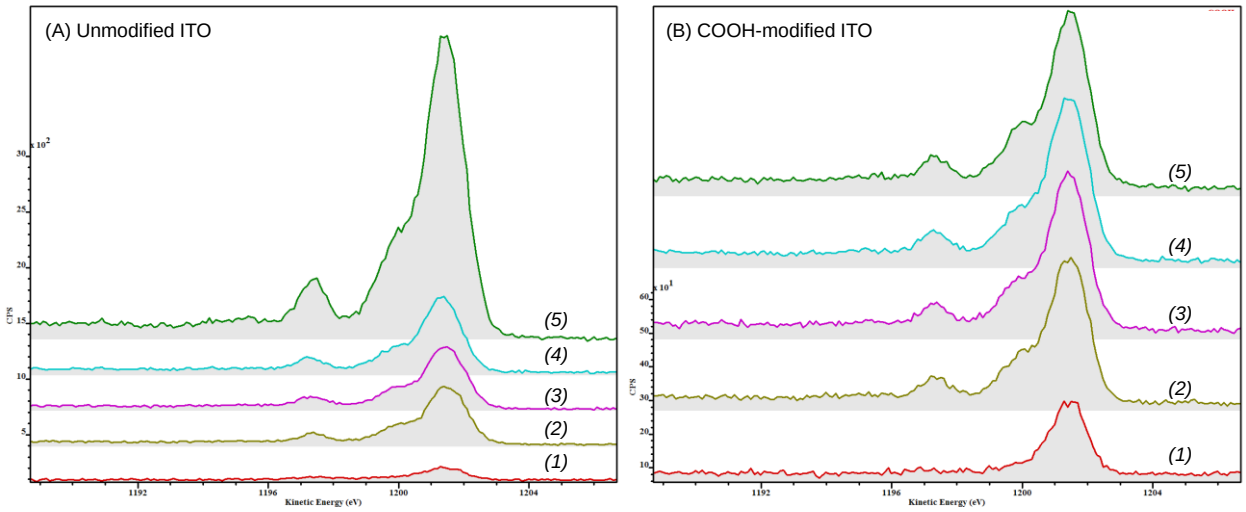

Figure 33. XPS spectra of C 1s are shown for PEDOT layers of varying thicknesses spin coated on (A) unmodified ITO and (B) 16-phosphonohexadecanoic (COOH) modified ITO. No PEDOT was present on (1) and thicknesses of PEDOT were increased from 2-5.

The COOH SAM layer was observed on the COOH-modified substrate indicated by the intense C-C component. The carbon spectra are the same for all thicknesses of PEDOT on both substrates, with only variations in absolute intensity. No shifts in peak positions were observed. Figure 34 shows the UPS spectra for the sequential depositions of PEDOT on the two ITO substrates. The COOH-modified substrates show a shift of the low KE edge from that of the unmodified substrates. However, there was almost no shift in the low KE edge with increased PEDOT layer thickness. Figure 35 summarizes the work function values for the two sets of samples as a function of layer thickness, i.e. percent composition of substrate (In) and overlayer (S).

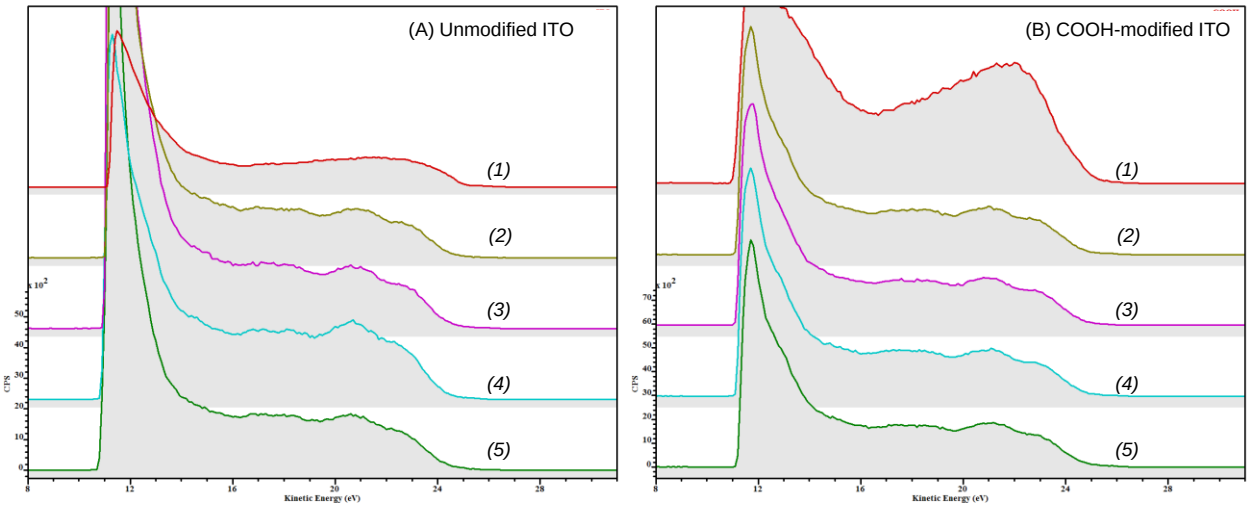

Figure 34. UPS spectra for PEDOT layers of varying thicknesses spin coated on (A) unmodified ITO and (B) 16-phosphonohexadecanoic (COOH) modified ITO. No PEDOT was present on (1) and thicknesses of PEDOT were increased from 2-5.

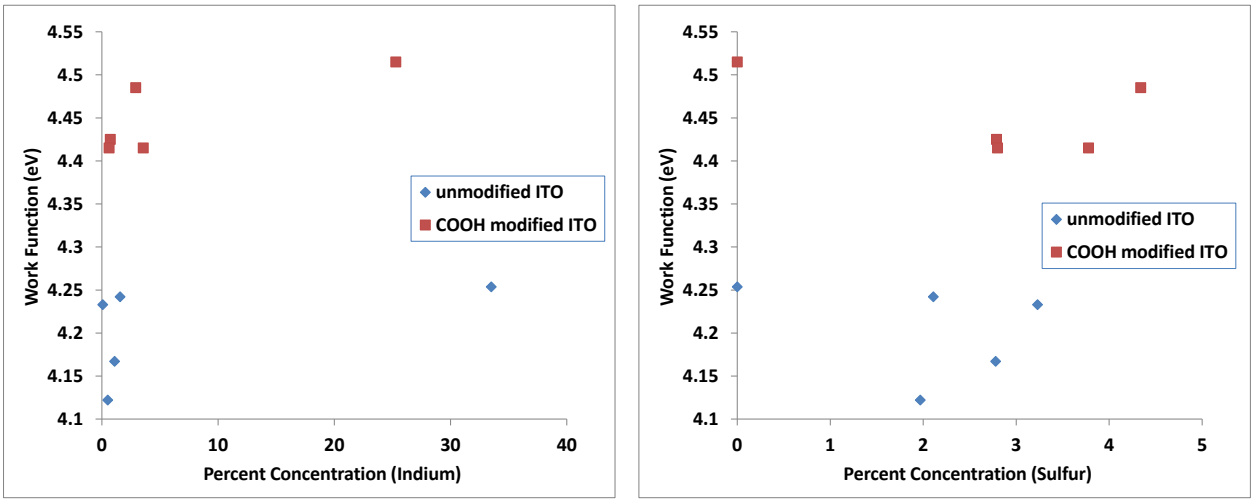

Figure 35. Work function does not change significantly for the various thicknesses of PEDOT on the two ITO substrates. Work function is shown as a function of indium concentration, where decreasing In concentration related to increasing PEDOT thickness. Work function is also shown relative to sulfur concentration, where increasing sulfur relates to increasing PEDOT thickness.

There is an overall difference in work function between the COOH-modified samples and the unmodified ITO samples which is retained regardless of the thickness of the overlying PEDOT. These results show that the work function is pinned and that charge redistribution through the polymer does not occur to any measureable extent.

4.3. HAXPES of Protected ITO Interfaces with P3HT

The characterization of buried interfaces is difficult and often has to be performed by a post-processing method where the interface is exposed. Hard energy X-ray photoelectron spectroscopy (HAXPES) offers the ability to tune the X-ray energy and thereby change the depth of analysis. In this work, an inorganic/organic interface was evaluated, namely the poly(3-hexylthiophene) (P3HT) interface with indium tin oxide (ITO), with relevance to organic photovoltaic devices. P3HT/ITO buried interfaces were examined using three X-ray energies where the ITO was prepared under different pretreatment conditions. The P3HT film protected the ITO surface to adventitious adsorbents and allowed for sensitivity to the buried ITO surface. Robust peak fitting parameters were obtained to model the O 1s and In 3d lineshapes. The deconvolution of these lineshapes allowed for the clear identification of a surface layer on the ITO which is oxidized to a greater extent than the underlying ITO substrate. The surface oxide layer is electronically disconnected from the underlying ITO, composed of an indium oxide and an indium hydroxide layer. The peak fitting conditions also allowed for an estimation of the thickness of this insulating layer. The layer was determined to be approximately 2.2 nm for a pretreatment step where the ITO surface was etched using H_2SO_4.

The characterization of buried interfaces is of significant interest to the study of organic electronics yielding insights on the interfacial energy alignments between semiconducting materials, segregation of species at interfaces, and identification of interfacial contaminants.[7, 14,]

[72-76] Interfacial modifications and/or the presence of adventitious species have been shown to dramatically affect performance of organic electronic devices.[4, 5, 32] In organic photovoltaics (OPVs) and organic light emitting diodes (OLEDs) charge injection barriers can be present due to energy level offsets, and also due to the presence of undesirable chemical species at the interface. Interfacial modification has been shown to be beneficial to increase work function and charge transport across an interface. Similarly, work on interfacial oxides has led to increased performance in OPVs.[1, 38] Understanding and identifying surface constituents can help guide rational design of interfaces to improve the efficiency of organic electronic devices.

The nature of the interface in real devices is often unknown, since the interface is buried and cannot be strictly characterized. For many studies, characterization relies on separate analyses of the bare surface of the substrate and of the bulk organic film. Results from the two components are then combined to give a description of the interface and are assumed to remain unchanged. More rigorous strategies for evaluating interfaces are to do sequential analysis of varying thickness films under highly controlled conditions.[7, 10] For the case of conducting polymers on an inorganic substrate, the analysis is complicated by the difficulty of depositing polymer layers in the absence of adventitious contaminants. Additionally, polymer deposition introduces solvent interactions with substrate. Recently a polymer/oxide interface was thoroughly examined by use of multiple samples with varying thickness polymer films under the assumption that the substrate surfaces were the same for all samples.[74] Schlaf and coworkers have also performed *in situ* deposition of polymers via electrospray deposition to evaluate the interfacial energy alignment.[77] HAXPES is well suited to the study of a polymer/substrate interface since a single sample can be probed at varying depths.

In most circumstances where XPS has been used to characterize ITO, the surface has been exposed to atmosphere and a X-ray energy of 1486.6 eV has been used, although lower excitation energies and angle resolved measurements have been performed to obtain more surface sensitive measurements.[37, 75, 76, 78-81] Surface roughness, adsorption of adventitious species, and/or a measurement which is still too bulk-sensitive can confound these attempts to evaluate the ITO surface. Additionally, these studies have evaluated the bare ITO surface, without an actual interface with an organic material. Here, the presence of the organic film allowed for the tuning of the high energy X-rays to act as both a surface sensitive probe of the ITO substrate, as well as a bulk-sensitive probe.[28, 82-85] Three cases were examined where the ITO surface was pretreated to give varying surface chemistries. ITO surface chemistry is known to be affected by cleaning processes and can have dramatic impacts on device performance.[4, 5, 14] The depth discrimination accessed by HAXPES allowed for the observation a very thin, electronically disconnected surface region on the ITO surface. Robust peak fitting, confirming previous reports, has been shown to clearly delineate the various chemical environments.

Three excitation energies, 2.2keV, 3.1keV, and 3.9keV, were used for XPS characterization of the P3HT/ITO interfaces on the solvent cleaned ITO substrate, UV/ozone cleaned ITO substrate, and H_2SO_4 cleaned ITO substrate. The survey spectra, shown in Figure 36, show that the 2.2keV X-ray energy allowed for photoemission from the substrate, indicated by the In 3d peaks. The deeper analyses, using 3.1keV and 3.9keV sources, clearly show greater intensity from In 3d and O 1s photoemission from the ITO substrate. The similar attenuation of the In 3d across samples show that the polymer thicknesses were nearly identical. Tin is typically present in ITO at

atomic concentrations ranging between 6-18%. This was not enough to be observed in the limited volume of ITO evaluated.

High resolution spectra for C 1s and S 2s from the P3HT films on the three differently treated ITO substrates are not shown, but, other than changes in intensity and a slight broadening of the spectra with increasing X-ray energy, there were no changes in the C 1s or S 2s spectra as the depth of analysis was varied. The lineshapes were consistent and the BE positions did not vary. Since all three excitation energies probed the full depth of the P3HT films, it is not unexpected that no changes were observed. Shallower analyses may reveal differentiation of P3HT species within the P3HT films, however, for this study the surface of the ITO was of interest.

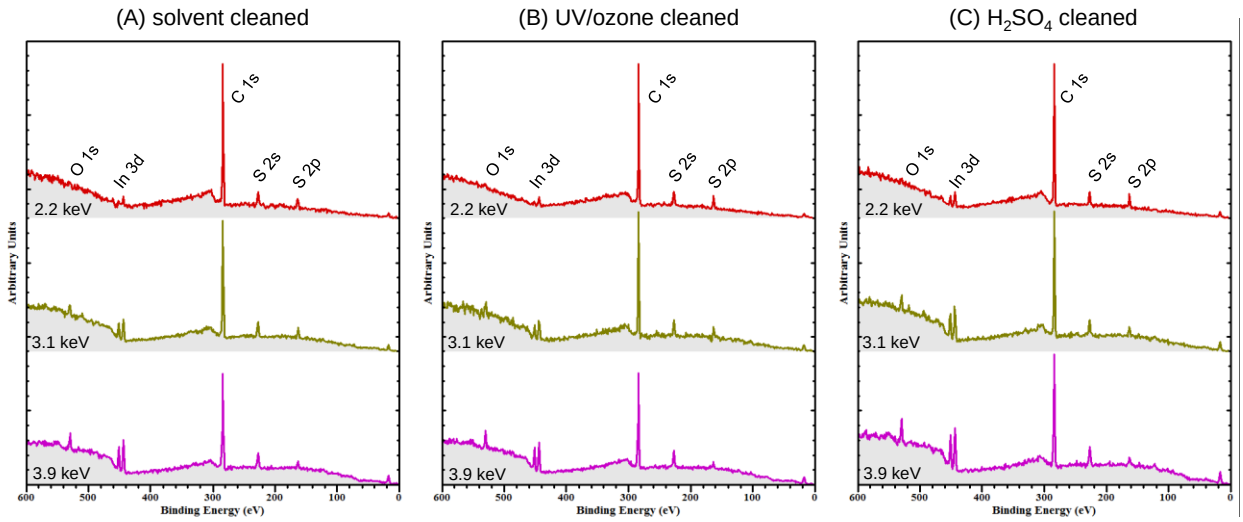

Figure 36. Survey spectra are shown for P3HT films on ITO surfaces using three different X-ray energies as indicated. Prior to P3HT deposition, ITO surfaces were treated with (A) solvent cleaning only, (B) solvent cleaning followed by UV/ozone treatment, and (C) H_2SO_4 etching.

The O 1s and In 3d showed significant and systematic changes as the analysis depth was increased, Figure 37 and 38. The O 1s of ITO has been of extensive interest in the literature and has tended to show the greatest variation in lineshape as a function of surface treatment.[4, 14, 44, 86, 87] ITO is conductive due to n-type doping with tin and oxygen vacancies.[88] Peak assignments have been made with associations to surface hydroxides, oxygen vacancies, and tin-oxide species. In the simplest case, a two component fit could be used to model all O 1s spectra, regardless of excitation energy or substrate pretreatment. However, the peak positions and FWHM had to be varied in each spectrum to obtain adequate fits. Using only two peaks for the O 1s fitting, the BE separation decreased by nearly 1 eV as the excitation energy was increased. Additionally, the FWHM of the high BE component was significantly greater for the high BE component of the UV/ozone cleaned ITO substrate. Two peaks could similarly be used to fit the In 3d $^5/_2$, but changes in the fitting parameters were also required for the various spectra. Since the peak FWHM and peak positions relate directly to the identification of surface and/or bulk constituents of the ITO, changes in these parameters lead to ambiguity in chemical identification. A more rigorous approach was followed to constrain the fitting parameters for both the O 1s and In 3d spectra.

Figure 37 shows the O 1s, with peak fits, from the three differently treated ITO surfaces buried under equivalent thicknesses of P3HT. Using a 2.2 keV source, the O 1s was low in intensity and showed two distinct components for all surface pretreatments. There was a relatively sharp component at around 530 eV with a broad second component approximately 2 eV higher in binding energy (BE). Since the In 3d intensity and O 1s intensities are very low, the O 1s evaluated at 2.2 keV is apparently only from the immediate surface of the ITO. Here, the two peaks used to fit the O 1s are associated with In_2O_3, for the low BE component, and $InO_X(OH)_Y$ (where X may vary from 0-1 and Y from 0-3), for the high BE component. The fitting parameters were constrained for these two components, Table 5, and were applied to all O 1s spectra. The highly constrained fitting parameters still allowed for adequate fits to all O 1s spectra taken at 2.2 keV.

When these two peaks were applied to the deeper analyses, a residual difference yielded a single asymmetric component with exactly the same FHWM and asymmetry across all spectra. Previous work has shown that an asymmetric lineshape adequately fit the O 1s of *in situ* prepared conductive indium oxide.[14] The asymmetric component was also successfully applied to ITO with some residual, unidentified surface species.[14] The fitting parameters of this previously observed asymmetric component matched the residual difference observed here for the O 1s from the deeper HAXPES spectra. These fitting parameters were used to synthesize Peak C in Figure 37, which is assigned to the bulk lattice of the ITO substrate. Peak C increased in intensity as the analysis depth increased. Peak C was also observed in the 2.2 keV analysis of the O 1s from the H_2SO_4 etched ITO sample.

The same strategy used to fit the O 1s was employed to fit the In 3d 5/2, Figure 38, where two constrained components were associated with In_2O_3 and $InO_X(OH)_Y$ and a third asymmetric component was assigned to the bulk ITO. In 3d electrons have a greater inelastic mean free path (IMFP) than O 1s electrons so a greater bulk contribution was observed in the In 3d 5/2 spectra relative to the O 1s spectra. Fitting parameters are also summarized in Table 5 for the In 3d 5/2 components. IMFP values are summarized in the supporting information.[89]

The asymmetry of peak C was held constant for the O 1s and In 3d with only a variation in FWHM. Additionally, the relative intensities of peak A and B for the In 3d were held constant and proportional to peak A and B used for the O 1s. The oxide and hydroxide peaks have not been previously confirmed; however, here it is clear that the peak areas, binding energy separations, and FWHM can be strictly identified from the extremely surface sensitive 2.2 keV analyses. These fitting parameters were constrained across all O 1s and In 3d 5/2 spectra leaving only the single asymmetric component, which was also constrained.

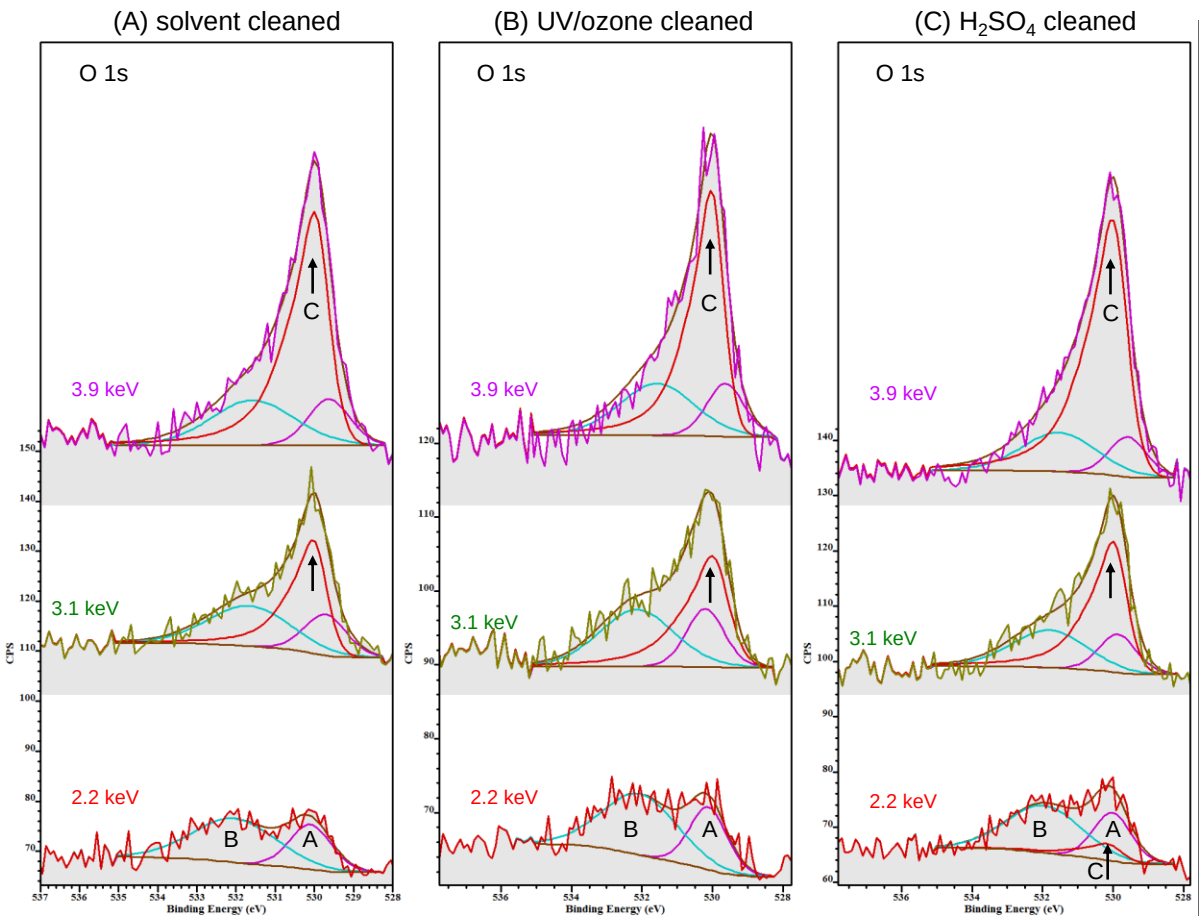

Figure 37. O 1s spectra are shown for ITO buried under P3HT films using three different X-ray energies. Prior to P3HT deposition, ITO surfaces were treated with (A) solvent cleaning only, (B) solvent cleaning followed by UV/ozone treatment, and (C) H_2SO_4 etching. Peak A and B were fixed at identical binding energy separations, FWHM, and area ratios across all spectra. This allowed for the clear identification of an asymmetric component, peak C, associated with the conducting ITO substrate in the deeper HAXPES analyses. Peak C was also observed in the 2.2 keV analysis of the H_2SO_4 treated ITO/P3HT sample.

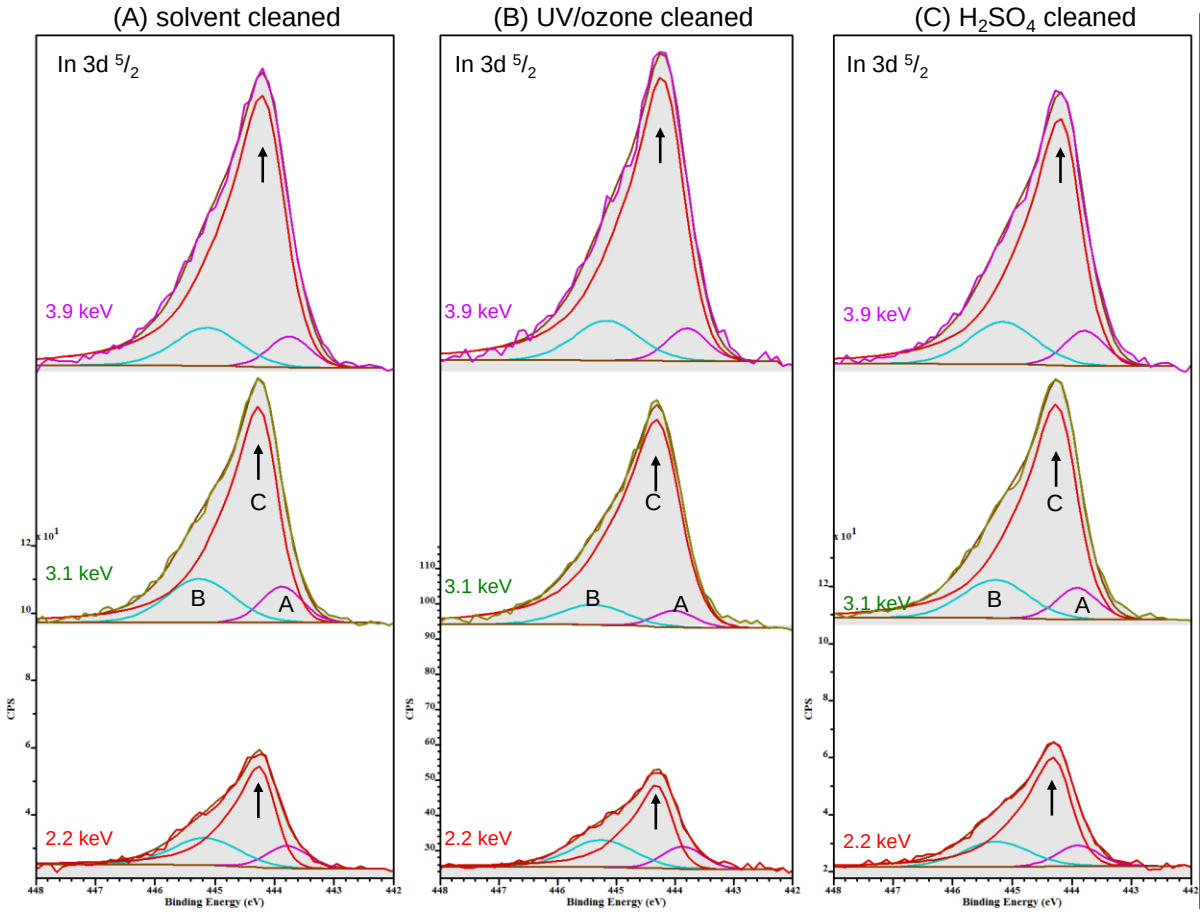

Figure 38. In 3d$^5/_2$ spectra are shown for ITO buried under P3HT films using three different X-ray energies. Prior to P3HT deposition, ITO surfaces were treated with (A) solvent cleaning only, (B) solvent cleaning followed by UV/ozone treatment, and (C) H_2SO_4 etching. Peak A and B were fixed at identical binding energy separations, FWHM, and area ratios across all spectra. An asymmetric component, peak C, associated with the conducting ITO substrate, was observed in all spectra but increased in intensity as the depth of analysis increased.

Table 4. Fitting parameters for the In 3d 5/2 and O 1s components. In 3d 5/2 peak B was fixed at FWHM=1.3, BE position A+1.375, and area=A*1.95. O 1s peak B was fixed at FWHM=2.5, BE position A+1.945, and area=A*1.95.

		In 3d 5/2 - peak A		In 3d 5/2 - peak C		O 1s - peak A		O 1s - peak C	
	hν (eV)	BE position (eV)	FWHM (eV)	BE position (eV)	FWHM (eV)	BE position (eV)	FWHM (eV)	BE position (eV)	FWHM (eV)
solvent cleaned	2200	443.78	0.80	444.27	0.65	530.10	1.25	N/A	N/A
	3100	443.88	0.80	444.27	0.78	529.71	1.25	530.04	0.80
	3900	443.75	0.80	444.22	0.90	529.63	1.25	530.01	0.87
UV/ozone cleaned	2200	443.87	0.80	444.32	0.64	530.12	1.25	N/A	N/A
	3100	443.87	0.80	444.31	0.77	530.20	1.25	530.01	1.07
	3900	443.79	0.80	444.23	0.90	529.63	1.25	530.04	0.82
H_2SO_4 cleaned	2200	443.90	0.80	444.33	0.74	530.01	1.25	530.17	0.99
	3100	443.91	0.80	444.27	0.84	529.86	1.25	530.00	0.92
	3900	443.78	0.80	444.21	0.85	529.58	1.25	530.02	0.97

The contribution of the bulk components of the O 1s and In 3d 5/2 increase nearly linearly with increasing depth of analysis, while the total peak areas of the surface constituents remain unchanged. As the analysis depth increased, the peaks became dominated by the bulk constituents and the O 1s and In 3d fits converged on similar FWHM and BE positions across the various surface pretreatments. For the deepest analysis, the In 3d 5/2 peak C binding energy position was 444.22 ± 0.01 with a FWHM of 0.88 ± 0.03 for all three samples. The O 1s peak C was 530.02 ± 0.02, FWHM of 0.89 ± 0.08. Peak A of the In 3d converged on 443.77 ± 0.02 and peak A of the O 1s converged on 529.61 ± 0.03.

The region of surface oxidation is of particular relevance for organic electronics, since it represents an insulating barrier between the bulk ITO and the overlying organic semiconductor. From the relative changes in peak areas, the thickness of the P3HT film was estimated along with the thickness of the surface oxidized layer of the ITO substrate. Figure 39A shows the change in analysis depth with the relative concentration of indium. Analysis depths were estimated by 3 times the IMFP for O 1s and In 3d electrons through a carbon overlayer at the respective excitation energies.[89] The plot shows a y-intercept where indium concentration is zero, thereby indicating the thickness of the P3HT films, 8.2 ± 0.9nm. Similarly, a plot can be made relating analysis depth to the relative contribution from the bulk oxide constituent of the O 1s giving a y-intercept relating to the depth of the interface between the oxidized ITO surface layer and the bulk oxide plus the thickness of the P3HT film, Figure 39B. The H_2SO_4-etched ITO sample was the only sample that gave three data points for the bulk constituent yielding a y-intercept of 10.5nm. This relates to a surface oxidized layer thickness of 2.3nm for the H_2SO_4-etched ITO sample. For the solvent cleaned and UV/ozone cleaned samples, the layer is presumably thicker since a bulk oxide constituent was not observed in the O 1s at 2.2keV. If the analyses for these two samples are presumed to penetrate the full depth of the surface oxidized layer, then a thickness of 3.6-3.8nm would be estimated. These calculations rely on a great number of assumptions including the correct values of the IMFP for O 1s and In 3d electrons through the P3HT film, uniformity and smoothness of the surfaces and interfaces, constant densities and relative atomic concentrations of oxygen in the surface oxidized layer and underlying bulk oxide, linear extrapolations, and accurate calculations of the atomic concentrations of In, Sn, O, and C (which can be affected by a great number of parameters).

Consequently, the thickness values given above are only rough estimates but do reliably demonstrate a difference between the oxidized layer thicknesses of the ITO etched by H_2SO_4 versus the other two cleaning procedures, illustrated in Figure 40.

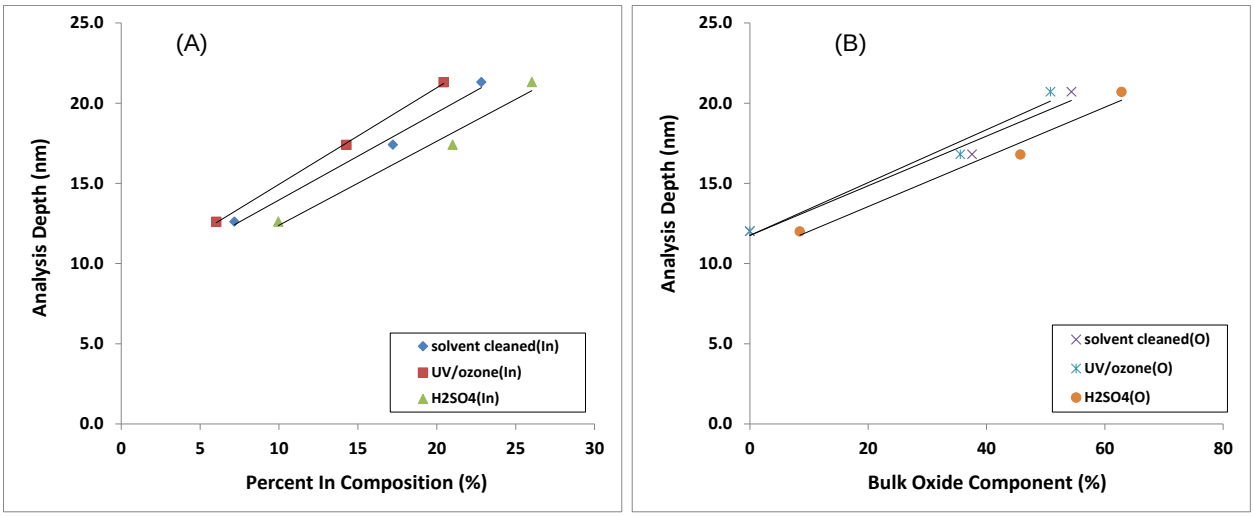

Figure 39. (A) The analysis depth, based upon 3x(IMFP) values for the respective X-ray energies, is plotted versus the atomic concentration of indium observed in survey spectra. A linear relationship was observed extrapolating to a y-intercept of zero indium content, i.e. the thickness of the P3HT film. (B) The analysis depth is plotted versus the relative content of the bulk oxide constituent from the O 1s peak fits. A bulk oxide constituent of zero shows that the only contribution to the O 1s spectra is from the oxidized surface layer. Consequently, the y-intercept relates to the depth of the interface between the bulk oxide and the surface oxidized layer, plus the thickness of the P3HT film.

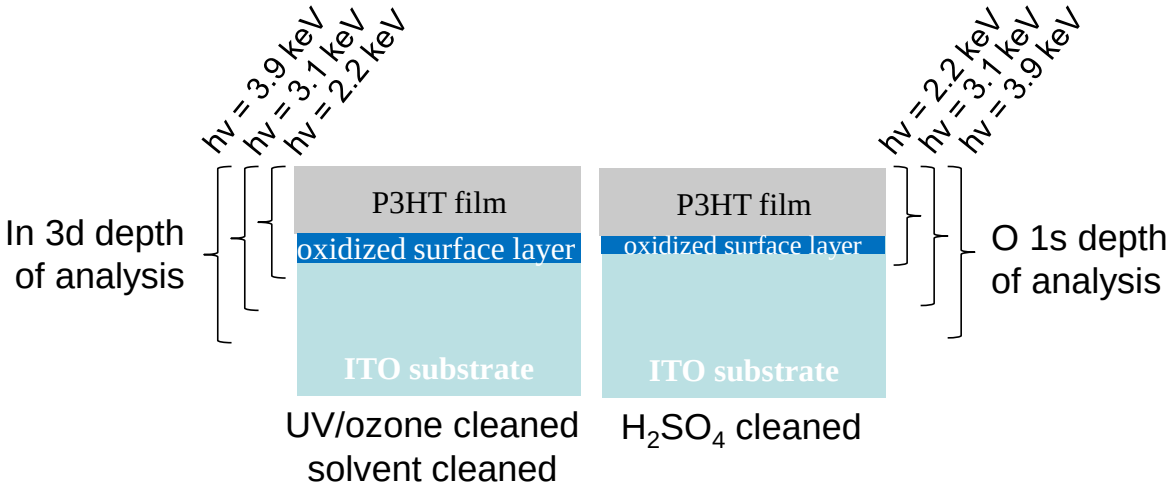

Figure 40. The analysis depth of XPS can be tuned in HAXPES by changing the energy of the illuminating X-ray. For the P3HT films investigated in this work, the films were sufficiently thin to allow for examination of the P3HT/ITO interface using three different X-ray energies. HAXPES

revealed a thicker surface oxidized layer in the ITO films cleaned solvent and UV/ozone treatments.

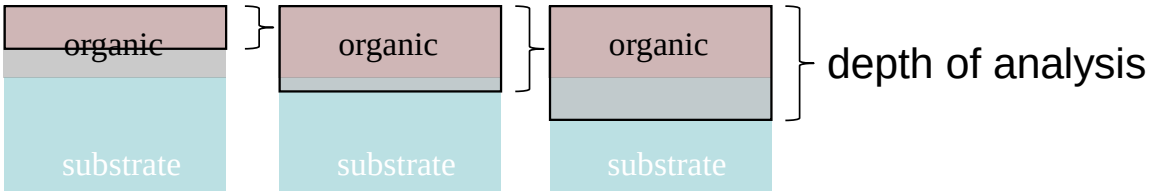

Figure 41. HAXPES allows for the use of different X-ray energies to probe various depths of the near surface region. Higher photon energy probes deeper into the sample. Consequently, an interface can be evaluated by simply changing the excitation energy to probe above, at, or below the interfacial region.

HAXPES was shown to be suitable for evaluating the buried interface between ITO and P3HT. The P3HT overlayer acted as a protective barrier to adsorption of adventitious contaminants such that the surface of ITO could be strictly analyzed as a function of surface pretreatment. Robust fitting parameters with clear chemical assignments were identified and could be applied to all samples. This allowed for identification of a surface oxidized layer, distinct from the underlying conductive bulk oxide. A clear discrimination of the surface components from the bulk component were observed. The bulk component exhibits an asymmetry due to the high conductivity in the bulk film, while the surface is fully oxidized and depleted of oxygen vacancies. The thickness of the surface oxidized layer was estimated, and, even after several days of exposure to air, the H_2SO_4-etched sample showed a thinner layer than the other two surface pretreatment conditions.

4.3. Photoelectronic Characterization of Discontinuous P3HT Films on ITO

The discussions above have evaluated the role of surface modification on photoemission analysis of various substrates as well as the interface between the substrate and the polymer. Here it was attempted to evaluate the role of direct patterning on the overlying conducting polymer. Additionally, differences in the P3HT films were investigated according to the deposition conditions used for the P3HT films.

P3HT is one of the most commonly used conducting polymers used in bulk heterojunction solar cells. P3HT has good light absorption properties, hole conduction, ease of processing, and phase separates to give continuous, but tortuous, interfaces with the electron transporting material in these devices. The performance of OPV devices utilizing P3HT have been shown to be extremely dependent on the deposition conditions and subsequent processing of the P3HT films.[90] P3HT films were spun coat on ITO under ambient lab atmosphere as well as under dry nitrogen. To evaluate the effect of patterning, a grid of scratches was produced directly into the P3HT films. Regions without patterning and patterned regions could be evaluated independently. Figure 43 shows the optical images of the cross-hatched patterns on the P3HT films. The width of the lines was tightly controlled by the use of a ball-on-disc tribometer to

make the scratches in the P3HT. The distance between lines was not as strictly controlled, but the orientation of the cross hatched pattern was perpendicular and gives a good comparison to unpatterned regions.

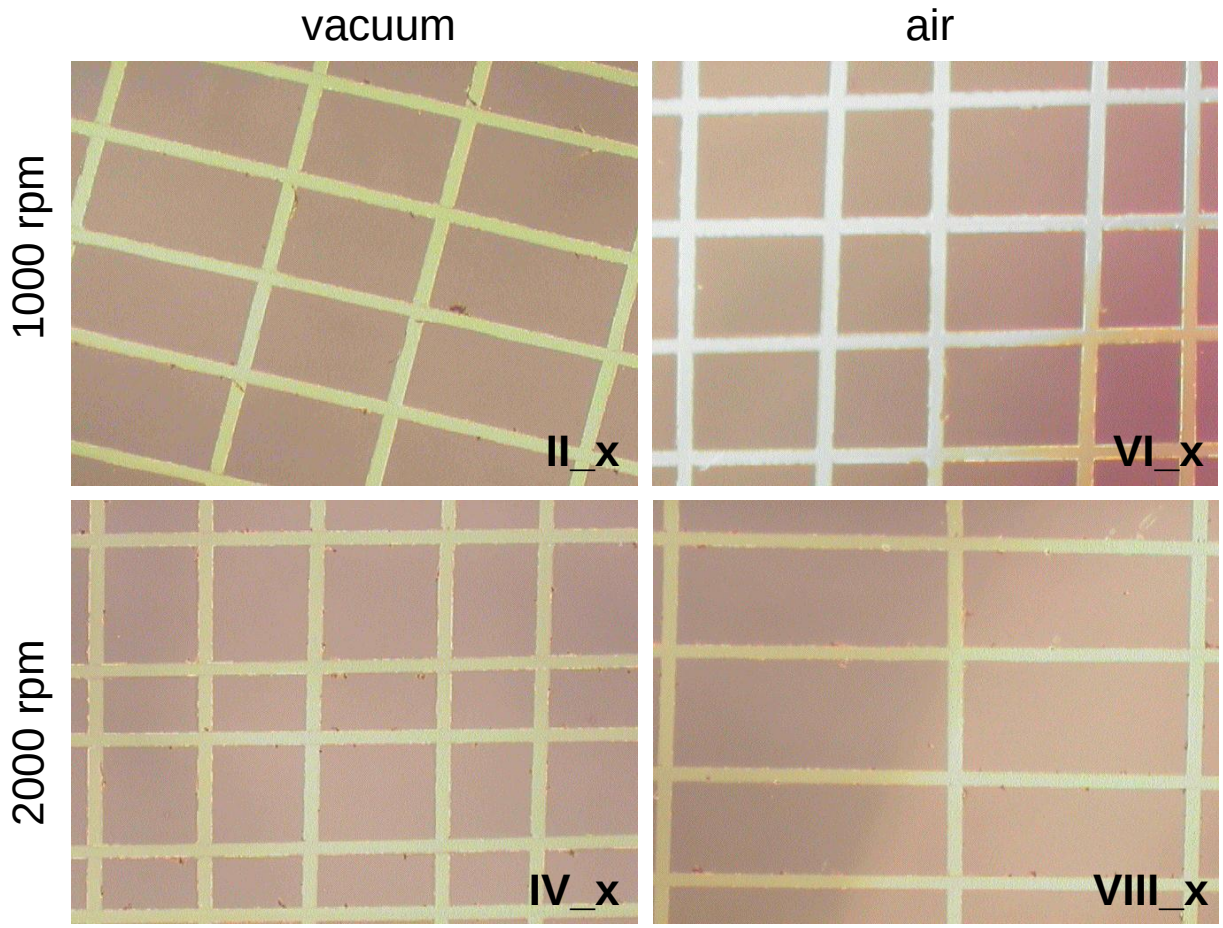

Figure 42. Optical images of cross-hatch patterns on P3HT films on ITO. Images are 480microns by 580microns. Samples II and VI were 20nm thick P3HT films, and samples IV and VIII were 10nm films. Samples II and IV were spin coated under under dry N_2. Samples VI and VIII were spin coated under ambient atmospheric conditions.

P3HT films were evaluated by XPS and UPS in patterned and unpatterned regions as shown in Figure 44. In the unpatterned regions on the samples spun coat under dry nitrogen, only the P3HT constituents were observed, C and S, with some oxygen from adventitious contaminants. In the two samples spun coat in air, there was a silicon impurity as well as a higher concentration of oxygen. The cross-hatched regions showed evidence of the ITO substrate along with the P3HT film. The lineshapes of the UPS spectra were not dramatically different between patterned and unpatterned regions, however, there was a significant difference between the P3HT films spun coat in air versus those spun coat under dry nitrogen. Table 4 summarizes the percent compositions observed via XPS and the work function values obtained from UPS for all four films in patterned and unpatterned regions.

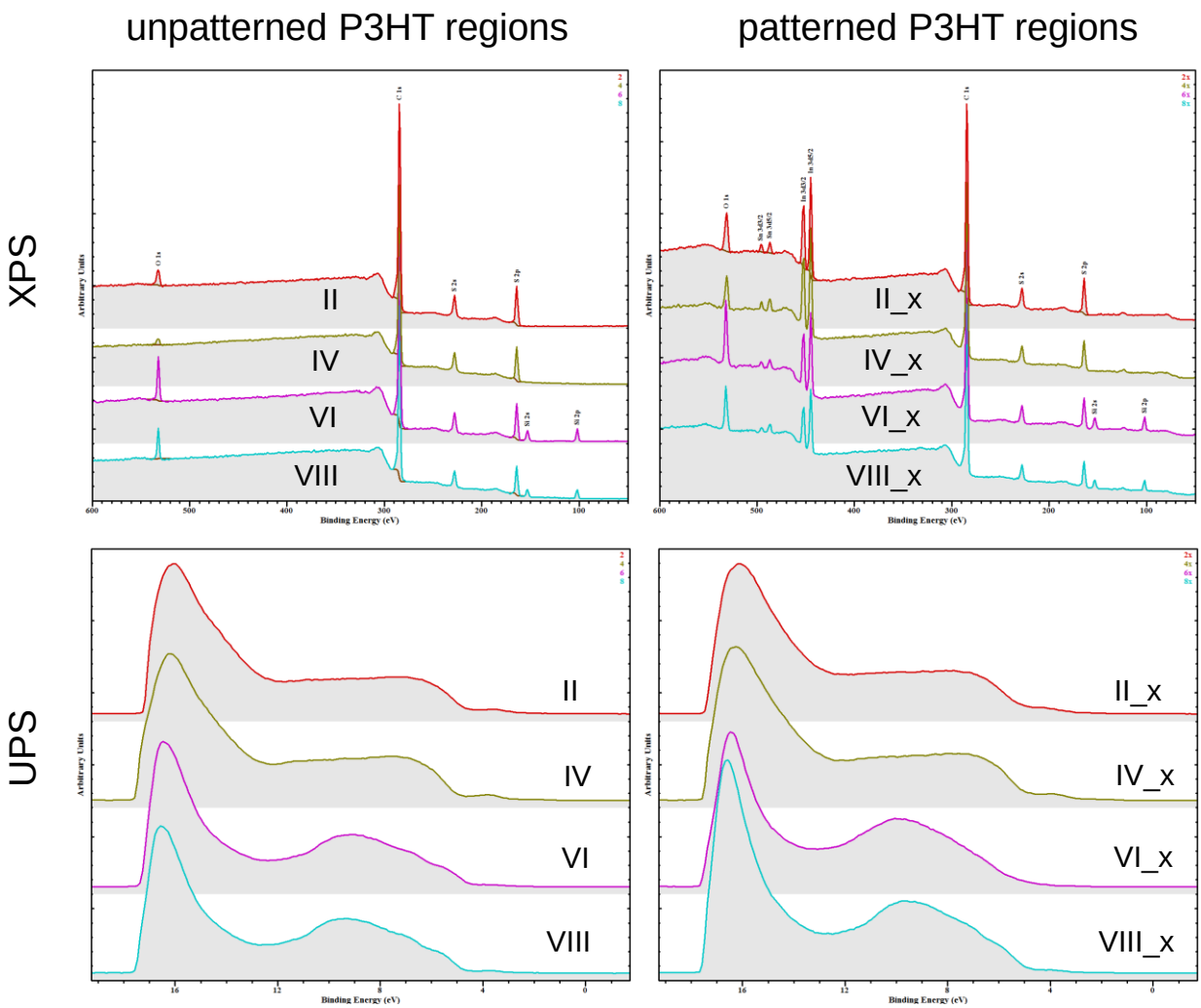

Figure 43. (Top) XPS spectra are shown for the P3HT films in (left) unpatterned regions and (right) patterned regions. The In and Sn from the substrate are observed through the patterned scratches in the XPS of the patterned P3HT films. (Bottom) UPS spectra are shown for the (left) unpatterned and (right) patterned P3HT films. Samples II and VI were 20nm thick P3HT films, and samples IV and VIII were 10nm films. Samples II and IV were spin coated under under dry N_2. Samples VI and VIII were spin coated under ambient atmospheric conditions. The "_x" nomenclature indicates the region on the film where lines were cross-hatched into the P3HT film exposing ITO.

Table 5. Work function values and atomic concentrations for the various P3HT films on ITO.

	P3HT thickness (nm)	Atmosphere during P3HT deposition	Area of P3HT film under analysis	Atomic Concentration [%]					WF (eV)
				Carbon	Oxygen	Sulfur	Indium	Tin	
II	20	Dry N_2	Continuous	87	3	10			3.7
IV	10	Dry N_2	Continuous	89	2	10			3.2
VI	20	Ambient	Continuous	86	6	8			3.7
VIII	10	Ambient	Continuous	87	5	8			3.4
II_x	20	Dry N_2	Discontinuous	81	8	8	3	0.3	3.5
IV_x	10	Dry N_2	Discontinuous	81	7	8	4	0.3	3.3
VI_x	20	Ambient	Discontinuous	80	11	7	2	0.3	3.3
VIII_x	10	Ambient	Discontinuous	82	9	7	2	0.3	3.4

There was very little change in work function observed between any of the patterned P3HT films. Work function values varied from 3.3-3.5eV with no obvious trend corresponding to the film deposition conditions or percent composition of exposed ITO. The work function of the unpatterned regions of the P3HT films correlated more closely to the thickness of the polymer. The 10nm films showed a low work function, 3.2-3.4eV, while the thicker P3HT films showed a higher work function, 3.7eV. The cross-hatching of the P3HT films, exposing ITO in the area of analysis, increased the apparent work function of the thin P3HT films and decreased the apparent work function of the thick P3HT films.

The P3HT films and underlying ITO provide a significant chemical contrast which can be observed via XPS imaging. Figures 45-48 show the XPS images for the patterned films. The spectrum corresponding to the respective intensity image is shown for each sample. The P3HT films were clearly observed in the open regions of the cross-hatched pattern. In the lines of the pattern the In, Sn, and O signals were observed from the ITO substrate. C and S were also observed in the lines of the cross-hatched pattern showing that there must still be a very thin P3HT film in the lines of the pattern. This result was consist for all four samples and even included the observation of the silicon peaks in the lines of the two samples spun coat in air.

NEXAFS imaging was also performed on all four samples. Images are shown for the two samples spun coat under dry nitrogen, Figure 49 and 50. The NEXAFS spectra for the P3HT coated areas were nearly identical for these two samples. The thinner P3HT sample also yielded a spectrum for the material in the lines of the pattern.

Imaging results confirm that the work function differences between patterned and unpatterned regions were influenced by the discontinuous nature of the P3HT films in the patterned regions. It is interesting that the large differences in WF between the two films deposited in air versus the two films deposited under nitrogen, converged to nearly the same WF in patterned regions. This result shows that any attempt to develop an energy level alignment from an imaging technique, where polymers of varying thicknesses could be patterned and imaged to give a sequence spectra from varying thicknesses, would likely encounter confounding interferences from the pattern itself.

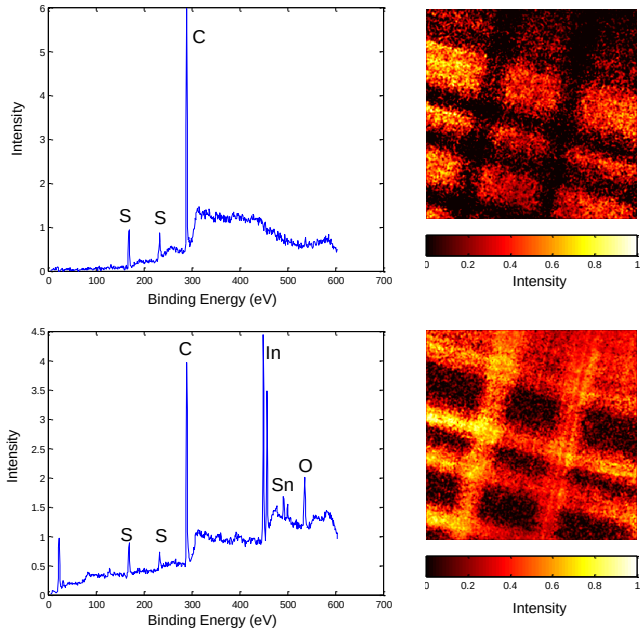

Figure 44. XPS images are shown for the two components showing the greatest contrast for the P3HT patterned film II (20nm thick P3HT spin coat under dry N_2). The P3HT layer, composed of C and S, is observed in between the lines where the ITO constituents are observed. The images are 400microns by 400 microns. Images correspond to the intensity of the spectra shown to the left of the image.

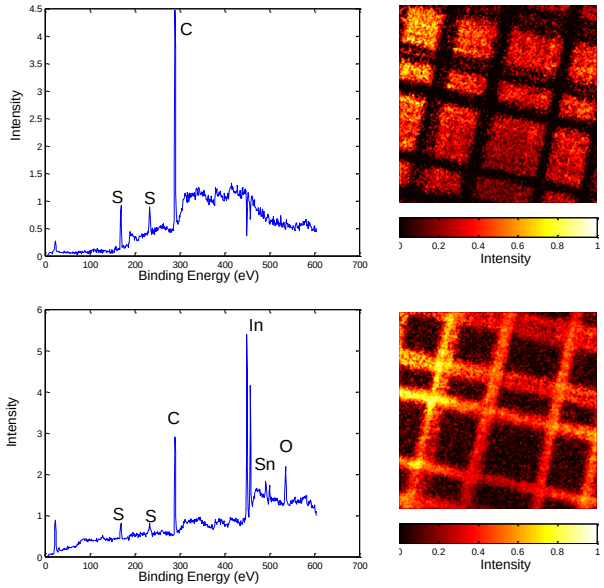

Figure 45. XPS images are shown for the two components showing the greatest contrast for the P3HT patterned film IV (10nm thick P3HT spin coat under dry N_2). The P3HT layer, composed of C and S, is observed in between the lines where the ITO constituents are observed. The images are 400microns by 400 microns. Images correspond to the intensity of the spectra shown to the left of the image.

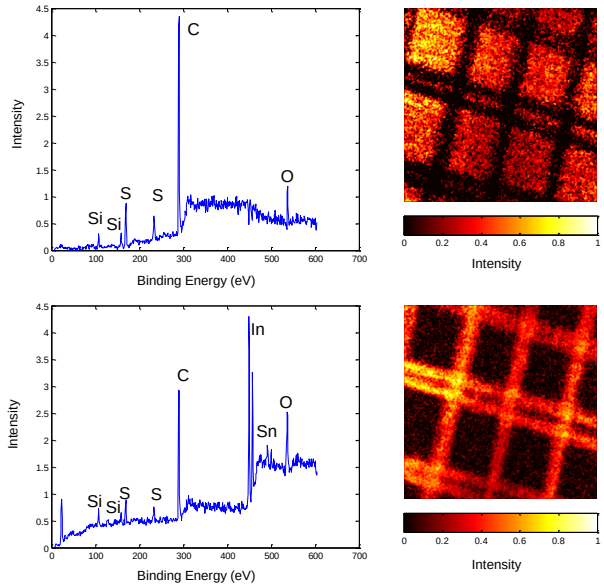

Figure 46. XPS images are shown for the two components showing the greatest contrast for the P3HT patterned film VI (20nm thick P3HT spin coat under ambient conditions). The P3HT layer, composed of C and S, is observed in between the lines where the ITO constituents are observed. The images are 400microns by 400 microns. Images correspond to the intensity of the spectra shown to the left of the image.

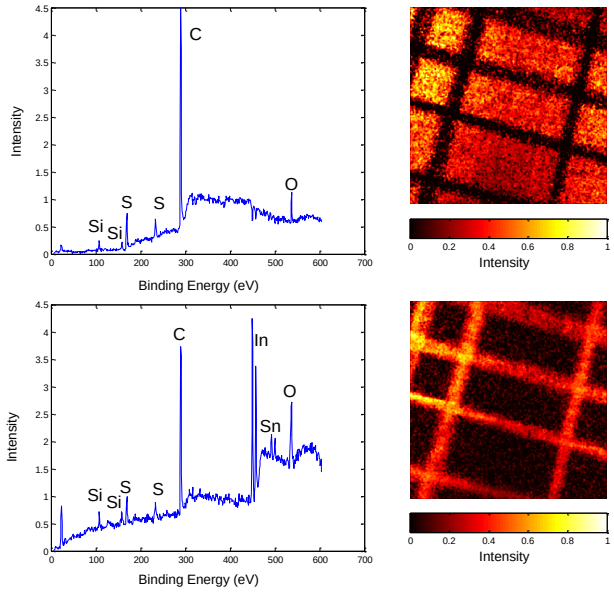

Figure 47. XPS images are shown for the two components showing the greatest contrast for the P3HT patterned film VIII (10nm thick P3HT spin coat under ambient conditions). The P3HT layer, composed of C and S, is observed in between the lines where the ITO constituents are observed. The images are 400microns by 400 microns. Images correspond to the intensity of the spectra shown to the left of the image.

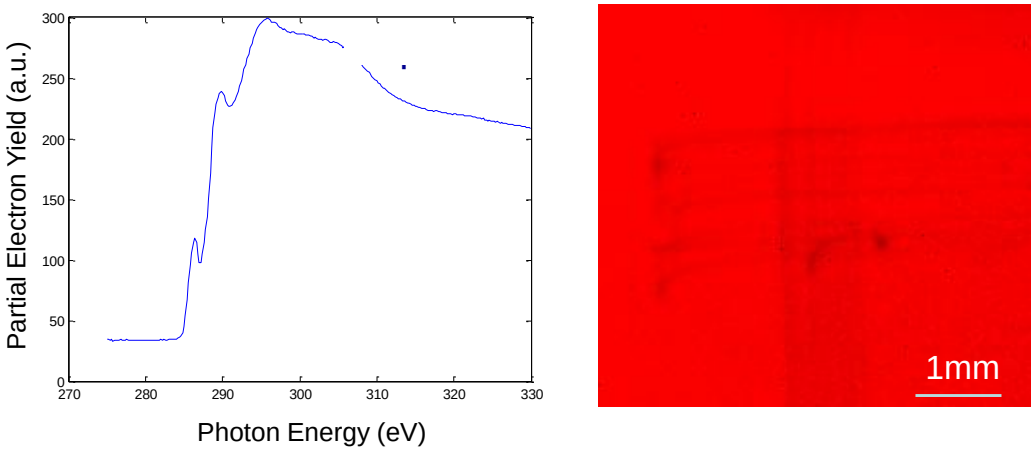

Figure 48. A NEXAFS image, and the corresponding spectrum, is shown for the P3HT patterned film II. Red coloration relates to the intensity of the given spectrum. The black lines indicate no data collected in those regions. A -100V bias was applied to the grid at the entrance to the partial electron yield detector.

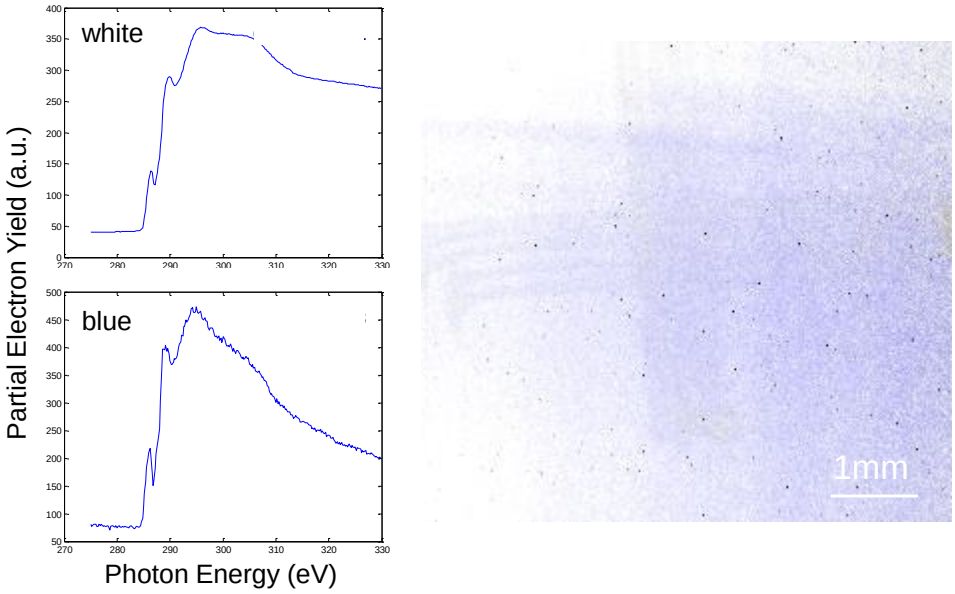

Figure 49. A NEXAFS image, and the corresponding spectra, is shown for the P3HT patterned film IV. White and blue coloration relates to the intensity of the indicated spectra. A -100V bias was applied to the grid at the entrance to the partial electron yield detector.

5. INTERDIGITATED ELECTRODES

5.1. PEDOT on Gold IDE

PEDOT is highly conducting, cheap, water soluble, easily processable, and electronic properties can be tuned through deposition procedures, annealing conditions, and/or introduction of various cationic species.[4, 39, 86, 91-93] PEDOT is often used to cover the roughness of an inorganic substrate to give a smooth, amorphous layer for interfacing with additional organic layers. PEDOT has also become of interest as a transparent conducting electrode to replace more expensive inorganic oxides.[94-99] Consequently, PEDOT can be used to tether conducting regions of a substrate thereby circumventing less-conducting regions.

As mentioned previously, an interdigitated electrode (IDE) was conceived as an ideal substrate for evaluating electronic materials via XPS, since one set of electrodes could be electrically grounded while the other set could be electronically floating. The floating electrodes represent insulating regions of the substrate, similarly to poorly conducting regions of a substrate used in OLED or OPV devices. The electrically floating electrodes of an IDE substrate will charge in the presence of an electric field. Since both the grounded and floating pairs of electrodes are gold, then shifted gold peaks in an XPS spectrum can be clearly identified from the insulating regions of the IDE substrate. The area of the charged gold peaks and the shift of the peaks relate to the total electric field produced by the emission of electrons from the sample during X-ray illumination.

Gold IDEs were evaluated via XPS with and without SAM-modifications. Figure 51 shows the gold IDEs with 50 and 70 micron interdigit spacings for the unmodified gold electrodes. Figure 52 and 53 show the spectra for C10 and C10F8 modified electrodes, respectively. Also shown are spectra for thin layers of PEDOT cast across the respective IDE substrates. In all cases there was still a significant gold signal observed indicating that the PEDOT films were exceptionally thin, less than three times the escape depth of Au 4f electrons through a carbonaceous overlayer (<10nm). For all cases where PEDOT was deposited, there were no shifted peaks observed in the XPS spectra indicating that the floating gold IDE electrodes were electronically connected to the grounded IDE electrodes. Various thicknesses of PEDOT were attempted and it was observed that no thickness of PEDOT could be deposited to leave the floating electrodes isolated from the grounded components. Additionally, the presence of the various SAM layers did not influence the charging of the isolated gold electrodes in the presence of PEDOT.

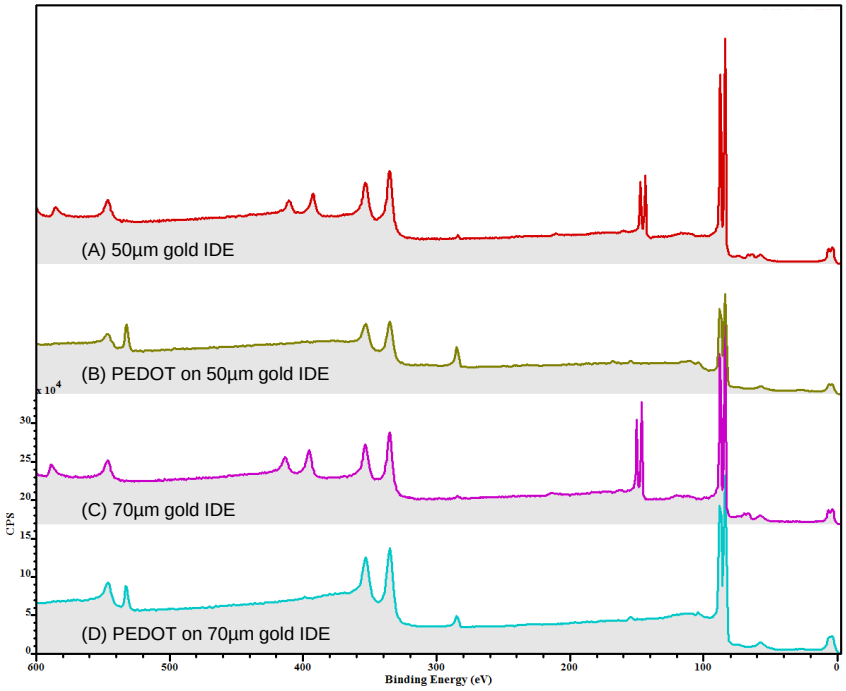

Figure 50. XPS spectra for unmodified gold IDEs with and without PEDOT overlayer using two different dimensions of interdigitated electrodes.

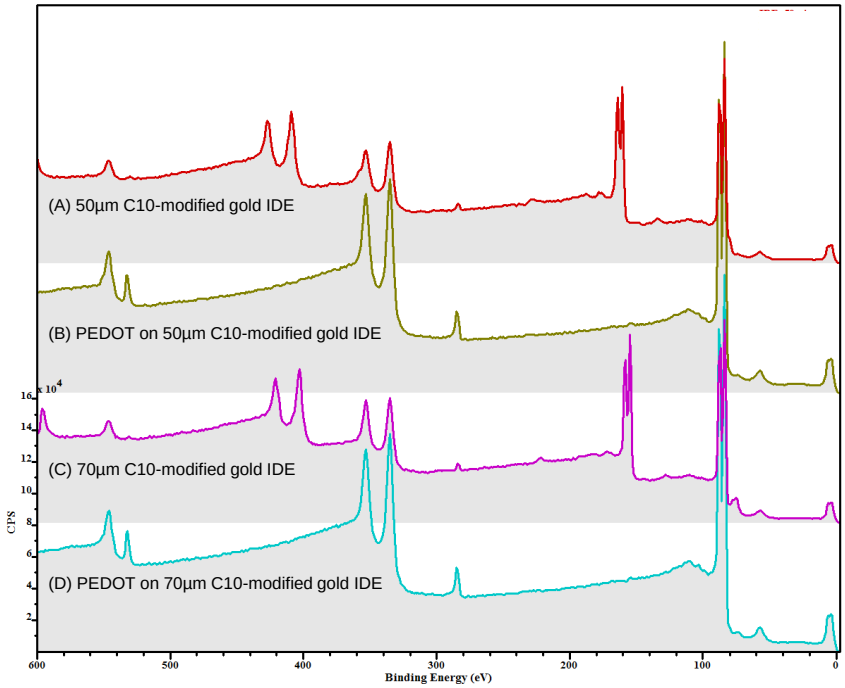

Figure 51. XPS spectra for C10-modified gold IDEs with and without PEDOT overlayer using two different dimensions of interdigitated electrodes.

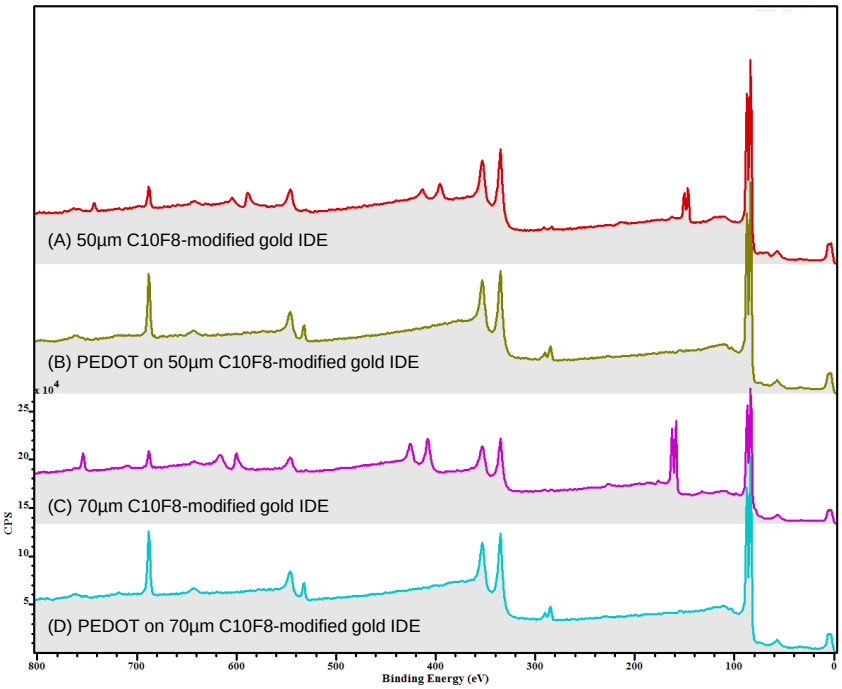

Figure 52. XPS spectra for C10F8-modified gold IDEs with and without PEDOT overlayer using two different dimensions of interdigitated electrodes.

The results from the above studies on conducting polymer films showed that the conduction in the polymers was sufficient to effectively distribute charge into the organic semiconductor uniformly. For the case of conducting polymers, the interface was dominated by an interfacial dipole associate with the difference in work function between the substrate and the overlying polymer. For PEDOT over the variously treated IDE substrates, an extreme case is represented where regions of the substrate were electronically isolated, i.e. fully insulating. The PEDOT films, even as extremely thin films, effectively wired the two regions of the gold substrate together. This is shown schematically in Figure 54 where the Au 4f is observed at around 84 eV for the electrically grounded set of gold IDEs. A second set of Au 4f peaks was observed at ~165 eV due to the charging of the isolated gold IDEs. In the presence of the conducting polymer film, which was still thin enough to allow for significant Au 4f emission, there was only a set of Au 4f peaks observed at 84 eV as would be expected for an electronically grounded substrate.

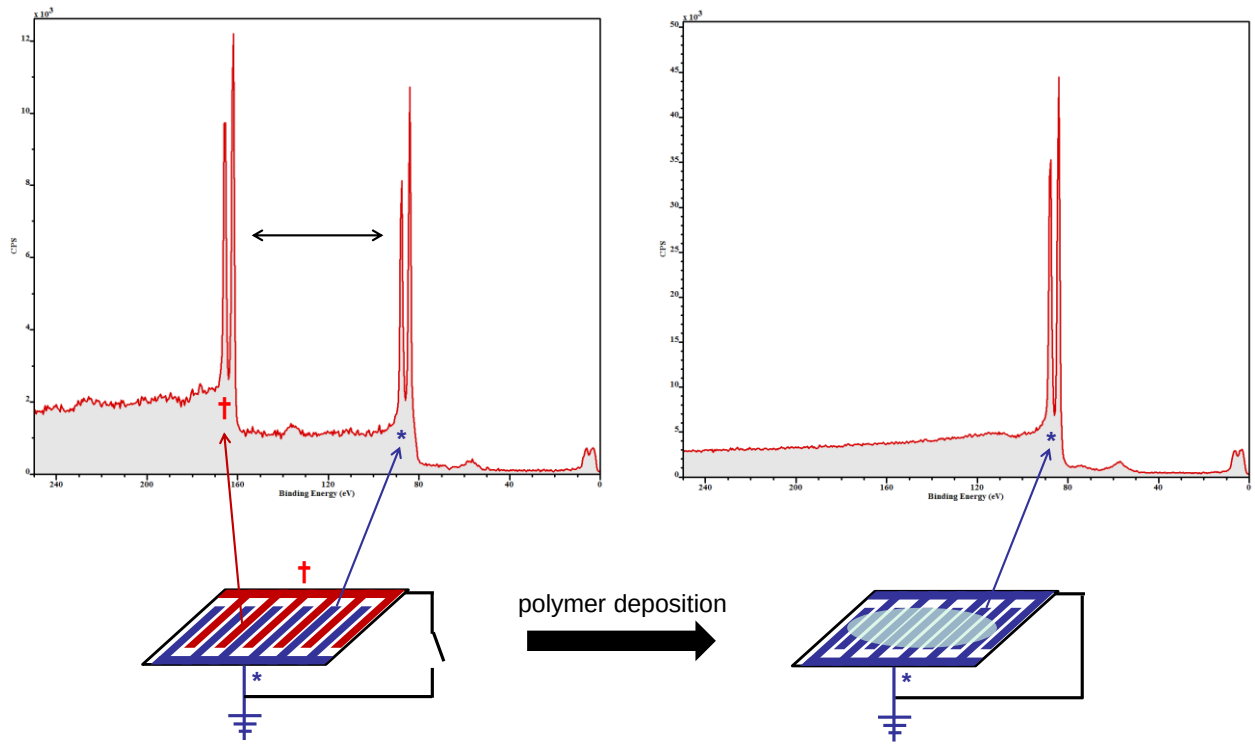

Figure 53. The schematic for the change in BE position of the Au 4f peaks is shown for the case of an IDE substrate used in XPS. In the case where there is no electronic communication between the grounded and floating pairs of IDE electrodes, there is a large shift in the BE of the emission from the floating gold due to static charging. When PEDOT is cast over the interdigit spacing, the ungrounded IDE electrodes are effectively wired through the PEDOT to the grounded electrodes. Consequently, the charging effect is removed and only one set of Au 4f peaks is observed.

5.2. TiOPc and C_{60} on Gold IDEs

Further studies on interdigitated electrodes were performed to investigate less conducting materials and the role of the electric field on charge transport and charge injection. C_{60} and titanyl phthalocyanine (TiOPc) films were deposited to expected thicknesses of 8nm on gold IDE substrates that had been cleaned via sputter etching. The samples were prepared entirely under vacuum conditions thereby preserving the cleanliness of the substrates and purity of the deposited films. Effects from adventitious species could be excluded. The resulting XPS spectra for sputter cleaned gold IDEs, and films of C60 and TiOPc over sputter cleaned gold IDEs are shown in Figure 55 for three different electrode spacings. The charging of the Au 4f for the sputter cleaned gold IDE was insensitive to the distance of the interdigit electrode spacing. However, in the presence of semiconducting organic thin films, the charging of the electrically isolated gold IDE electrodes was shifted greater for the larger interdigit spacings. The overall shift in the Au 4f for the charged gold substrate was significantly less in the presence of an overlying organic film. This was expected as the film should act to provide a pathway for electrons to partially neutralize the ungrounded gold electrodes.

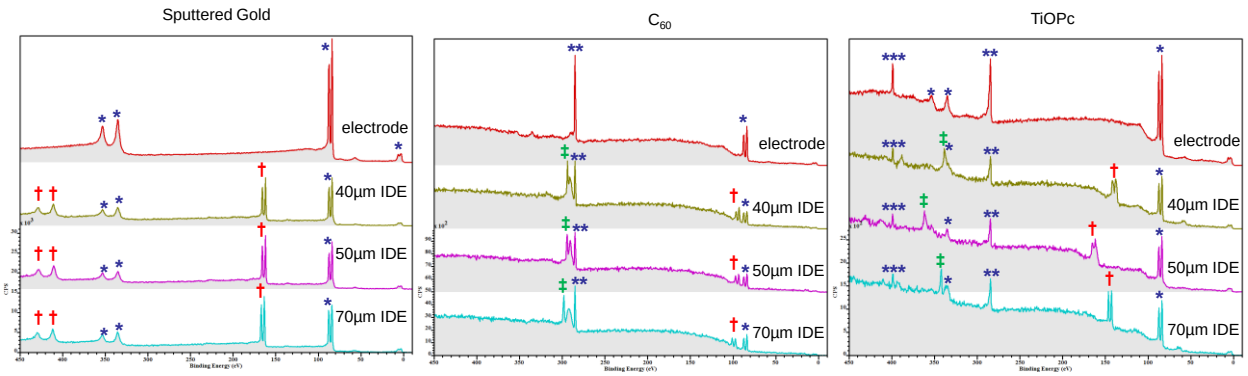

Figure 54. XPS spectra are shown for (left) sputter cleaned gold IDE, (middle) C_{60} on sputter cleaned gold IDE, and (right) TiOPc on sputter cleaned gold IDE. (*) indicate emission from the grounded gold IDE. (**) indicate emission from carbon in electrically grounded environments. (***) indicate N 1s emission from electrically grounded environments. (†) indicate emission from electrically charged gold IDEs. (‡) indicate emission from charged carbon environments. Significant charging of the floating electrodes is observed for the sputter cleaned gold, where there is no conductive pathway from the grounded electrodes to the floating electrodes. There is only a slight shift in the charged components corresponding to the difference in interdigit spacing. For C_{60}, in which electron mobility is significantly greater than hole mobility, the charged gold components are shifted much closer to the grounded Au 4f emission. Alternatively, for TiOPc, where hole mobility is highest, the shift of the charged Au 4f emission is less than was observed for C_{60}.

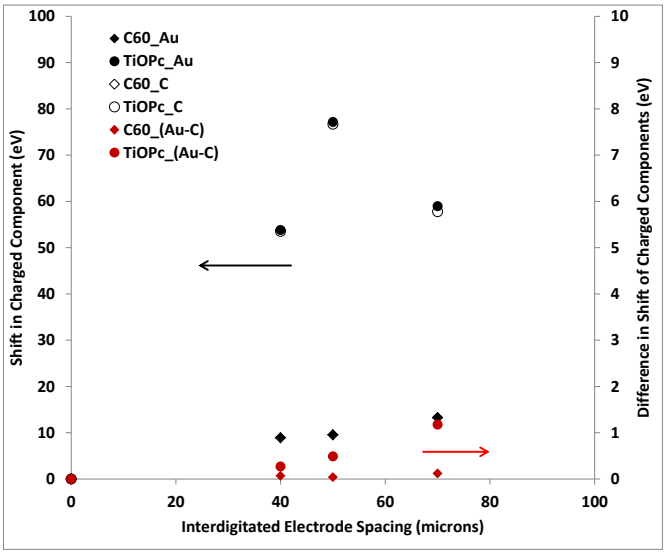

Figure 55. The shift of the charged gold and charged carbon components are not equivalent. The shift of the charged gold components relative to the grounded components, are shown as a function of interdigit spacing. The shift is much greater for the TiOPc films than for the C60 films. (The value at 50microns probably has additional charging due to an inadequate contact.) The difference between the shift of the charged gold components and the charged carbon components are shown on the right-hand y-axis. Gold components shift to a greater extent that the carbon components.

C 1s was also observed at 284 eV, for the electronically grounded component of the overlying organic film, while additional C 1s components were observed at various shifted binding energies. The grounded C 1s component is from the organic semiconductor overlying the grounded gold IDEs, while the charged C 1s component arises from the organic semiconductor overlying the floating gold IDEs. The broad distribution of spectral intensity observed between the grounded C 1s component and the charged C 1s component is likely due to emission from the carbonaceous material in the interdigit gap where there is an electric field across the material.

The shift in the Au 4f and C 1s from their respective grounded components are shown in Figure 56. The sample with TiOPc over an IDE spacing of 50 microns was additionally charged, probably due to a poor electrode contact. The shifts of the gold and carbon peaks were significantly greater in the presence of the TiOPc, relative to the shifts observed for C60 films. This would be expected since C60 is a much better electron conductor than TiOPc and should neutralize the charged gold electrodes more effectively than TiOPc. Additionally, the shift of the carbon and gold peaks was not equal for any of the films or interdigit spacings. Since electrons must transverse the gap between electrodes, with charge injection steps at each electrode, it would be anticipated that the charged gold electrodes would be additionally shifted by the energy barrier associated with charge injection from the organic film into the gold electrode. This appears to be the case since the carbon peaks are shifted less than the charged gold peaks. The difference in the shift was much greater for the TiOPc films indicating a larger barrier for charge injection from TiOPc to gold. Figure 57 shows a cartoon of the pathway for electron flow in the material leading to differential charging of the organic and the ungrounded gold electrodes.

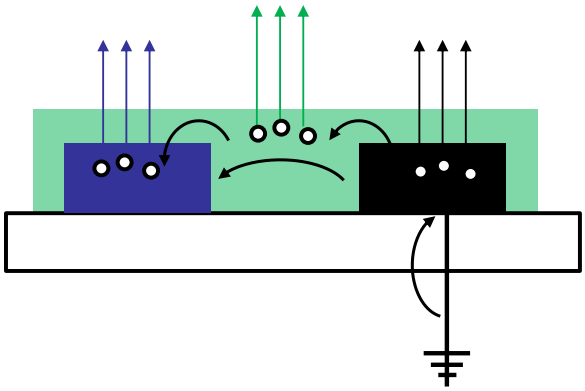

Figure 56. A cartoon of electron flow is shown for a simplified IDE electrode. Arrows relate to electron flow. Electrons are emitted from all illuminated areas of the sample leaving core holes which must be refilled. The only path for electrons back into the system is through the grounding of the sample to the electron spectrometer. Electrons must then inject into the organic film and then transport across the interdigit gap through the organic, and reinjected into the electrically disconnected gold IDE. Since there is an additional charge injection step to neutralize the floating gold IDEs, the charged gold components are always shifted more than the charged carbon components. Background emission form the quartz substrates is either not observed, due to an insufficient escape depth through the overlying organic film, or are so charged as to be broadened and shifted out of the spectrum.

5.3. Pentacene Conversion on IDE

Pentacene is a known hole conductor and has been used to yield OPV devices with good overall photoconversion efficiencies.[100] Pentacene is typically deposited via vacuum deposition; however, soluble pentacene-based molecules have been synthesized.[101, 102] Soluble pentacene precursors can be cast into thin films on a desired substrate using cheap, large area processing methods, such as spin coating, under atmospheric pressures. In some cases, the precursors can be converted to pentacene by thermal treatment. 13,6-N-sulfinylacetamidopentacene is soluble in chloroform and has been used to prepare pentacene thin films from spin coating followed by a thermal treatment to convert the precursor film to a film of pentacene, Figure 58.[27, 103]

In this study a film of the soluble pentacene precursor was deposited over gold IDE substrates. The samples were then placed into the analysis chamber for XPS characterization. The insulating precursor film was analyzed. The film was then thermally treated, in the UHV analysis chamber, to convert the precursor film to a semiconducting film of pentacene. The sample was then reanalyzed via XPS. The key to this experiment, as discussed above, was to make the films sufficiently thin such that Au 4f emission could be observed through the organic overlayer.

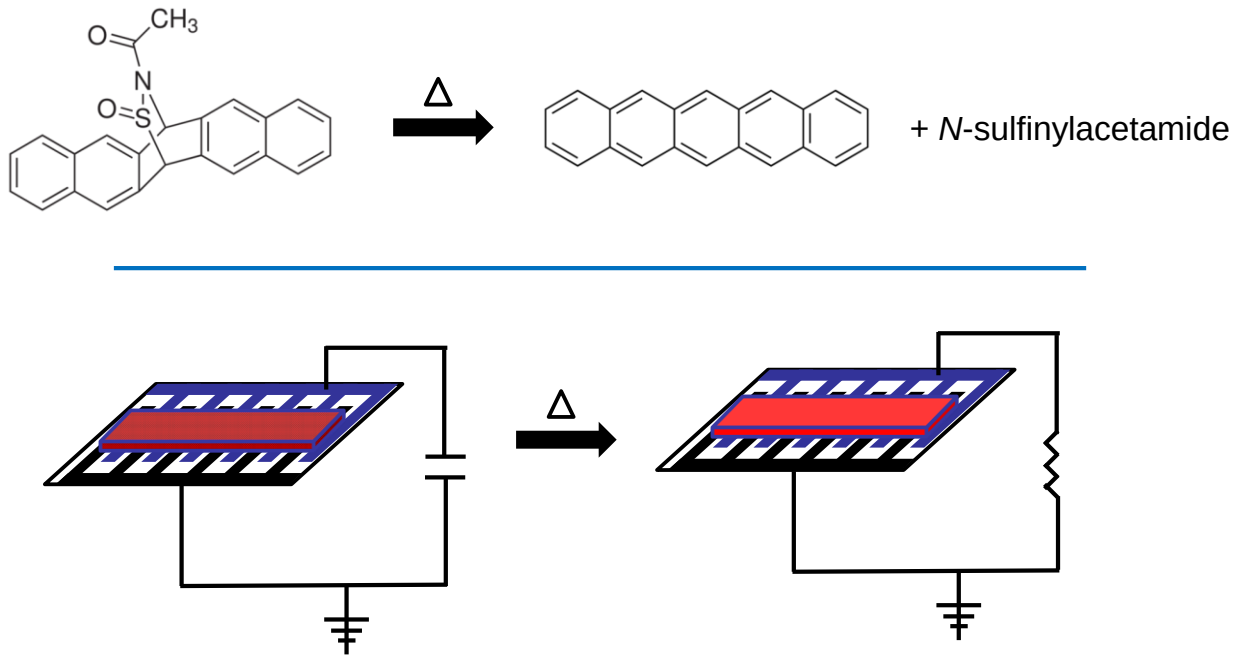

Figure 57. The pentacene precursor was deposited via spin coating from solution. The sample was then placed under vacuum where it was analyzed via XPS. Conversion to the pentacene molecule was performed by heating the sample *in situ*. Analyses of the resulting films were then performed without breaking vacuum. The film of the pentacene precursor should not have any appreciable conductivity, while the pentacene film would be expected to be conducting.

Figure 59 shows the XPS spectra for the film of the pentacene precursor on gold IDEs of varying interdigit spacings. Close-up regions of the Au 4f and C 1s are also shown. A uniform area of the gold substrate was used as a control to evaluate the relative thickness of the precursor film over gold and also to more clearly evaluate changes after the thermal conversion to pentacene. Sulfur and nitrogen were just observable above baseline noise for the precursor film.

There was a shift in the Au 4f and C 1s for the electrically isolated gold electrodes as well as a carbon component associated with charged precursor material. The shift in the charged components was consistent with larger interdigit spacings. Since the precursor film would be expected to be insulating, the shifts were quite large. A broad shoulder on the low binding energy side of the C 1s was observed, most likely due to a range of differentially charged precursor material in the interdigit gap.

Figure 60 shows the corresponding XPS spectra for the thermally treated film. Sulfur and nitrogen were not observed in the converted films. Additionally, the Au 4f signal increased in intensity as the overall carbon intensity decreased. This was partially due to the loss of adventitious species which previously added to the carbon signal. The converted pentacene may have also migrated on the surface and preferentially deposited in the interdigit gap, thereby moving off of the gold surface during thermal treatment. Evaporation of pentacene from the substrate is unlikely, since the conversion temperature was below that of the evaporation temperature.

The shift of the Au 4f and C 1s for charged components of the pentacene film was less than was observed for the pentacene precursor film. This was the anticipated result, as the pentacene film should be much more conducting and should allow for partial neutralization of charging. Figure 61 shows the changes in the shifting of charged species for the precursor and pentacene films.

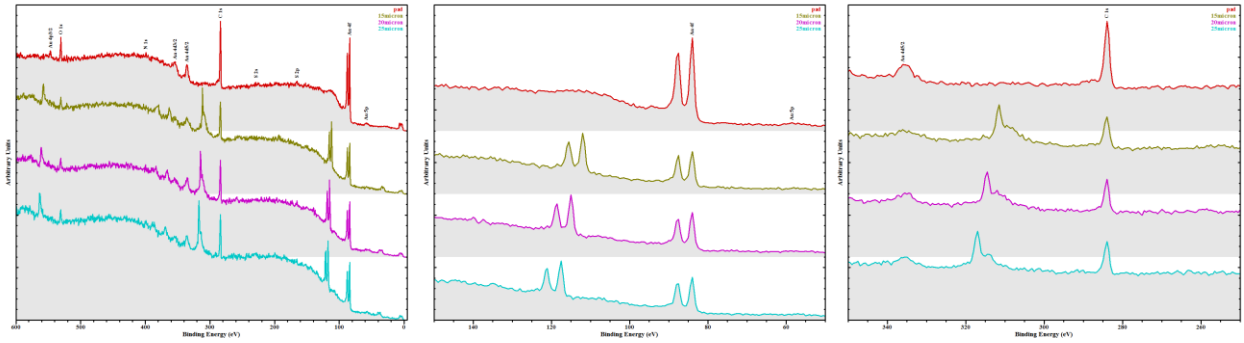

Figure 58. XPS spectra of the pentacene precursor on cleaned gold interdigitated electrodes are shown for (red) a uniform film on gold, (green) 15µm IDE, (pink) 20 µm IDE, and (blue) 25 µm IDE. Spectra shown are (left) survey spectra, (middle) Au 4f and charged Au 4f components, (right) C 1s and charged C 1s components.

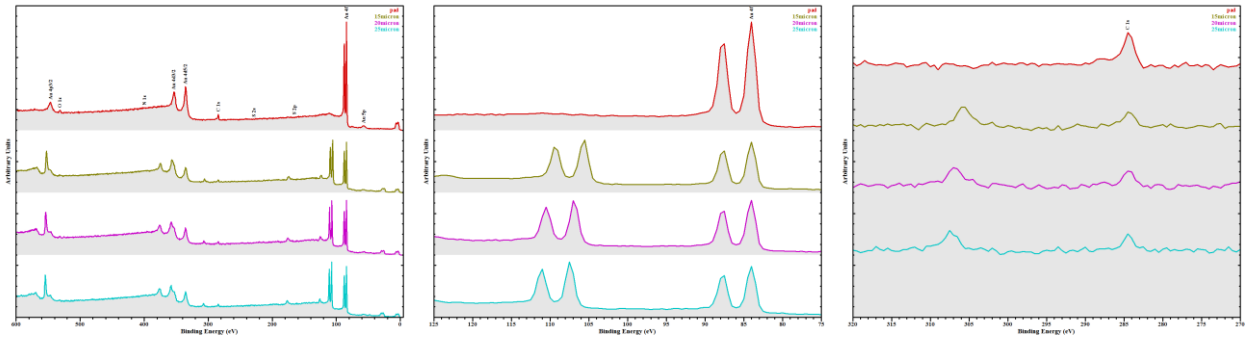

Figure 59. XPS spectra of the converted pentacene on cleaned gold interdigitated electrodes are shown for (red) a uniform film on gold, (green) 15µm IDE, (pink) 20 µm IDE, and (blue) 25 µm IDE. Spectra shown are (left) survey spectra, (middle) Au 4f and charged Au 4f components, (right) C 1s and charged C 1s components.

The shift of the gold and carbon peaks in the precursor film was approximately 10eV greater than the shift observed for the same peaks in the pentacene film. The shift in peaks was nearly linear with the interdigit spacing for both films. Also shown is the difference in shift between the gold and carbon for each respective film at each interdigit spacing. The differences in shifts were greater for the precursor film.

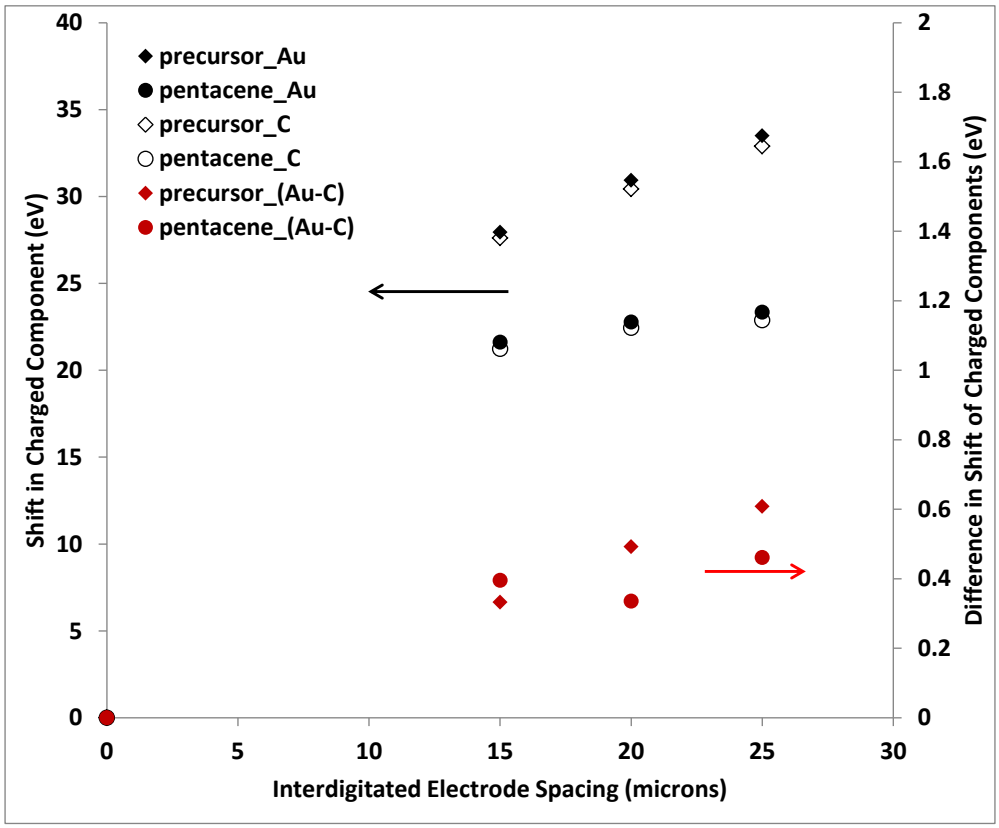

Figure 60. The shift in the charged gold and charged carbon components are shown relative to their respective grounded components, as a function of interdigitated electrode spacing. The shift in the charged gold components is greater than that of the charged carbon components, and the difference is shown on the right-hand y-axis.

As was observed for the TiOPc and C60 films on gold IDEs, the shift in gold and carbon was not the same. This is an interesting result since differential charging is usually observed to shift all components of an XPS spectra equally. However, given the design of this experiment, where there is an interdigit gap, the flow of electrons has to occur through the organic material with an additional charge injection step from the organic into the charged gold IDE, as shown schematically in Figure 57. Consequently, the shifted gold peaks should be shifted more than the

carbon peaks and the shift should be proportional to the charge injection barrier between the organic and the gold.

6. CONCLUSIONS

This study has shown a thorough examination of multiple surface treatments and interfaces with organics. Additionally, multiple emerging photoemission analysis techniques were utilized and a new technique for characterization of materials was discovered.

Thiol SAMs could be patterned via shadow mask UV/ozone patterning, however, the intended nature of the deposited SAMs were altered by the process. NEXAFs imaging, as one of the earliest demonstrations of this technique, proved the existence of patterned thiol SAMs. The corresponding spectra show that the thiol deposited after patterning appears to displace the existing SAM. Additionally, the quality of the SAM film was be influenced by the hysteresis of any previous SAM. Walker and coworker have evaluated SAMs deposited after UV exposure of a previous SAM.[104-106] Here, as supported by NEXAFS, XPS, and UPS, it would appear that the secondarily deposited SAM is either denser or more uniformly aligned over large areas. Work function changes were more substantial for SAM films deposited after an initial SAM was removed. Additionally, the C 1s lineshapes were more distinct for the different SAMs when they were deposited after an initial SAM was removed. C10 appeared to displace patterned C10F8 in a uniform and consistent manner, since no NEXAFS image was observed where C10F8 was previously patterned and backfilled by C10. C10F8 also displaced patterned C10, however, the result gave a pattern of C10F8 SAMs. Angle dependent NEXAFS imaging would be an important avenue for future work to prove orientational differences between thiols deposited before and after patterning. Work function variations were observed for unimolecular SAMs of C10 and C10F8 where the area of coverage was varied by the shadow mask patterning. This may be the first demonstration of such work function changes for patterned SAM films. Further examination of patterned SAMs deposited by a soft-lithographic technique may better preserve the intended unimolecular and bimolecular patterns. Additionally, a greater range in pattern dimensions could be investigated to evaluate a cross-over point between superimposed spectra versus spatially averaged spectra.

HAXPES was shown to be suitable for evaluating the buried interface between ITO and P3HT. The P3HT overlayer acted as a protective barrier to adsorption of adventitious contaminants such that the surface of ITO could be strictly analyzed as a function of surface pretreatment. Robust fitting parameters with clear chemical assignments were identified and could be applied to all samples. This allowed for identification of a surface oxidized layer, distinct from the underlying conductive bulk oxide. A clear discrimination of the surface components from the bulk component was observed. The bulk component exhibits an asymmetry due to the high conductivity in the bulk film, while the surface is fully oxidized and depleted of oxygen vacancies. The thickness of the surface oxidized layer was estimated, and, even after several days of exposure to air, the H_2SO_4-etched sample showed a thinner layer than the other two surface pretreatment conditions.

7. REFERENCES

1. V. Shrotriya, G. Li, Y. Yao, C. W. Chu and Y. Yang, Appl Phys Lett **88** (7) (2006).
2. V. Shrotriya, G. Li, Y. Yao and Y. Yang, P Soc Photo-Opt Ins **6334**, U175-U181 (2006).
3. N. R. Armstrong, D. Alloway, A. Graham, C. Shallcross, M. Brumbach, P. A. Veneman, D. Placencia and W. N. Wang, Proc Spie **7034** (2008).
4. N. R. Armstrong, C. Carter, C. Donley, A. Simmonds, P. Lee, M. Brumbach, B. Kippelen, B. Domercq and S. Y. Yoo, Thin Solid Films **445** (2), 342-352 (2003).
5. N. R. Armstrong, P. A. Veneman, E. Ratcliff, D. Placencia and M. Brumbach, Accounts Chem Res **42** (11), 1748-1757 (2009).
6. N. R. Armstrong, W. N. Wang, D. M. Alloway, D. Placencia, E. Ratcliff and M. Brumbach, Macromol Rapid Comm **30** (9-10), 717-731 (2009).
7. M. Brumbach, D. Placencia and N. R. Armstrong, J Phys Chem C **112** (8), 3142-3151 (2008).
8. O. V. Molodtsova and M. Knupfer, J Appl Phys **99** (5) (2006).
9. G. Nesher, A. Vilan, H. Cohen, D. Cahen, F. Amy, C. Chan, J. H. Hwang and A. Kahn, J Phys Chem B **110** (29), 14363-14371 (2006).
10. R. Schlaf, B. A. Parkinson, P. A. Lee, K. W. Nebesny and N. R. Armstrong, J Phys Chem B **103** (15), 2984-2992 (1999).
11. P. G. Schroeder, M. W. Nelson, B. A. Parkinson and R. Schlaf, Surf Sci **459** (3), 349-364 (2000).
12. D. C. Olson, Y. J. Lee, M. S. White, N. Kopidakis, S. E. Shaheen, D. S. Ginley, J. A. Voigt and J. W. P. Hsu, J Phys Chem C **111** (44), 16640-16645 (2007).
13. D. C. Olson, Y. J. Lee, M. S. White, N. Kopidakis, S. E. Shaheen, D. S. Ginley, J. A. Voigt and J. W. P. Hsu, J Phys Chem C **112** (26), 9544-9547 (2008).
14. M. Brumbach, P. A. Veneman, F. S. Marrikar, T. Schulmeyer, A. Simmonds, W. Xia, P. Lee and N. R. Armstrong, Langmuir **23** (22), 11089-11099 (2007).
15. N. S. Cho, S. K. Lee, J. H. Seo, M. Elbing, J. D. Azoulay, J. Park, S. Cho, A. J. Heeger and G. C. Bazan, J Mater Chem **18** (41), 4909-4911 (2008).
16. Y. Gassenbauer, A. Wachau and A. Klein, Phys Chem Chem Phys **11** (17), 3049-3054 (2009).
17. B. S. Flavel, A. J. Gross, D. J. Garrett, V. Nock and A. J. Downard, Acs Appl Mater Inter **2** (4), 1184-1190 (2010).
18. S. S. C. Yu, E. S. Q. Tan, R. T. Jane and A. J. Downard, Langmuir **23** (22), 11074-11082 (2007).
19. M. E. Roberts, D. R. Wheeler, B. B. McKenzie and B. C. Bunker, J Mater Chem **19** (38), 6977-6979 (2009).
20. P. S. Lysaght, J. Barnett, G. I. Bersuker, J. C. Woicik, D. A. Fischer, B. Foran, H. H. Tseng and R. Jammy, J. Appl. Phys. **101** (2), - (2007).
21. A. K. Rumaiz, J. C. Woicik, E. Cockayne, H. Y. Lin, G. H. Jaffari and S. I. Shah, Appl. Phys. Lett. **95** (26), - (2009).
22. J. C. Woicik, M. Yekutiel, E. J. Nelson, N. Jacobson, P. Pfalzer, M. Klemm, S. Horn and L. Kronik, Phys. Rev. B: Condens. Matter Mater. Phys. **76** (16), - (2007).
23. J. C. Woicik, E. J. Nelson, D. Heskett, J. Warner, L. E. Berman, B. A. Karlin, I. A. Vartanyants, M. Z. Hasan, T. Kendelewicz, Z. X. Shen and P. Pianetta, Phys. Rev. B: Condens. Matter Mater. Phys. **6412** (12), - (2001).

24. S. A. Chambers, T. Droubay, T. C. Kaspar and M. Gutowski, J Vac Sci Technol B **22** (4), 2205-2215 (2004).
25. M. A. Garcia, S. D. Wolter, T. H. Kim, S. Choi, J. Baier, A. Brown, M. Losurdo and G. Bruno, Appl. Phys. Lett. **88** (1) (2006).
26. N. Fairley and A. Carrick, *The Casa Cookbook*. (Acolyte Science, Cheshire, 2005).
27. A. Afzali, C. D. Dimitrakopoulos and T. O. Graham, Adv Mater **15** (24), 2066-2069 (2003).
28. R. Reininger, J. C. Woicik, S. L. Hulbert and D. A. Fischer, Nucl Instrum Meth A **649** (1), 49-51 (2011).
29. T. Sakanoue and H. Sirringhaus, Nat Mater **9** (9), 736-740 (2010).
30. B. H. Hamadani, D. A. Corley, J. W. Ciszek, J. M. Tour and D. Natelson, Nano Lett **6** (6), 1303-1306 (2006).
31. J. H. Seo, A. Gutacker, Y. M. Sun, H. B. Wu, F. Huang, Y. Cao, U. Scherf, A. J. Heeger and G. C. Bazan, J Am Chem Soc **133** (22), 8416-8419 (2011).
32. P. J. Hotchkiss, H. Li, P. B. Paramonov, S. A. Paniagua, S. C. Jones, N. R. Armstrong, J. L. Bredas and S. R. Marder, Adv Mater **21** (44), 4496-+ (2009).
33. S. A. Paniagua, P. J. Hotchkiss, S. C. Jones, S. R. Marder, A. Mudalige, F. S. Marrikar, J. E. Pemberton and N. R. Armstrong, J Phys Chem C **112** (21), 7809-7817 (2008).
34. S. E. Koh, K. D. McDonald, D. H. Holt, C. S. Dulcey, J. A. Chaney and P. E. Pehrsson, Langmuir **22** (14), 6249-6255 (2006).
35. S. Maldonado, T. J. Smith, R. D. Williams, S. Morin, E. Barton and K. J. Stevenson, Langmuir **22** (6), 2884-2891 (2006).
36. L. Y. Park, A. M. Munro and D. S. Ginger, J Am Chem Soc **130** (47), 15916-15926 (2008).
37. Y. Gassenbauer and A. Klein, Solid State Ionics **173** (1-4), 141-145 (2004).
38. M. D. Irwin, B. Buchholz, A. W. Hains, R. P. H. Chang and T. J. Marks, Proc. Natl. Acad. Sci. U. S. A. **105** (8), 2783-2787 (2008).
39. N. Herzer, M. M. Wienk, P. Schmit, A. B. Spoelstra, C. E. Hendriks, S. D. Oosterhout, S. Hoeppener and U. S. Schubert, J Mater Chem **20** (32), 6618-6621 (2010).
40. S. P. Harvey, T. O. Mason, C. Korber, Y. Gassenbauer and A. Klein, Appl Phys Lett **92** (25) (2008).
41. S. P. Tiwari, K. A. Knauer, A. Dindar and B. Kippelen, Org Electron **13** (1), 18-22 (2012).
42. J. B. Kim, C. Fuentes-Hernandez, S. J. Kim, S. Choi and B. Kippelen, Org Electron **11** (6), 1074-1078 (2010).
43. J. S. Kim, F. Cacialli, M. Granstrom, R. H. Friend, N. Johansson, W. R. Salaneck, R. Daik and W. J. Feast, Synthetic Met **101** (1-3), 111-112 (1999).
44. J. S. Kim, P. K. H. Ho, D. S. Thomas, R. H. Friend, F. Cacialli, G. W. Bao and S. F. Y. Li, Chem Phys Lett **315** (5-6), 307-312 (1999).
45. J. S. Kim, B. Lagel, E. Moons, N. Johansson, I. D. Baikie, W. R. Salaneck, R. H. Friend and F. Cacialli, Synthetic Met **111**, 311-314 (2000).
46. C. D. Bain and G. M. Whitesides, Science **240** (4848), 62-63 (1988).
47. N. L. Abbott, J. P. Folkers and G. M. Whitesides, Science **257** (5075), 1380-1382 (1992).
48. Y. N. Xia, X. M. Zhao and G. M. Whitesides, Microelectron Eng **32** (1-4), 255-268 (1996).

49. P. E. Laibinis, M. A. Fox, J. P. Folkers and G. M. Whitesides, Langmuir **7** (12), 3167-3173 (1991).
50. J. Lahiri, E. Ostuni and G. M. Whitesides, Langmuir **15** (6), 2055-2060 (1999).
51. A. Kumar, H. A. Biebuyck and G. M. Whitesides, Langmuir **10** (5), 1498-1511 (1994).
52. H. A. Biebuyck, C. D. Bian and G. M. Whitesides, Langmuir **10** (6), 1825-1831 (1994).
53. C. D. Bain, H. A. Biebuyck and G. M. Whitesides, Langmuir **5** (3), 723-727 (1989).
54. C. D. Bain, E. B. Troughton, Y. T. Tao, J. Evall, G. M. Whitesides and R. G. Nuzzo, J Am Chem Soc **111** (1), 321-335 (1989).
55. C. D. Bain, J. Evall and G. M. Whitesides, J Am Chem Soc **111** (18), 7155-7164 (1989).
56. H. Sezen and S. Suzer, Journal of Vacuum Science & Technology A **28** (4), 639-642 (2010).
57. J. J. Boland, Surf Interface Anal **10** (2-3), 149-152 (1987).
58. O. O. Ekiz, K. Mizrak and A. Dana, Acs Nano **4** (4), 1851-1860 (2010).
59. S. C. DeCaluwe, M. E. Grass, C. J. Zhang, F. El Gabaly, H. Bluhm, Z. Liu, G. S. Jackson, A. H. McDaniel, K. F. McCarty, R. L. Farrow, M. A. Linne, Z. Hussain and B. W. Eichhorn, J Phys Chem C **114** (46), 19853-19861 (2010).
60. C. J. Zhang, M. E. Grass, A. H. McDaniel, S. C. DeCaluwe, F. El Gabaly, Z. Liu, K. F. McCarty, R. L. Farrow, M. A. Linne, Z. Hussain, G. S. Jackson, H. Bluhm and B. W. Eichhorn, Nat Mater **9** (11), 944-949 (2010).
61. S. Suzer, H. Sezen, G. Ertas and A. Dana, J Electron Spectrosc **176** (1-3), 52-57 (2010).
62. H. Sezen and S. Suzer, Surf Sci **604** (21-22), L59-L62 (2010).
63. S. Suzer, E. Abelev and S. L. Bernasek, Appl Surf Sci **256** (5), 1296-1298 (2009).
64. G. Ertas, U. K. Demirok, A. Atalar and S. Suzer, Appl Phys Lett **86** (18) (2005).
65. G. Ertas and S. Suzer, Surf Interface Anal **36** (7), 619-623 (2004).
66. B. Ulgut and S. Suzer, J Phys Chem B **107** (13), 2939-2943 (2003).
67. T. Hauffman, O. Blajiev, J. Snauwaert, C. van Haesendonck, A. Hubin and H. Terryn, Langmuir **24** (23), 13450-13456 (2008).
68. A. K. M. M. Islam and M. Mukherjee, J Phys Chem B **112** (29), 8523-8529 (2008).
69. M. Dubey, I. Gouzman, S. L. Bernasek and J. Schwartz, Langmuir **22** (10), 4649-4653 (2006).
70. I. Gouzman, M. Dubey, M. D. Carolus, J. Schwartz and S. L. Bernasek, Surf Sci **600** (4), 773-781 (2006).
71. H. Peisert, M. Knupfer, T. Schwieger, J. M. Auerhammer, M. S. Golden and J. Fink, J Appl Phys **91** (8), 4872-4878 (2002).
72. N. Dam, M. M. Beerbom, J. C. Braunagel and R. Schlaf, J Appl Phys **97** (2) (2005).
73. J. E. Lyon, A. J. Cascio, M. M. Beerbom, R. Schlaf, Y. Zhu and S. A. Jenekhe, Appl Phys Lett **88** (22) (2006).
74. J. H. Seo, R. Q. Yang, J. Z. Brzezinski, B. Walker, G. C. Bazan and T. Q. Nguyen, Adv Mater **21** (9), 1006-+ (2009).
75. S. P. Harvey, T. O. Mason, Y. Gassenbauer, R. Schafranek and A. Klein, J Phys D Appl Phys **39** (18), 3959-3968 (2006).
76. Y. Gassenbauer, R. Schafranek, A. Klein, S. Zafeiratos, M. Havecker, A. Knop-Gericke and R. Schlogl, Phys Rev B **73** (24) (2006).
77. A. J. Cascio, J. E. Lyon, M. M. Beerbom, R. Schlaf, Y. Zhu and S. A. Jenekhe, Appl Phys Lett **88** (6) (2006).
78. T. Kawai, Y. Maekawa and M. Kusabiraki, Surf Sci **601** (22), 5276-5279 (2007).

79. S. K. So, W. K. Choi, C. H. Cheng, L. M. Leung and C. F. Kwong, Appl Phys a-Mater **68** (4), 447-450 (1999).
80. Z. Z. You and J. Y. Dong, Appl Surf Sci **253** (4), 2102-2107 (2006).
81. Z. Y. Zhong and Y. D. Jiang, Phys Status Solidi A **203** (15), 3882-3892 (2006).
82. L. Kover, J Electron Spectrosc **178**, 241-257 (2010).
83. R. Claessen, M. Sing, M. Paul, G. Berner, A. Wetscherek, A. Muller and W. Drube, New J Phys **11** (2009).
84. J. Rubio-Zuazo and G. Castro, Rev Adv Mater Sci **15** (1), 79-86 (2007).
85. K. Siegbahn, Nucl Instrum Meth A **547** (1), 1-7 (2005).
86. X. H. Zhang, S. P. Tiwari, S. J. Kim and B. Kippelen, Appl Phys Lett **95** (22) (2009).
87. J. S. Kim, R. H. Friend and F. Cacialli, J Appl Phys **86** (5), 2774-2778 (1999).
88. J. C. C. Fan and J. B. Goodenough, J Appl Phys **48** (8), 3524-3531 (1977).
89. C. J. Powell and A. Jablonski, *NIST Electron Inelastic-Mean-Free-Path Database - Version 1.2*. (National Institute of Standards and Technology, Gaithersburg, MD, 2010).
90. Y. Sohn and J. T. Stuckless, Appl Phys Lett **90** (17) (2007).
91. T. M. Brown, J. S. Kim, R. H. Friend, F. Cacialli, R. Daik and W. J. Feast, Synthetic Met **111**, 285-287 (2000).
92. H. Peisert, M. Knupfer, F. Zhang, A. Petr, L. Dunsch and J. Fink, Surf Sci **566**, 554-559 (2004).
93. E. L. Ratcliff, P. A. Lee and N. R. Armstrong, J Mater Chem **20** (13), 2672-2679 (2010).
94. Q. F. Dong, Y. H. Zhou, J. N. Pei, Z. Y. Liu, Y. W. Li, S. Y. Yao, J. B. Zhang and W. J. Tian, Org Electron **11** (7), 1327-1331 (2010).
95. Y. S. Kim, S. B. Oh, J. H. Park, M. S. Cho and Y. Lee, Sol Energ Mat Sol C **94** (3), 471-477 (2010).
96. S. Schwertheim, O. Grewe, I. Hamm, T. Mueller, R. Pichner and W. R. Fahrner, Ieee Phot Spec Conf (2010).
97. J. W. Huh, Y. M. Kim, Y. W. Park, J. H. Choi, J. W. Lee, J. W. Lee, J. W. Yang, S. H. Ju, K. K. Paek and B. K. Ju, J Appl Phys **103** (4) (2008).
98. L. Lindell, A. Burquel, F. L. E. Jakobsson, V. Lemaur, M. Berggren, R. Lazzaroni, J. Cornil, W. R. Salaneck and X. Crispin, Chem Mater **18** (18), 4246-4252 (2006).
99. Y. Qiu, L. Duan and L. D. Wang, Chinese Sci Bull **47** (23), 1979-1982 (2002).
100. S. Yoo, B. Domercq and B. Kippelen, Appl Phys Lett **85** (22), 5427-5429 (2004).
101. J. H. Chen, C. K. Tee, M. Shtein, D. C. Martin and J. Anthony, Org Electron **10** (4), 696-703 (2009).
102. S. K. Park, J. E. Anthony and T. N. Jackson, Ieee Electr Device L **28** (10), 877-879 (2007).
103. A. Afzali, C. D. Dimitrakopoulos and T. L. Breen, J Am Chem Soc **124** (30), 8812-8813 (2002).
104. C. Z. Zhou, A. Trionfi, J. C. Jones, J. W. P. Hsu and A. V. Walker, Langmuir **26** (6), 4523-4528 (2010).
105. C. Z. Zhou and A. V. Walker, Langmuir **23** (17), 8876-8881 (2007).
106. C. Z. Zhou and A. V. Walker, Langmuir **22** (26), 11420-11425 (2006).

DISTRIBUTION

1	MS0359	D. Chavez, LDRD Office	01911
1	MS0614	Chris Orendorff	02546
1	MS0734	Timothy Lambert	06124
1	MS0885	Terence Aselage	01810
1	MS0885	Steve Lott	01820
1	MS0886	Jim Aubert	01822
1	MS0886	Joe Michael	01822
1	MS0886	James Ohlhausen	01822
1	MS0888	Cody Washburn	01821
1	MS0888	Shawn Dirk	01821
1	MS0888	Kevin Zavadil	01825
1	MS0889	Jill Glass	01825
1	MS0892	David Wheeler	01714
1	MS0892	Joe Simonson	01716
1	MS0892	Ronen Polsky	01714
1	MS0892	Susan Brozik	01714
1	MS0958	Mike Kelly	01833
1	MS0959	Robert Grubbs	01832
1	MS0959	Dave Adams	01832
1	MS1315	Sean Hearne	01132
1	MS1304	Dale Huber	01132
1	MS1411	Erik Spoerke	01816
1	MS1411	Geoff Brennecka	01816
1	MS1411	Paul Clem	01816
1	MS1415	Calvin Chan	01114
1	MS1415	Carlos Gutierrez	01114
1	MS1425	Xiaoyin Xiao	01714
1	MS0899	RIM–Reports Management	9532 (electronic copy)

Sandia National Laboratories